Hydrodynamics of Wind-Assisted Ships

A Numerical and Experimental Study on a Systematic Series of Bare Hull Models at Drift Angles

Gijsbert D. Struijk

Master of Science Thesis

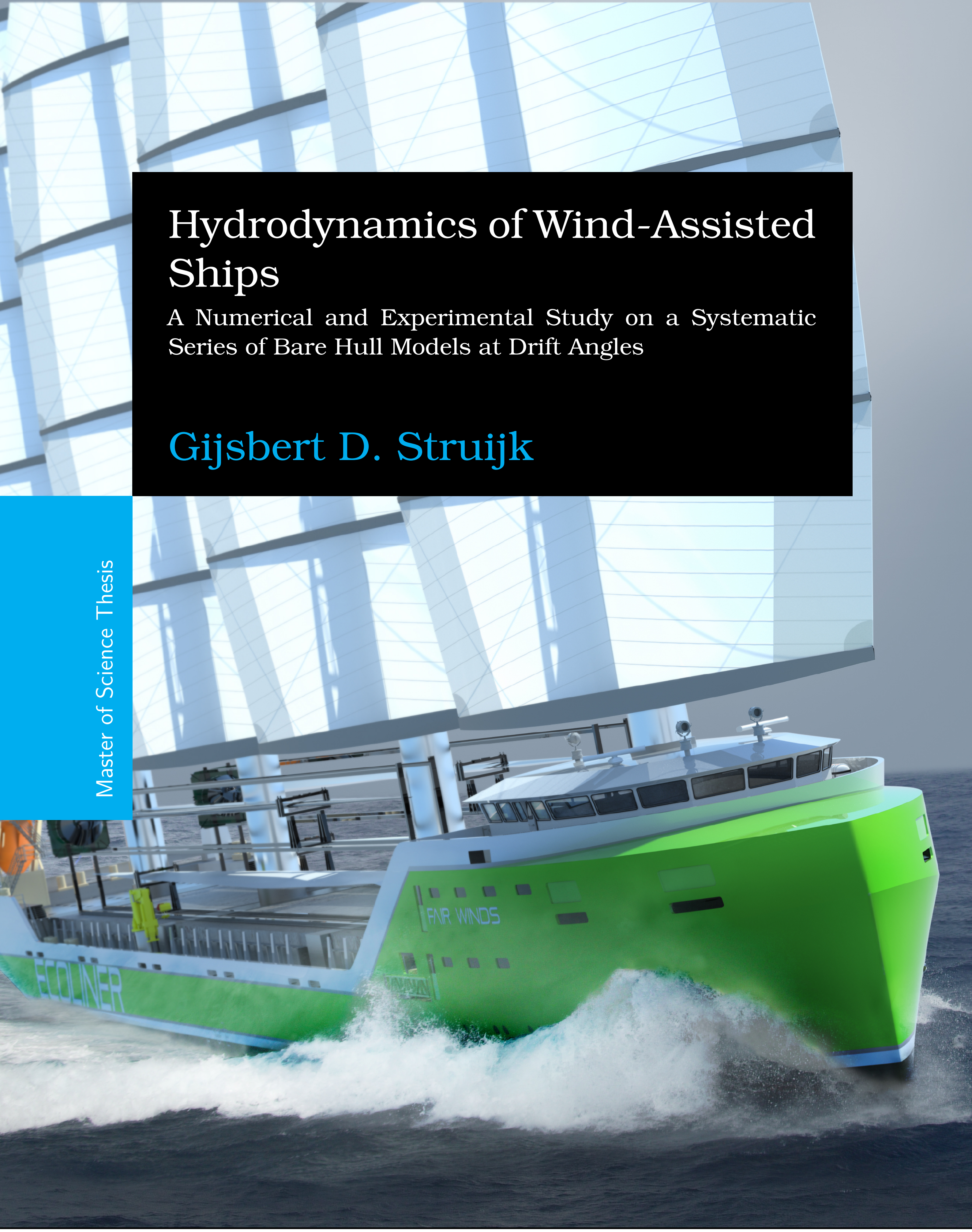

Delft
University of
Technology

Hydrodynamics of Wind-Assisted Ships

A Numerical and Experimental Study on a Systematic Series of Bare Hull Models at Drift Angles

MASTER OF SCIENCE THESIS

For the degree of Master of Science in Ship Hydromechanics and Structures at Delft University of Technology

Gijsbert D. Struijk

June 11, 2015

Faculty of Mechanical, Maritime and Materials Engineering (3mE) · Delft University of Technology

Cover art: the *Ecoliner* under full canvas, courtesy of Dykstra Naval Architects

DELFT UNIVERSITY OF TECHNOLOGY
DEPARTMENT OF
MARITIME AND TRANSPORT TECHNOLOGY (M&TT)

The undersigned hereby certify that they have read and recommend to the Faculty of Mechanical, Maritime and Materials Engineering (3mE) for acceptance a thesis entitled

HYDRODYNAMICS OF WIND-ASSISTED SHIPS

by

GIJSBERT D. STRUIJK

in partial fulfillment of the requirements for the degree of

MASTER OF SCIENCE SHIP HYDROMECHANICS AND STRUCTURES

Dated: June 11, 2015

Supervisor(s):

Prof. dr. ir. R.H.M. Huijsmans

Dr. ir. J.A. Keuning

Reader(s):

Prof. ir. J.J. Hopman

Dr. ir. I. Akkerman

Ir. N.J. van der Kolk

Abstract

With fuel oil the main driver for operational expenses, increasingly stringent regulations on emissions of ships and a growing environmental awareness throughout the industry, the concept of Wind-Assisted Ship Propulsion (WASP) presents itself as a means to reduce fuel consumption. Though a promising concept, the performance prediction of a wind-assisted vessel is a complex task involving many physical interactions.

As part of a larger research plan on WASP at the Delft University of Technology, this thesis focusses on the hydrodynamic forces on bare hull models at drift angles resulting from the wind-assisted operating conditions. The aim of this study is firstly to show the adequacy of RANS CFD as a numerical tool to estimate the hydrodynamic forces (resistance, side force and yaw moment) for vessels sailing at a drift angle. Secondly, the aim is to deliver a database of hydrodynamic forces for a series of hull forms. This database will ultimately aid in modelling a wind-assisted vessel in a Performance Prediction Programme (PPP).

A systematic series of bare hull forms based on one parent hull is constructed by varying draught T, prismatic coefficient C_p and midship section area coefficient C_m. The numerical tool is used to obtain the hydrodynamic forces of all models while three selected models are tested in a towing tank for validation. On the simulation results, regression analysis is performed to arrive at formulations expressing the dependency of these forces on the bare hull form parameters.

The validation study shows that the numerical tool captures most hydrodynamic forces sufficiently accurate for use in a PPP tool. With side force most poorly resolved, there is room for improvement however. Using a different turbulence model could provide improvement in this area, albeit at the cost of increased computational time.

The formulations obtained by regression show satisfactory robustness for vessels having hydrostatic parameters both within and outside the range of the Delft Systematic Wind-Assisted Series (DSWAS). Unfortunately, the lack of precision of the side force formulation can lead to erroneous results when applied in a PPP.

Table of Contents

List of Figures

List of Tables

Glossary

List of Acronyms

ANSI	American National Standards Institute
ASME	American Society of Mechanical Engineers
BICS	Blended Interface Capturing Scheme
CAD	Computer Aided Design
CFD	Computational Fluid Dynamics
CLR	Centre of Lateral Resistance
DES	Detached Eddy Simulation
DNS	Direct Numerical Simulation
DSWAS	Delft Systematic Wind-Assisted Series
DSYHS	Delft Systematic Yacht Hull Series
DWL	Design Waterline
EASM	Explicit Algebraic Stress Model
EEDI	Energy Efficiency Design Index
FVM	Finite Volume Method
GCI	Grid Convergence Index
ITTC	International Towing Tank Conference
NURBS	Non-Uniform Rational B-Spline
PIV	Particle Image Velocimetry
PMB	Parallel Middle Body

PPP	Performance Prediction Programme
QUICK	Quadratic Upstream Interpolation for Convective Kinematics
RANS	Reynolds-averaged Navier-Stokes
RE	Richardson Extrapolation
RSM	Reynolds Stress Modelling
RSS	Root of Sum of Squares
SEE	Standard Error Estimate
SHS	Ship Hydromechanics and Structures
TU Delft	Delft University of Technology
UDS	Upwind Differencing Scheme
VOF	Volume of Fluid
V&V	Verification and Validation
WASP	Wind-Assisted Ship Propulsion

List of Symbols

α	Model scale	
Æ	Aspect ratio	
β	Drift angle	deg
Δ	Displacement mass	kg
ϵ	Error	
∇	Displacement volume	m^3
ν	Kinematic viscosity	m^2/s
ϕ	Heel angle	deg
ρ	Density	kg/m^3
τ	Trim, $\tau = T_a - T_f$	m
θ	Trim angle	deg
A_{hl}	Lateral area	m^2
A_{wp}	Waterplane surface	m^2
B	Breadth	m
C_b	Block coefficient	
C_L	Lift coefficient	

C_m	Midship area coefficient	
C_o	Courant number	
C_p	Prismatic coefficient	
C_{Di}	Induced drag coefficient	
$C_{f,ITTC}$	ITTC-57 correlation coefficient	
C_{hl}	Lateral area coefficient	
C_n	Yaw moment coefficient	
C_{wp}	Waterplane area coefficient	
C_{xR}	Residuary resistance coefficient	
C_y	Side force coefficient	
D	Depth	m
D	Experimental result	N or Nm
E	Comparison error	$\%D$
E_r	Exit rocker angle	deg
F_n	Froude number, $F_n = \frac{V}{\sqrt{gL}}$	
F_s	Safety factor	
f_s	Sampling frequency	Hz
F_x	Resistance in flow aligned coordinates	N
F_y	Side force in ship-fixed coordinates	N
F_a	Side force at aft balance arm	N
F_f	Side force at forward balance arm	N
F_{xR}	Residuary resistance in flow aligned coordinates	N
G	Centre of gravity	
h	Typical cell size	m
I_e	Incidence angle of waterline entrance	deg
L	Reference length	m
L_{hl}	Geometric centre of lateral area	m^2
L_{oa}	Length over all	m
L_{PMB}	Length of Parallel Middle Body (PMB)	m
L_{pp}	Length between perpendiculars	m
L_{wl}	Waterline length	m
LCB	Longitudinal Centre of Buoyancy	$\%L$ w.r.t. ⊗
M_z	Yaw moment in ship-fixed coordinates, taken about ⊗	Nm
p	Order of convergence	
Q	Second invariant	
q	Dynamic pressure, $q = {}^1\!/\!{}_2\rho V_m^2$	N/m^2
r	Pearson's correlation coefficient	
R^2	Coefficient of determination	
R_b	Bilge radius	m
Re	Reynolds number, $Re = \frac{VL}{\nu}$	

S	Numerical simulation result	N or Nm
S_w	Wetted surface	m^2
T	Draught	m
U_D	Experimental uncertainty	$\%D$
U_G	Discretisation uncertainty	$\%S$
U_S	Simulation numerical uncertainty	$\%S$
U_{val}	Validation uncertainty	$\%D$
V_m	Model velocity	m/s
V_s	Ship velocity	kn
VCB	Vertical Centre of Buoyancy	$\%T$, w.r.t. CWL
y^+	Dimensionless wall distance	
℄	Centreline	
⊗	Midship, defined at $^L/_2$	

Preface

Although promising, the concept of Wind-Assisted Ship Propulsion is one of complex nature. This makes for a challenging prediction of its effect on the operational performance of a vessel. With the goal to tackle the most important physical phenomena involved, a research involving two PhD candidates is initiated at the Delft University of Technology with the goal of delivering a more accurate Performance Prediction Programme (PPP).

As part of that project, this MSc thesis focusses on a selection of hydrodynamic phenomena. Executed in parallel with the initial phases of the project, the nature of the study is exploratory. Focussing on bare hull hydrodynamic forces, RANS CFD is used to obtain hydrodynamic forces for a series of hull forms dubbed Delft Systematic Wind-Assisted Series (DSWAS). For validation purposes, experiments are conducted in the towing tank of the university's Ship Hydromechanics department.

Doing my graduation research at this department on a subject close to my personal interest has been a true privilege. I greatly enjoyed working at this department and I would like to express my gratitude towards the people working there.

First and foremost to Dr. ir. Lex Keuning for his supervision. I greatly value his engagement in the project and I enjoyed the helpful discussions throughout the period of this thesis. I would also like to thank Prof. dr. ir. René Huijsmans for his valuable criticism, pushing the level of this thesis. Furthermore, I thank the department staff for their assistance in both the numerical and experimental work as well as helping me out with various questions I fired at them.

On a more personal note, I thank my parents for their everlasting support and the healthy distraction they offered with more practical boating issues during the weekends.

Delft, The Netherlands
June 11, 2015

Gijsbert D. Struijk

“No one believes the CFD results except the one who performed the calculation, and everyone believes the experimental results except the one who performed the experiment.”

— *P.J. Roache, 1998*

Chapter 1

Introduction

1-1 Framework

With increasing oil prices and environmental awareness throughout the shipping industry, interest in fuel and emission reduction has grown over the recent years. Modern shipping companies are not only driven by fuel costs, but also by regulatory bodies. A main driver in this is the Energy Efficiency Design Index (EEDI). With its roots in a MARPOL convention addressing air pollution, this mandatory index for new ships puts stringent requirements on the emissions of a vessel, pressing the shipping companies and consequently ship designers to develop cleaner alternatives for ship propulsion. In this light, the possibility to harness wind energy for a vessel's propulsion presents itself as an alternative to fossil fuel driven engines. Or in a more hybrid form: an auxiliary propulsion to reduce fuel consumption. This concept of motor-sailing, dubbed Wind-Assisted Ship Propulsion (WASP), combines the reliability of schedule that a combustion engine offers with the fuel-free propulsion by wind. Such a hybrid form could well bring feasibility to this concept in the modern ages of shipping.

Despite the very recent interest in WASP, the idea of using wind as propulsion is not at all new. The shipping industry has its roots in vessels harnessing the power of the wind to sail their cargo around the globe, with the square-rigged windjammers of the early 1900's being the final iteration. The era of sailing cargo vessels ended with the uprising of steam- and combustion engines. In the beginning of the 20$^{\text{th}}$ century the numbers of wind-driven cargo ships diminished. By that time the engine-driven ships offered faster transits and more reliable schedules. Apart from some attempts in the 1920's to introduce the Flettner rotor as ship propulsion (Prandtl, 1925), little attention was given to the concept of WASP in the following decades.

During the energy and oil crises of the 1970's, interest in using wind as a source of propulsion was rejuvenated. In literature, much research into the feasibility of (motor-)sailing a cargo vessel can be found from the 1980's, most of which focusses on practical and economic feasibility or aerodynamic considerations of rig types.

1-2 State of the art

Nowadays, with rising fuel prices and a greater environmental awareness, interest has picked up again. In appendix A a literature review focussing on WASP studies is presented. Studies from both the 1980's and recent years show the fuel saving potential of wind-assistance. However, the scatter is large still. Partly because of different approaches to the problem, and partly because of the lack of accurate prediction methods. Often, the estimation of hydrodynamic forces is simplified, not incorporating an accurate prediction for side force and induced resistance. Furthermore, it becomes apparent that one of the greatest hydrodynamic challenges with sailing a cargo vessel at a drift angle is controlling the yaw moment. However, this is an often neglected problem when estimating the performance of a WASP vessel.

A previous MSc thesis at the TU Delft on WASP (Mobron, 2014) focusses on improving this imbalance on the concept vessel *Ecoliner* (Nikkels, 2013). From this study it was concluded that adding a skeg at the aft ship is an effective way to reduce the yaw moment (by 27% w.r.t. bare hull). Furthermore, the side force is significantly increased (more than doubled w.r.t. bare hull) leading to a large shift aft of the Centre of Lateral Resistance (CLR).

1-3 Aim of the current study

From past research as well as more recent work in the field of WASP it becomes clear that there is need for a better performance prediction of a vessel in wind-assisted conditions. At the Ship Hydromechanics and Structures (SHS) section of the TU Delft, a research project involving two PhD candidates is recently initiated on the topic of WASP (Bordogna et al., 2014). The research programme is split into two components: an aerodynamic and a hydrodynamic part. The execution is divided as such over the two PhD candidates.

The overall aim of the project is to deliver a refined Performance Prediction Programme (PPP) for WASP concepts. This PPP will couple the aero- and hydrodynamic forces to obtain a solution for velocity under sail and ultimately a thrust reduction. To be able make the PPP more accurate, refinements are needed on many fronts.

Focussing only on the hydrodynamics, possible issues include, but are not limited to: side force, yaw moment (and consequently CLR), (induced) resistance, propeller loading and efficiency in oblique flow, engine efficiency at partial load and dynamic effects such as added resistance in waves and aero-hydro coupling in the field of ship motions.

As observed from recent studies, the ability for a typical merchant vessel (without a keel like a sailing yacht) to produce side force whilst keeping control of the yaw moment is as much a primary issue as it is a neglected or simplified one. It is therefore flagged as starting topic for the hydrodynamic research. Furthermore, in order to have a first database to test a preliminary PPP, hydrodynamic forces of a small systematic series is desired.

Splitting the hydrodynamic problems up in parts, the decision is made to study the effect of bare hull form variations on the hydrodynamic forces in this thesis, with the intention of covering the effect of appendages at a later stage of the project. The recent availability of commercial Computational Fluid Dynamics (CFD) software at the SHS section offers the opportunity to conduct the research with this tool.

1-3-1 Research questions

The considerations above and the tools at hand give rise to two main questions for the present study:

1. Can the used numerical method predict the bare hull hydrodynamic forces sufficiently accurate for application in a Performance Prediction Programme?
2. Using the numerical results, can a set of formulations be derived that describe the bare hull hydrodynamic forces as function of hull form parameters sufficiently accurate for application in a Performance Prediction Programme?

In which:

- The used numerical method is a RANS CFD code developed by NUMECA (refer to section 3-3 for details).
- The hydrodynamic forces encompass the resistance F_x, side force F_y and yaw moment M_z of the bare hull, i.e. no appendages of any sort are included.

1-3-2 Approach

To be able to answer the research questions, the research approach is outlined as follows:

1. In order to provide a PPP tool with a hydrodynamic database of forces dependent on bare hull form parameters, a small systematic series is constructed on the basis of a parent hull. From observations in literature a choice is made on which hull form parameters to vary.
2. The hydrodynamic forces are evaluated using CFD, eliminating the need to build scale models for *every* geometry in the series for towing tank experiments.
3. Using numerical tools like CFD requires validation. A *selection* of geometries is therefore tested in the towing tank at the same conditions to provide experimental validation data.
4. Validation requires uncertainty estimates for both methods. Repeat runs are performed to obtain an estimate for the experimental uncertainty. Numerical uncertainty is accessed by performing grid studies. A Verification and Validation (V&V) analysis is then conducted to answer research question one.
5. The results from the CFD simulations are used to build regression formulations expressing the hydrodynamic forces as function of form parameters. The performance of these formulations will then answer question two.

1-4 Outline

With the current chapter offering the framework, aim and approach, chapter 2 depicts the construction of the systematic series. Considerations about which parameters are chosen to vary are given and the resulting series is presented. Chapter 3 outlines both the experimental and numerical methods and offers the test conditions while chapter 4 elaborates on the uncertainty analysis for both these methods. With the results and corresponding uncertainties from both methods, the validation is performed in chapter 5 for the selected geometries. Thereafter, the CFD results are used to construct regression formulations in chapter 6. Finally the conclusions are presented in chapter 7 along with recommendations.

Chapter 2

Systematic Series

To investigate the effects of bare hull form parameters on the hydrodynamic forces, a systematic series is constructed from a parent hull. In this chapter, the development of the series dubbed Delft Systematic Wind-Assisted Series (DSWAS) is discussed.

2-1 Parent hull

For constructing a systematic series of Wind-Assisted Ship Propulsion (WASP) models, a parent hull is required. This should be a (concept) vessel for which it is feasible to apply WASP. The availability of experimental or numerical data on the hydrodynamic characteristics of the vessel would be an extra benefit.

Following these requirements, the *Ecoliner* concept is selected as parent hull. See Figure 2-1 for a digital render. Conceived by Dykstra Naval Architects (Nikkels, 2013), this vessel is purposely designed to be wind-assisted. Notable hull form features include a straight bow profile without bulb and a pram shape aft-body without propeller gondola. The concept has already undergone towing tank tests at the TU Delft, offering a good basis to work from. The model is built at a scale of $\alpha = 50$, resulting in a model length of $L = 2.76\,\text{m}$. Table 2-1 offers some full scale particulars for reference.

Table 2-1: Full scale main particulars of the *Ecoliner*

$L_{oa} = L_{wl}$	138	m
B	18.2	m
T	6.5	m
D	10.2	m
Δ	11850	t
DWT	8210	t
V_s design	12	kn
Cargo hold	13000	m^3
TEU capacity	476	-

Figure 2-1: Render of the *Ecoliner*, design by Dykstra Naval Architects (Nikkels, 2013)

2-2 Form variations

To choose which parameters to vary, different considerations are taken into account:

- The parameter should be expected to have a significant influence on the hydrodynamic forces under consideration.
- The number of parameters should be limited, in light of available time and computing power.
- The resulting hullforms should be able to cover a range of applications (e.g. tankers, container vessels, etc.).

To predict which parameters are of primary influence, results from past research on vessels under drift is consulted. A summary of the observations from this literature survey is depicted in Table A-1 in appendix A. From this, the following parameters are chosen for variation within the series:

Draught $\mathbf{T}$ There exists consensus about the influence of draught T on the side force production, which can be related to the effect of aspect ratio and span in airfoil theory.

Prismatic coefficient $\mathbf{C_p}$ On the effect of C_p different findings exist, possibly by different techniques to construct the variations. For example, one could raise C_p by increasing the bilge radius, which could result in a weaker bilge vortex, reducing side force production. However, one could also raise C_p by lengthening the Parallel Middle Body (PMB), lengthening the bilges and thereby increasing the bilge vortex strength. Alternatively, vessels with a low C_p possibly feature a sharp bow that might induce strong local pressure differences or a bow vortex. Furthermore, varying C_p allows for application on a range of vessel types.

Midship coefficient $\mathbf{C_m}$ A sharp-bilged vessel is observed to generate more side force than one with larger bilge radius. Both the windtunnel study on hull blocks by Bradbury (1985) as the study on the submerged wing section by Beukelman (1998) confirm this and it is mentioned in the paper by Schenzle (1980). This has thus been varied and expressed as midship coefficient C_m.

2-2-1 Scaling assumptions

While scaling T the displaced volume ∇ is kept constant. Consequently, the breadth B changes. Previous studies have shown that the change in B has a small effect on the hydrodynamic forces at low Froude numbers (below $F_n = 0.30$) (Gerritsma et al., 1974). When scaling C_p or C_m, the main dimensions L, B and T are kept constant while ∇ changes.

2-2-2 Transformation methods

For generating the form variations of the parent hull, three different methods have been used. For scaling the draught T, affine stretching of the geometry is used (Letcher, 2009). This allows the geometry to be uniformly stretched along different axes. Because the constraint for the draught variations was a constant displacement, the breadth (along y-axis) is lowered when the draught (along the z-axis) is increased and vice versa.

For variations in C_p the transformation method of Lackenby (1950) is used. This method shifts the control points of the NURBS surface longitudinally without changing the sectional shape. An advantage of this method is that one can quite easily make changes in C_p, C_b or LCB while maintaining the characteristics and fairness of the original hull to a large degree.

The variations of C_m have been established by altering the bilge radius. The control points in the PMB have been moved from and towards the bilge point (intersection of bottom and side line) by a certain factor to obtain a bilge radius $3/2$ and $1/2$ as large as the parent hull. This resulted in C_m values of -7.2 % and $+4.5$ % respectively.

The range of variations in T and C_p has been chosen as $\pm 10\%$. This is considered a range yielding realistic hull forms while expected to be large enough to generate sufficiently large differences in hydrodynamic forces. Table 2-2 gives an overview of the range of parameters.

2-2-3 Manual modifications

During the transformations by the methods as depicted in section 2-2-2 two issues in the geometry fairness arose:

- When altering the bilge radius in the PMB the transition of the modified radius to the aft sections was not smooth, i.e. the fairness of the hull was compromised. This transition has been faired by hand.

Table 2-2: Variations of the selected parameters

		$-$	0	$+$
T	%	-10%		$+10\%$
	m	0.117	0.130	0.143
C_p	%	-10%		$+10\%$
	$-$	0.688	0.764	0.840
C_m	%	-7.2%		$+4.5\%$
	$-$	0.874	0.942	0.984

- The Lackenby transformations for the C_p variations also change the bow contour (in side view) due to the shifting of stations. It has been observed (Mobron, 2014) that the bow contour has a primary effect on the side force and yaw moment generation of the hull. In the present study, only the dependency on variations in T, C_p and C_m is of interest. Therefore, it is important to keep other parameters as constant as possible to isolate these effects. For this purpose, after the Lackenby transformations the control points of the bow contour have been placed back at their original x- and z-coordinates.

It must be noted that although these manual adjustments introduce some form of subjectiveness and non-reproducibility, they do reflect design practice. Furthermore, the maximum deviation from the original transformation in terms of displacement, C_p, C_b and LCB throughout the series is 0.33%.

2-2-4 Results

All combinations of the varied parameters yield a series of $3^3 = 27$ models. The resulting hydrostatic parameters are listed in Table 2-3 at model scale. For the linesplans one is referred to Appendix B. The space of varied parameters is visualised with scatter plots in Figure 2-2.

Table 2-3: Hydrostatic parameters of DSWAS models, values at model scale

Model #	Description	∇ m^3	L m	B m	T m	C_p $-$	C_b $-$	C_m $-$	LCB $\%L\between$	S_w m^2
1	Parent	0.0928	2.76	0.360	0.130	0.764	0.719	0.942	0.13	1.317
2	T^+	0.0929	2.76	0.327	0.143	0.764	0.720	0.942	0.19	1.304
3	T^-	0.0928	2.76	0.400	0.117	0.763	0.719	0.942	0.14	1.349
4	C_p^+	0.1021	2.76	0.360	0.130	0.840	0.791	0.942	-0.32	1.389
5	C_p^-	0.0837	2.76	0.360	0.130	0.689	0.649	0.942	1.31	1.258
6	C_m^+	0.0975	2.76	0.360	0.130	0.767	0.755	0.984	0.17	1.383
7	C_m^-	0.0865	2.76	0.360	0.130	0.768	0.671	0.874	0.09	1.255
8	$T^+C_p^+$	0.1022	2.76	0.327	0.143	0.840	0.791	0.942	-0.28	1.375
9	$T^+C_p^-$	0.0838	2.76	0.327	0.143	0.689	0.649	0.942	1.37	1.243
10	$T^-C_p^+$	0.1020	2.76	0.400	0.117	0.839	0.790	0.942	-0.84	1.423
11	$T^-C_p^-$	0.0836	2.76	0.400	0.117	0.688	0.648	0.942	1.26	1.291
12	$T^+C_m^+$	0.0976	2.76	0.327	0.143	0.768	0.756	0.984	0.20	1.369
13	$T^+C_m^-$	0.0866	2.76	0.327	0.143	0.769	0.672	0.874	0.12	1.241
14	$T^-C_m^+$	0.0974	2.76	0.400	0.117	0.767	0.755	0.984	0.15	1.415
15	$T^-C_m^-$	0.0865	2.76	0.399	0.117	0.768	0.671	0.874	0.06	1.287
16	$C_p^+C_m^+$	0.1067	2.76	0.360	0.130	0.840	0.826	0.984	-0.30	1.459
17	$C_p^+C_m^-$	0.0947	2.76	0.360	0.130	0.840	0.734	0.874	-0.38	1.316
18	$C_p^-C_m^+$	0.0873	2.76	0.360	0.130	0.687	0.676	0.984	1.39	1.312
19	$C_p^-C_m^-$	0.0776	2.76	0.360	0.130	0.689	0.602	0.874	0.81	1.190
20	$T^+C_p^+C_m^+$	0.1067	2.76	0.327	0.143	0.840	0.827	0.984	-0.29	1.444
21	$T^+C_p^+C_m^-$	0.0947	2.76	0.327	0.143	0.840	0.734	0.874	-0.36	1.301
22	$T^+C_p^-C_m^+$	0.0874	2.76	0.327	0.143	0.688	0.677	0.984	1.44	1.297
23	$T^+C_p^-C_m^-$	0.0777	2.76	0.327	0.143	0.689	0.602	0.874	0.85	1.178
24	$T^-C_p^+C_m^+$	0.1066	2.76	0.400	0.117	0.839	0.826	0.984	-0.32	1.492
25	$T^-C_p^+C_m^-$	0.0946	2.76	0.399	0.117	0.840	0.734	0.874	-0.40	1.350
26	$T^-C_p^-C_m^+$	0.0872	2.76	0.400	0.117	0.686	0.675	0.984	1.33	1.346
27	$T^-C_p^-C_m^-$	0.0775	2.76	0.399	0.117	0.688	0.601	0.874	0.77	1.221

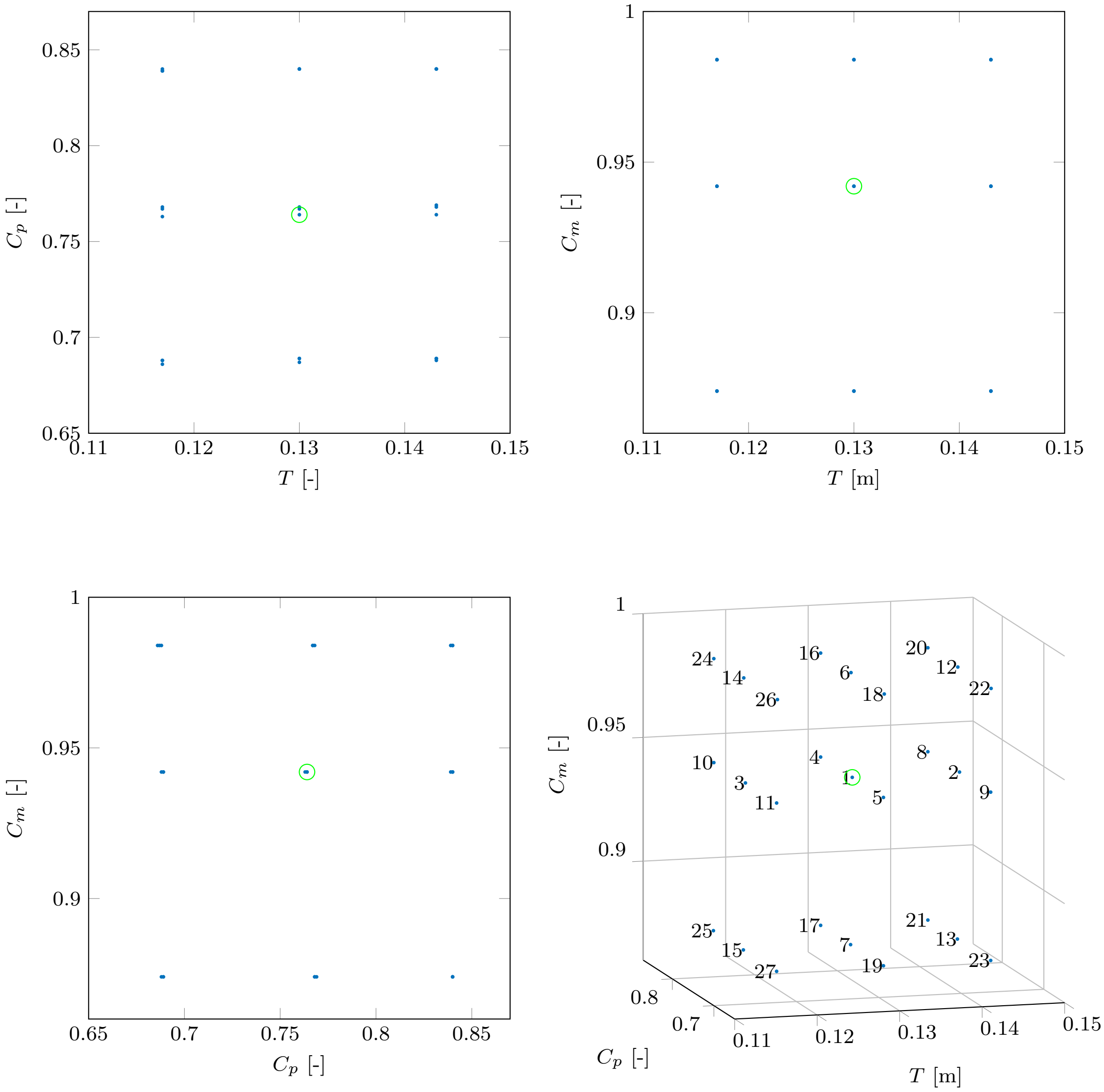

Figure 2-2: Scatter plots of varied parameters in the DSWAS, labels depicting model numbers, parent hull highlighted with ○

2-3 Selected models for validation

The Verification and Validation (V&V) analysis is conducted on three selected models from the DSWAS. The parent hull (model #1) is already available as towing tank model and two variations are newly built for this purpose: model #16 and model #19. The rationale behind selecting these particular models is:

- Model #16 ($C_p^+ C_m^+$) has a full form and long, sharp bilges. If present, it would be interesting to see if the strong vortices are well captured by the numerical method.
- Model #19 ($C_p^- C_m^-$) has a slender form and rounded bilges. Here the point of separation

may be hard to predict, if present at all. It would be interesting to see if the forces are validated and if possible deviations can be ascribed to this phenomena.

A profile comparison of the three models is given in Figure 2-3. For the complete linesplans, refer to Appendix B.

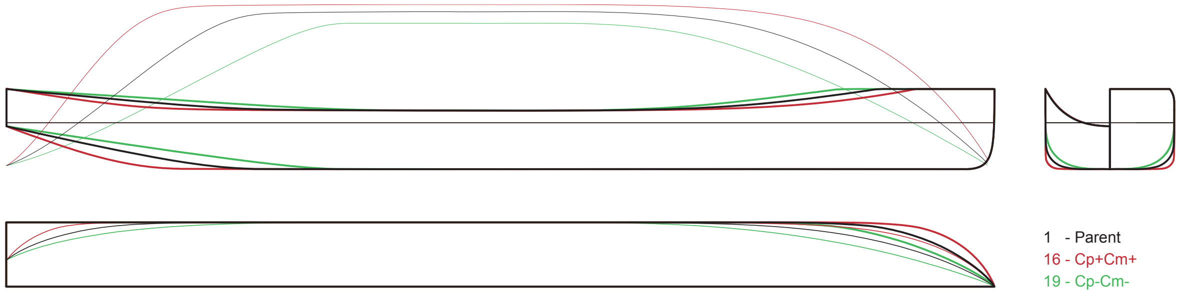

Figure 2-3: Profile comparison of the three selected vessels for validation

Chapter 3

Methods

In this chapter, the methods used for the experiments and numerical simulation are outlined. First, the used coordinate system for the experiments and computations is stated in section 3-1. Thereafter the experimental method is depicted in section 3-2 and the numerical method in section 3-3.

3-1 Coordinate system

In this work the coordinate system is defined with its origin at $\mathcal{O} = \begin{pmatrix} x_0 \\ y_0 \\ z_0 \end{pmatrix} = \begin{pmatrix} \text{⊗} \\ \text{℄} \\ \text{DWL} \end{pmatrix}$ as depicted in Figure 3-1. The side force component F_y of the hydrodynamic force is defined normal to the inflow. The resistance component F_x is defined parallel to the inflow, positive in the flow direction. The yaw moment M_z is taken about the vessel's midship section ⊗ (at $L/2$) rather than the centre of gravity G. This is done because ⊗ is a constant geometric position while the position of G varies per design. The yaw moment is defined in the same direction as the drift angle β, positive values indicating a destabilising moment.

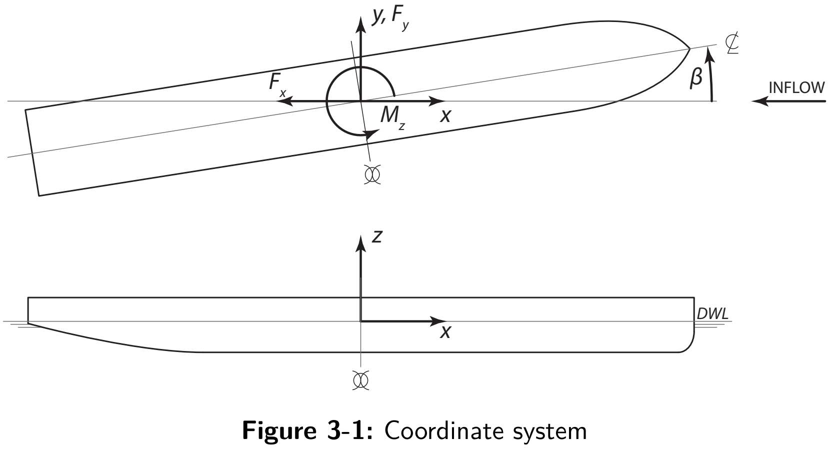

Figure 3-1: Coordinate system

Note that this decomposition is different from most manoeuvring publications where the x and y force components are decomposed in the *ship-fixed* coordinate system. The choice for using an *inflow-aligned* system has the following reasons:

- It is a common decomposition for sailing yacht tested in the towing tank.
- The y-component corresponds to the definition of lift (normal to inflow) and the x-component to the drag (parallel to inflow) as in aerodynamics.
- The ship-fixed decomposition as used in manoeuvring work is convenient for varying, large angles as seen in manoeuvres such as turning circles. In the current work, these angles remain small and are constant as only steady state conditions are considered.

3-2 Experimental method

For validation purposes, three geometries from the Delft Systematic Wind-Assisted Series (DSWAS) are tested on model scale in a towing tank. In this section the experimental method for these tests is treated.

3-2-1 Facility

The experiments are conducted in towing tank #1 at the Ship Hydromechanics laboratory of the TU Delft. Characteristics of this towing tank are listed in Table 3-1. The waterdepth during the experiments is 2.20 m and the average water temperature over all measurements is 17.0 °C.

Table 3-1: Towing tank characteristics

Length	142	m
Width	4.22	m
Maximum waterdepth	2.50	m
Maximum carriage velocity	8.00	m/s

3-2-2 Model

The models are built at a scale of $\alpha = 50$ in high density PU foam. Turbulence strips are fitted at three stations near the bow to ensure a fully turbulent boundary layer at the low Reynolds numbers at model scale. See Figure 3-3 for a photograph of the strips.

3-2-3 Measurement set up

The model is fixed to the towing carriage using a set-up commonly used by the laboratory for sailing yachts, see Figure 3-2. The model is fixed in the transverse y-direction by two balance arms (depicted in red), containing load cells for the two side forces F_f and F_a. The load cells are attached to the model with hinges. This allows the model to be fixed in sway and yaw, but free to surge, heave, pitch and roll. Due to the side force generated by the hull at a drift angle, a heel angle is induced when the model is brought up to speed. This heel angle is corrected while under way with a remote controlled weight travelling in ship-transverse direction.

The load cells used to measure resistance, side force forward and side force aft are all the same type, with a 5 kg maximum load, the smallest available in the SHS laboratory. Measured forces are in the range of $1 - 10\,\mathrm{N}$, which is about $2 - 20\%$ of the maximum load. This means that, especially at low measured forces, the signal to noise ratio can become an issue.

The position relative to the towing carriage is measured using an optical tracking system. This system uses three camera's in one armature monitoring a number of LEDs on the vessel in three dimensions. It then translates the signal into the vessel's motions in six degrees-of-freedom. During the measurements, the dynamic trim and sinkage due to forward velocity are monitored. The system also aids in aligning the model and obtaining an accurate reading for setting the heel angle.

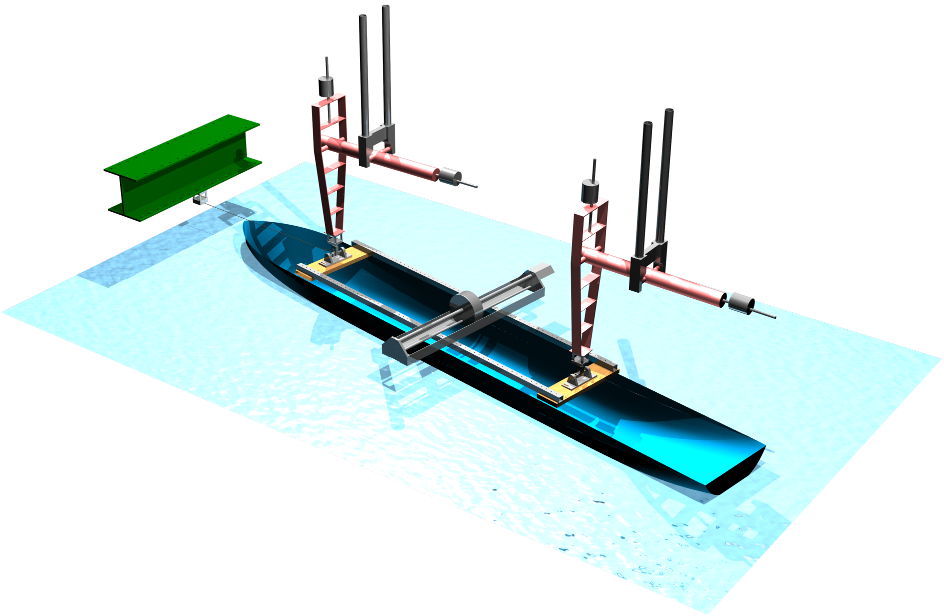

Figure 3-2: Experimental setup

3-2-4 Post processing

Strip correction The turbulence strips at the forward stations induce parasitic resistance. To be able to correct for this, the strip resistance is obtained by first doing a set of resistance runs with a single strip at each of the stations and another set with a second strip added at these stations, see Figure 3-3. Using the resulting difference in resistance, the strip resistance coefficient can be obtained and the measured resistance is corrected.

Raw signal processing At the tested velocities, measurements of about 60 s can be obtained. If necessary, the time traces of the forces are trimmed, typically resulting in $40 - 60\,\mathrm{s}$ of useful time trace. From this, the mean value is extracted for further processing.

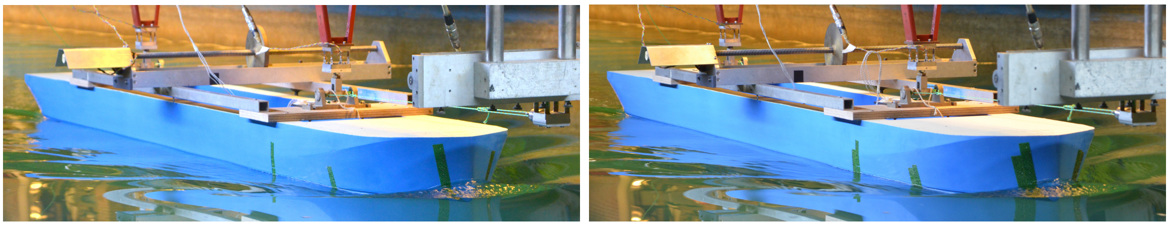

(a) Single strips **(b)** Double strips

Figure 3-3: Model #16 at $\beta = 0^{\circ}$ and $F_n = 0.168$

A notable observation from the time traces is an oscillatory resistance signal, corresponding to the oscillations in surge motion. At low resistance forces, the oscillation cuts off nears zero, meaning the towing line becomes slack. This will result in an erroneous mean. The timetraces are therefore trimmed such that this effect does not occur within the chosen selection for further processing.

Furthermore, the two side force signals contain a lot of noise. This can be explained by the fact that they are attached more rigidly to the towing carriage than the load cell for the resistance (via a towing line). As a consequence, the vibrations of the carriage affect the signal. However, the repeatability of the mean values is satisfactory, as is shown in section 4-1.

Data reduction After extracting mean values from the raw time traces, the measured forces are corrected by their respective zero measurement taken just prior to the run. For the resistance force, also the strip resistance is subtracted:

$$F_x = F_{x,meas} - F_{x,0} - F_{x,strip} \tag{3-1}$$

The effect of the strips on the side forces (forward and aft) is neglected, so:

$$F_f = F_{f,meas} - F_{f,0} \tag{3-2}$$

$$F_a = F_{a,meas} - F_{a,0} \tag{3-3}$$

The two side forces are then used to obtain the total side force F_y and yaw moment M_z about midship ⊗ :

$$F_y = F_f + F_a \tag{3-4}$$

$$M_z = (F_f D_f - F_a D_a)\cos\beta + F_x D_f \sin\beta \tag{3-5}$$

in which D_f and D_a are the distances between ⊗ and the forward and aft balance arms respectively, taken along the vessel's centreline.

3-3 Numerical method

In this section, the numerical study as performed with FINE/MARINE is outlined. The focus lies on the methods used and the choices made. For full derivations and numerical details one is referred to literature as stated. All computations are done at model scale. Refer to Table 2-3 for model particulars of the selected V&V models (#1, #16 and #19).

3-3-1 Governing equations

The numerical simulations are performed using the FINE/MARINE package of NUMECA. This implements the ISIS-CFD flow solver, developed by the Equipe Modélisation Numérique at the Ecole Centrale de Nantes. It is a Reynolds-averaged Navier-Stokes (RANS) solver using the Finite Volume Method (FVM). The governing equations are the incompressible Navier-Stokes equations:

$$\nabla \cdot \mathbf{u} = 0 \tag{3-6}$$

$$\frac{D\mathbf{u}}{Dt} + \nabla p - \frac{1}{Re}\Delta \mathbf{u} = 0 \tag{3-7}$$

which represent the conservation of mass and momentum respectively. On these equations, Reynolds decomposition is applied. This splits the velocity into a mean and fluctuating component:

$$\mathbf{u} = \bar{\mathbf{u}} + \mathbf{u}' \tag{3-8}$$

When Reynolds averaging is applied, one arrives at the RANS equations. As a result of this decomposition an extra set of terms known as the Reynolds stresses emerge. These stresses can then be solved using a turbulence model. For the full derivation one is referred to e.g. Pope (2000).

3-3-2 Spatial discretisation

To numerically solve the flow, the domain of interest needs to be discretised into grid cells. The FVM then treats each cell as a control volume, solving the flow properties for each of these volumes. To do this, the governing equations are discretised as well.

For the momentum equation a mixed order scheme called AVLSMART is used. This scheme switches between the third-order scheme QUICK and the second-order Upwind Differencing Scheme (UDS), depending on flow conditions (NUMECA, 2014).

For the mass fraction, the BRICS scheme is used. This scheme is an improved version of Blended Interface Capturing Scheme (BICS) which has proven itself for the solution of a free-surface with the Volume of Fluid (VOF) method. See section 3-3-7 for more details.

3-3-3 Temporal discretisation

Although the flow problem is considered as steady state, a time-marching approach is implemented to reach a steady state for the multi-fluid problem. For the mass fraction equation, a sub-cycling acceleration is implemented, allowing to solve the volume fraction several times during a global time step ΔT. This way, a larger global time step is made possible, reducing computation time of the simulation.

For all simulations, a maximum number of $N = 5$ sub-cycles is chosen with a target Courant number of $C_o = 5$. The default adopted time step is calculated as $\Delta T = N \cdot 0.01 \frac{L_{ref}}{V_{ref}}$ allowing for 100 time steps per cycle of flow along the hull. This yields $\Delta T = 0.158\,\mathrm{s}$. However, this gives convergence issues. After adjusting this time step to $\Delta T = 0.06\,\mathrm{s}$ stability is achieved. This time step is adopted for all computations.

3-3-4 Turbulence model

By using a RANS method, one does not need to resolve all turbulence scales. This greatly reduces computational time and it is the main reason to choose this method for the present work rather than e.g. Direct Numerical Simulation (DNS) which solves all turbulence scales.

As discussed, the RANS method averages the turbulent fluctuations. Consequently, a turbulence model is required to close the equations. Throughout the years, many different turbulent models have been developed, all based mainly on empiricism. In ship hydromechanics, the most commonly used models which are also available in FINE/Marine are:

- $k - \epsilon$ two-equation model
- $k - \omega$ two-equation models (Baseline (BSL) or Shear Stress Transport (SST))
- Explicit Algebraic Stress Model (EASM)
- Detached Eddy Simulation (DES)

Some initial calculations are performed trying out the different turbulence models. DES is not considered because of it's large computational intensity. The results are stated in Table 3-2. From this, one can conclude that the $k - \epsilon$ is not suitable for this type of simulation. EASM performs the best, but also requires the largest computation time. A recent survey of the application of turbulence models in ship hydromechanics (Larsson et al., 2013) shows $k - \omega$ SST as the most frequently applied turbulence model for steady state computations. It is known to deliver rather consistent and sufficiently accurate results for the required computation time. Considering the number of simulations needed, $k - \omega$ SST is chosen for it's common use, good references and consistent quality.

Table 3-2: Comparison error ($E = S - D$ [$\%D$]) for different turbulence models, model #1 at $\beta = 9°$ and $F_n = 0.168$

Trim & sinkage	Fixed				Free	
Turb. model	$k - \epsilon$	$k - \omega$ BSL	$k - \omega$ SST	EASM	$k - \omega$ SST	EASM
CPU time [min]	647	560	580	749	1223	1645
F_x	76%	-2%	-2%	3%	-1%	5%
F_y	159%	-7%	-6%	5%	-2%	11%
M_z	38%	4%	4%	2%	9%	7%

3-3-5 Trim and sinkage

In FINE/Marine it is possible to give a vessel any number of degrees of freedom. Using this, one can for example do a full six degrees of freedom simulation like a turning circle or a seakeeping simulation. For the current work however, a steady state computation is considered. In the towing tank, the model is then free to trim and heave, but fixed in all other degrees of freedom. To simulate this approach, one can let the trim and heave due to forward speed (sinkage) be solved.

From previous experiments with the appended parent hull, the trim and sinkage due to forward speed has been observed to be very small. Trim at $F_n = 0.168$ is about $\theta = 0.06°$, or $\tau = T_a - T_f = 2.9\,\mathrm{mm}$ ($\approx 2\%$ of T) and sinkage about $2\,\mathrm{mm}$ ($\approx 1.5\%$ of T). Table 3-2 shows the effect of fixing or solving trim and sinkage in the numerical simulation. The results are better matched with experiments if the trim and sinkage is solved, but convergence is observed to be about two times slower. The effect of trim and sinkage is therefore neglected and all simulations are done with a fixed model.

3-3-6 Wall treatment

The turbulence model makes use of wall functions for the near-wall region of the flow, reducing the required grid resolution in those areas as the flow needs not to be resolved through to the wall. A dimensionless wall distance is defined as:

$$y^+ \equiv \frac{u^* y}{\nu} \tag{3-9}$$

where u^* is the friction velocity at the wall, y the distance from the wall to the first cell and ν the kinematic viscosity of the fluid.

The first cell centre should be in the log-layer, therefore y^+ should be in the range of $30 \leq y^+ \leq 300$. However, the FINE/Marine package offers the flexibility of automatically switching to alternative functions if $y^+ < 30$. The input y^+ is therefore chosen as 30 for the reference 'medium' grid (see section 4-2-1).

3-3-7 Free surface treatment

FINE/Marine implements the VOF method for capturing the free surface. In this method, each fluid phase is designated a mass fraction of either 0 or 1. The free surface is then defined at a value of 0.5. The mass fraction is solved using an extra transport equation, similar to that of the mass transport equation. The BRICS scheme is used for solving this equation. The main advantage of this method is that the grid cells do not need to deform when the free surface deforms. The volume fraction is solved on the existing grid where *a priori* a refinement around the initial free surface ($z = 0$) is applied.

3-3-8 Meshing strategy

NUMECA's meshing tool, Hexpress, is used to generate computational meshes from the CAD geometries. Hexpress generates a hexahedral unstructured mesh. The use of an unstructured mesh requires significantly less input time than a structured grid. This is preferred

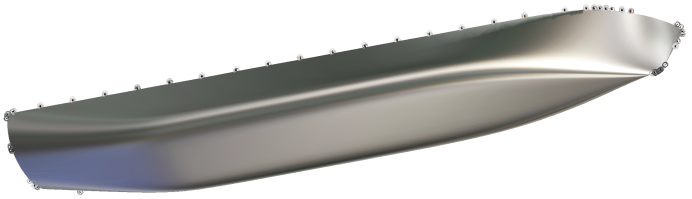

Figure 3-4: Highlighted cells with an orthogonality between $20°$ and $30°$ on a typical grid

for the current work since many grids need to be generated. A disadvantage of an unstructured mesh is that the grid quality is generally lower than that of a structured mesh, affecting the quality of the simulation.

The most important steps in the workflow can be summarised as follows:

1. Generate initial mesh, defining the global cell size.
2. Define refinements in certain regions. This can be a surface, line or a volumetric region.
3. Apply a boundary layer inflation mesh using a desired y^+ value per surface.

The program takes care of 'snapping' the mesh to the geometry surface as well as an optimisation step for fixing cells that are twisted, negative, concave or skewed. It is also capable of maintaining a minimum level of orthogonality. Throughout all used grids no twisted, negative, concave or skewed cells are present. A minimal orthogonality threshold of $10°$ was imposed, resulting in only a few orthogonalities of about $20°$ occurring at sharp corners such as bow, transom and deck line. Figure 3-4 depicts cells between $20°$ and $30°$ orthogonality on a typical grid.

The most important decisions in meshing strategy that remain are:

1. How fine to set the global cell size?
2. Where to put refinements? And how fine to set the target cell size?
3. Which y^+ value to adopt?

The decisions in these settings are based on best practices like the ones stated in ITTC (2011) and WS Atkins Consultants (2002) as well as best practices learned from colleagues and trial-and-error exercises on the parent hull, using existing experimental data as a reference. The lessons learned from these led to the choices for mesh sizes, y^+ and solver setup. A summary of grid settings is displayed in Table 3-3.

Table 3-3: Summary of grid settings, values for half domain (used for $\beta = 0$ cases) between parentheses

	non dimensional	dimensional [m]
Computational domain	$5 \times 3(1.5) \times 2\ L_{pp}$	$13.8 \times 8.28(4.14) \times 5.52$
Global cell size	$15 \times 9 \times 6\ (20 \times 6 \times 8)$	0.92 (0.69)
Surface refinements:	no. of refinements	resulting cell size
Hull	7	7.19×10^{-3}
Transom	6	1.44×10^{-2}
Deck	4	5.75×10^{-2}
Free surface	9	$0.552 \times 0.552 \times 0.00276$
Free surface triangle	9	$0.138 \times 0.138 \times 0.00276$
Curve refinements:		
Bow	8	3.59×10^{-3}
Transom	8	3.59×10^{-3}
Viscous Layer:	$y^+ = 30$	$y_{wall} = 1.06 \times 10^{-3}$
Typical total amount of cells:	$1.2 \times 10^6\ (0.73 \times 10^6)$	

3-4 Test conditions

Range of conditions The range of test conditions is chosen from expected operating conditions for Wind-Assisted Ship Propulsion (WASP) vessels. Because no such vessel operates today, a forecast is made. The current concept for the *Ecoliner* is designed for a service speed of $V_s = 12\,\text{kn}$ full scale, corresponding to $V_m = 0.873\,\text{m/s}$ at model scale or a Froude number of $F_n = 0.168$. Expected drift angles are somewhat more difficult to asses. It is greatly dependent on the ratio between thrust delivered by the rig and the engine. If a vessel is mostly engine propelled and the forward speed is somewhat high, the side force from the rig is relatively small and together with the forward speed, only a small drift angle is needed to counteract the side force hydrodynamically. If however, the concept tends more towards a mainly wind-driven vessel with low operating speeds and relatively higher side forces from the rig, the drift angle could be significantly larger. For the current work, a maximum drift angle of $\beta = 9°$ is chosen. Although quite large for a sailing vessel, it offers some margin to prevent the need for extrapolation outside the data set in future work.

The influence of heel is not taken into account, for its effect on the hydrodynamic forces is shown to be of a lower order than that of the drift angle (Wagner, 1967, Van Gastel, 1981, Fujiwara et al., 2005, Mobron, 2014, Struijk and Vogels, 2012). Consequently, for all tests $\phi = 0°$ applies.

Number of conditions To be able to do numerical simulations for all geometries of the series, a very limited set of test conditions is chosen. Because lift generation is assumed to be non linear with incidence angle β, two drift angles of $\beta = 3°$ and $9°$ are chosen next to straight ahead $\beta = 0°$. The drift cases are tested at the reference velocity corresponding to $F_n = 0.168$. The straight ahead resistance curve is given some resolution by adding two more velocities: $V_s = 9$ and 15kn ($F_n = 0.126$ and 0.210). This set of conditions is depicted as ‘Basic’ in Table 3-4.

The three selected geometries for Verification and Validation (V&V) (models #1, #16 and #19) are subject to an extended programme. For these geometries, a drift angle of $\beta = 6°$ is added to offer some more resolution for the relation of the hydrodynamic forces to the drift angle. Also, every drift angle is performed at all three velocities. This offers some more comparison material to the validation study. These conditions are depicted as 'Ext.' in Table 3-4.

For the uncertainty analysis, two conditions are marked (*): $\beta = 0°$ and 9° at the reference Froude number of $F_n = 0.168$. For these conditions, both repeat runs and grid studies are performed for the estimation of experimental and numerical uncertainty respectively. Refer to chapter 4 for more details.

Table 3-4: Overview of test conditions depicting basic and extended programme, the marked (*) cases are chosen for validation are subject to an uncertainty analysis

		$\beta =$			
V_s[kn]	$F_n[-]$	0°	3°	6°	9°
9	0.126	Basic	Ext.	Ext.	Ext.
12	0.168	Basic*	Basic	Ext.	Basic*
15	0.210	Basic	Ext.	Ext.	Ext.

Chapter 4

Uncertainty Estimation

The reliability and accuracy of the numerical simulations is evaluated by a Verification and Validation (V&V) analysis. In CFD, verification is about *solving the equations right*, assessing the uncertainties in the results. Validation is about *solving the right equations*, assessing the suitability of the numerical model for the physical problem at hand. For validation, knowledge of the uncertainty levels of both the experimental reference data and the numerical result is required. Section 4-1 treats the method and results of the experimental uncertainty estimation while section 4-2 does so for the numerical uncertainty.

The uncertainties are determined for the selected models #1, #16 and #19 as depicted in section 2-3. The selected conditions are $\beta = 0°$ and $\beta = 9°$ both at the reference Froude number of $F_n = 0.168$ as given in Table 3-4. The obtained relative uncertainty levels from these cases are then applied to the rest of the comparison material from the extended test programme($\beta = 3°$, $6°$ and $F_n = 0.126$ and 0.210).

4-1 Experimental uncertainty

For estimating the experimental uncertainty, the International Towing Tank Conference (ITTC) guidelines for uncertainty in resistance tests have been adopted (ITTC, 2014a,b,c,d). This method splits the estimation of elemental uncertainty into two categories:

- Type A: Uncertainty components obtained by *statistical analysis* of a series of observations.
- Type B: Uncertainty component obtained by *other means*, e.g. estimation based on previous experience.

Standard uncertainties are expanded to a 95% confidence level by a coverage factor K:

$$U_i = K u_i \tag{4-1}$$

For type A uncertainties, the coverage factor is taken from the student's t-distribution, to account for a limited sample size N (number of repeat measurements): $K = t_{95}(N-1)$. For type B uncertainties, a normal distribution is assumed. Therefore $K = 2$ applies.

After obtaining the expanded elemental uncertainties U_i (U_i' denoting a relative value), they propagate through sensitivity coefficients and are combined through Root of Sum of Squares (RSS) to build up the total uncertainty of the variable of interest.

4-1-1 Type A uncertainties

In typical resistance tests in towing tanks, the type A uncertainties one can obtain from statistical analysis are limited to the calibration of the load cells and the precision estimate from repeated measurements. Next to this, one should monitor the variations in the time signal.

Filtered time signal Although the time histories of the forces show significant fluctuation, after filtering with a low-pass cut-off frequency of 1.0 Hz the standard deviation of the filtered time history is around 0.3% of the mean value. Averaging over an interval of typically $\Delta t = 50\,\mathrm{s}$ with a sampling rate of $f_s = 50\,\mathrm{Hz}$ allows for a standard uncertainty of $0.3\%/\sqrt{50\,\mathrm{Hz} \cdot 50\,\mathrm{s}} = 0.006\%$. That is, the uncertainty of the data acquisition from the filtered time signal is negligible.

Load cell calibration The load cells are calibrated by applying a series of loads of a known weight W_i and recording the change in output voltage V_i at each step i. This is done while adding and subtracting the weights to check the presence of any hysteresis. The ratio between input weight and output voltage is determined for every step. The calibration factor K_g is then determined by taking the average over all steps of loading and unloading. The uncertainty in this factor for N steps is determined by the Standard Error Estimate (SEE) (Coleman and Steele, 2009):

$$u_{K_g} \equiv \mathrm{SEE} = \sqrt{\frac{\sum_{i=1}^{N}(W_i - K_g V_i)^2}{N-1}} \tag{4-2}$$

The load cells are re-calibrated at the end of the measurement programme to check for changes in the calibration factor. The resulting deviations in the calibration factor are taken into account in the uncertainty estimate. Especially the load cell for the resistance force showed some deviation over time and consequently carries the highest uncertainty: 0.031 N compared to 0.0087 N and 0.0045 N for the forward and aft side force load cells respectively.

Repeat measurements The precision of the measurements is quantified by considering the scatter from repeat measurements. The ITTC guidelines recommend $N = 10$ repeat measurements as a sample size. From these samples, the arithmetic mean $\overline{\phi}$ and the standard deviation s_ϕ of a quantity ϕ is calculated. For each geometry, the two selected V&V conditions have been repeated: $\beta = 0°$ and $\beta = 9°$, both at the reference Froude number of $F_n = 0.168$. This yields precision estimates for F_x at $\beta = 0°$ and F_x, F_f and F_a at $\beta = 9°$.

Figures 4-1, 4-2 and 4-3 give an overview of the results of models #1, #16 and #19 respectively. From these series runs 66, 98, 102, 174 and 202 were the first run of a day giving outlying result.

This is possibly due to lower turbulence levels in the tank compared to other measurements, affecting the results. These are thus excluded from further analysis.

Prior to run 88 the wave damping plank was used while backing up the carriage from the previous run. This was done to check its effect and indeed run 88 is an outlier. Using the plank did not reduce time waiting for the waves to die out. Instead it could have increased turbulence in the tank, causing the outlier. The plank is therefore not used and run 88 is excluded.

To check for any asymmetry of the model, set-up or other equipment half of the repeat measurements at $\beta = 9°$ has been performed at the mirrored angle $\beta = -9°$. For model #1 no systematic differences in results between these angles are observed, see Figure 4-1. For models #16 and #19 however, a bias in resistance is observed, see Figures 4-2 and 4-3. These differences are an order of magnitude larger than the differences within a series of measurements at one angle. The results for the side forces however are not systematically different, indicating no asymmetry in the model. This indicates some other source of error on the resistance measurement. The alignment of the model in the tank and with the resistance load cell has been checked and also re-built, yielding the same results. Thus, the source of error is unknown and the obtained precision limit is simply larger for these measurements.

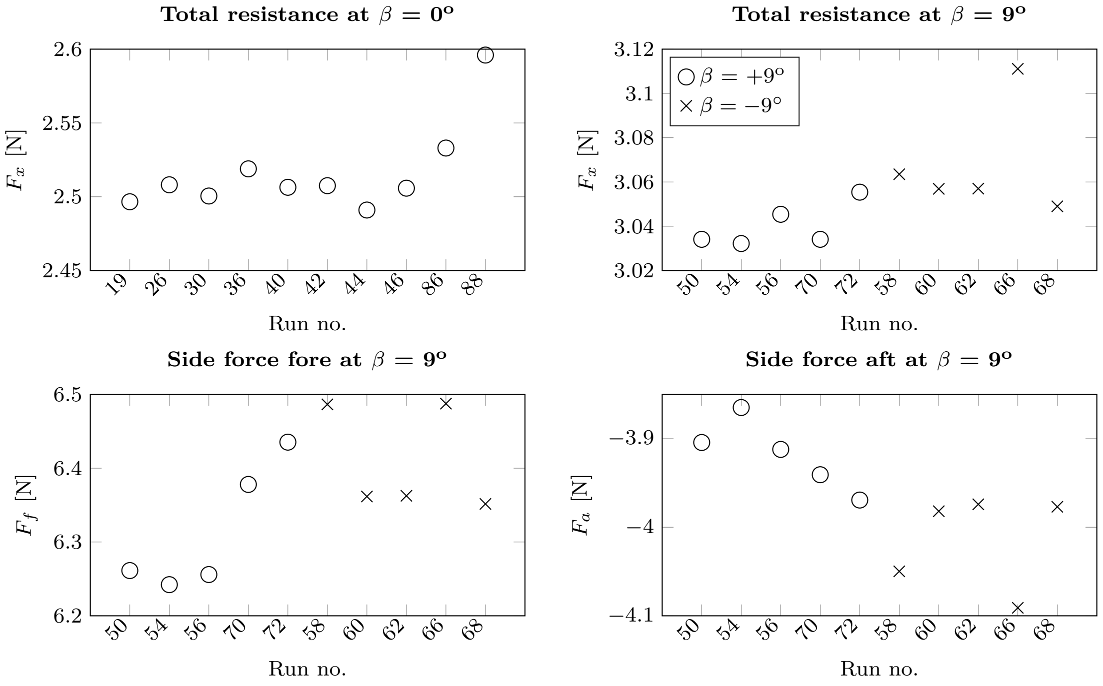

Figure 4-1: Results of repeat measurements for model #1

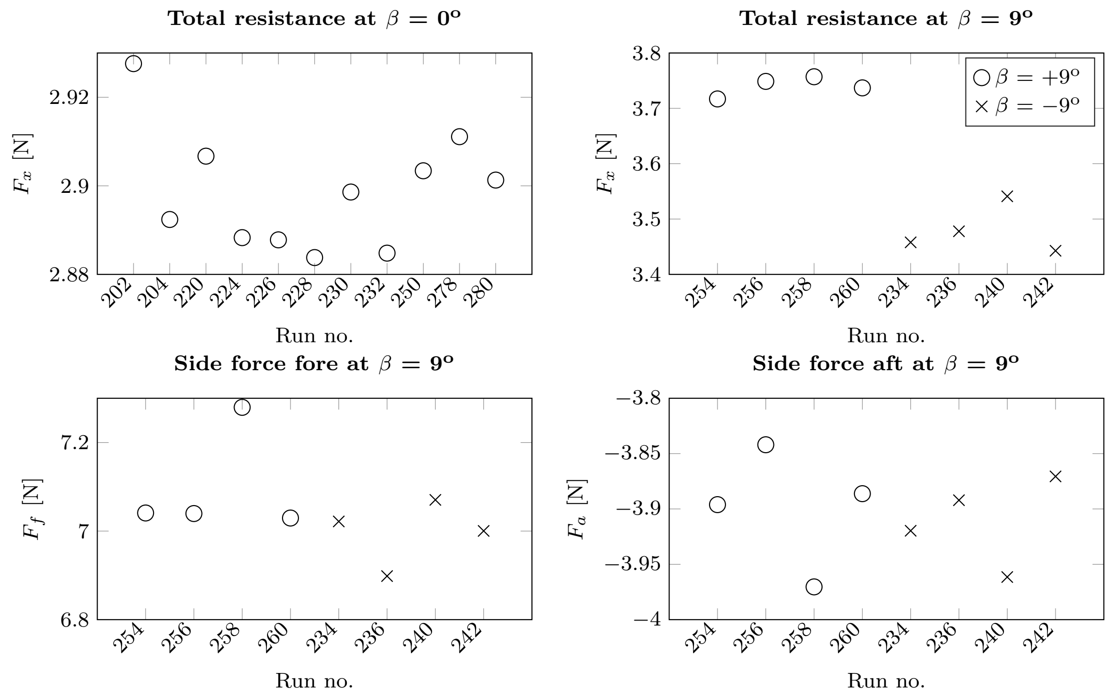

Figure 4-2: Results of repeat measurements for model #16

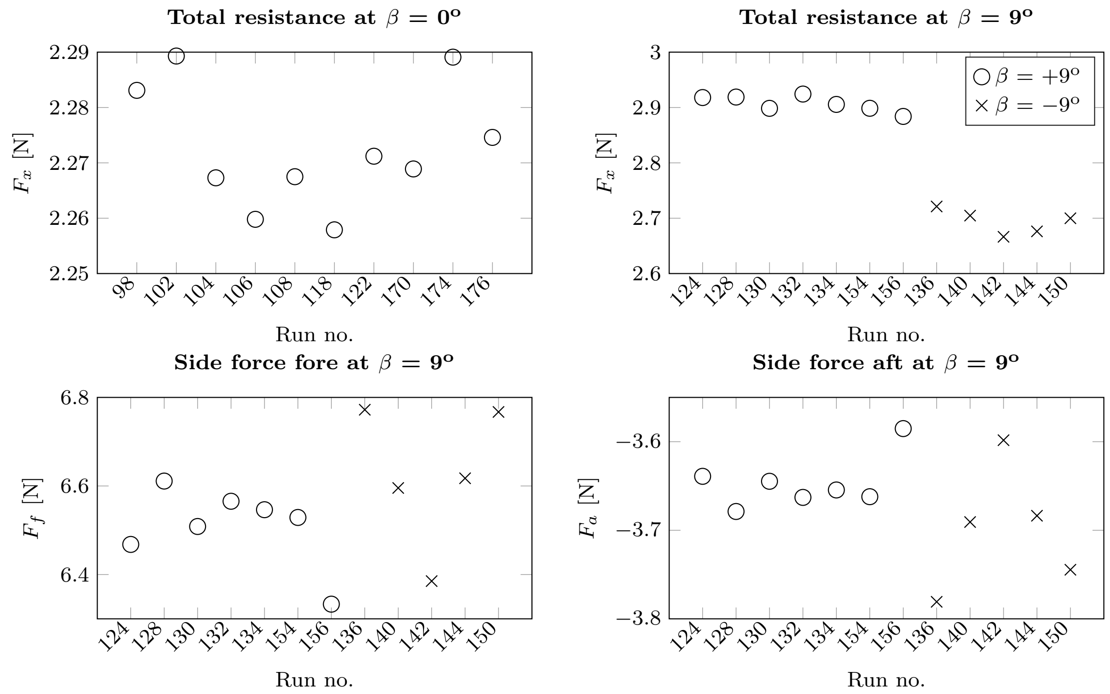

Figure 4-3: Results of repeat measurements for model #19

4-1-2 Type B uncertainties

Type B uncertainties originate from errors of various sources. They could consist of alignment errors, data reduction errors, test technique errors, etcetera. An estimation of different sources of errors is given below.

Environment The main environmental parameters of influence on the measurements are water density and viscosity. Both are determined from the water temperature using the ITTC equations (ITTC, 2011). The average water temperature over all measurements is recorded to be 17.0 °C. The deviation from this is ±0.6 °C. While this has negligible effect on the density (0.005%), the effect on viscosity is estimated as $u'_\nu = 0.87\%$ which propagates into the frictional resistance uncertainty.

Model displacement The models are ballasted using lead blocks. The accuracy of this procedure is dependent on the accuracy of the digital scale used to measure the model's mass. The limit bias of the used scale is ±0.05 kg. When assuming a uniform distribution the standard uncertainty becomes $u_\Delta = 0.05\,\mathrm{kg}/\sqrt{3} = 0.029\,\mathrm{kg}$.

Alignment The attitude of the vessel in still water is determined by four variables: trim, sinkage, roll and yaw. The still-water trim is set using draft indicators fore and aft (T_f and T_a). The precision of visually reading these is estimated as ±1 mm. For drift conditions the roll angle is set during a run because the vessel develops roll due to the generated hydrodynamic side force at a drift angle. It is adjusted by moving a remotely controlled weight in ship-transverse direction. The optical tracking system serves as an indicator. The error of this procedure is estimated as ±0.05°. The yaw angle is set before a run by adjusting the position of the balance arms. Also here, the angle can be read from the optical tracking system. The error of this is estimated as ±0.02°.

Strip resistance While necessary to ensure fully turbulent flow at model scale, the parasitic resistance from the turbulence strips is an unwanted quantity that needs to be determined in order to correct for. See section 3-2-4 for the determination of this quantity. Because one coefficient, constant over all velocities, is deduced and used in further processing, deviation in the obtained strip coefficients for different velocities is taken as a bias limit. This amounts to ±.0028 which is significant considering e.g. the value for model #16 of $C_{strip} = 0.00654$.

Carriage velocity The bias error in carriage velocity is quantified by taking the mean of the difference between the desired (input in up to three decimals) and measured carriage velocity over all runs. Deviations are observed to be ±0.001 m/s.

4-1-3 Uncertainty propagation

The uncertainties from elementary sources propagate through the data reduction equations. When considering a reduction equation of the form:

$$R = f(X_1, X_2, \ldots, X_j) \tag{4-3}$$

the partial derivatives of these elementary errors with respect to their elementary variable are computed as:

$$c_i = \frac{\partial R}{\partial X_i} \tag{4-4}$$

Then the uncertainty of the reduced variable R is computed as:

$$u_R = \sqrt{\sum_{i=1}^{J} (c_i u_i)^2} \tag{4-5}$$

The partial derivative c_i is also called the *sensitivity coefficient*, as it indicates the sensitivity of the reduced variable R to a certain elemental uncertainty.

Resistance The uncertainty components in the resistance are: strip resistance, load cell calibration, precision limits from repeat measurements, displacement, temperature and velocity. The uncertainty of the zero measurements is neglected. The propagation of these components is listed below:

- The strip resistance is determined as $F_{strip} = \frac{1}{2}\rho V_m^2 S_{strip} C_{strip}$. The sensitivity coefficient therefore reads $\frac{1}{2}\rho V_m^2 S_{strip}$.
- The load cell calibration uncertainty propagates with a sensitivity coefficient of 1, as does the repeatability uncertainty.
- The uncertainty in displacement propagates into the resistance as (ITTC, 2014c): $u'_\Delta(R_T) \approx \frac{2}{3} u'_\Delta$.
- The uncertainty in viscosity (due to variations in temperature) propagates as $u'_\nu(R_T) = \frac{C_{f,ITTC}}{C_T} \frac{0.87}{\log_{10} Re - 2} u'_\nu$, in which $C_{f,ITTC} = \frac{0.075}{(\log_{10} Re - 2)^2}$ is the ITTC-57 correlation coefficient.
- Assuming $R_T \propto V^2$, the sensitivity coefficient for the uncertainty in carriage velocity is 2.

Side force The uncertainty components in the side force are load cell calibration, precision limits from repeat measurements, displacement, temperature and velocity. The uncertainty of the zero measurements is neglected. These component propagate into the forward and aft side forces with the same sensitivity coefficients as in the resistance. The uncertainty of the total side force is then obtained by:

$$u(F_y) = \sqrt{[u(F_f)]^2 + [u(F_a)]^2} \tag{4-6}$$

Yaw moment Using the same uncertainty estimates for F_f and F_a and neglecting the uncertainty in the distances and angles, the combined uncertainty for the yaw moment becomes:

$$u(M_z) = \sqrt{[(u(F_f) D_f \cos\beta]^2 + [(u(F_a) D_a \cos\beta]^2 + [u(F_x) D_f sin\beta]^2} \tag{4-7}$$

which results in somewhat lower uncertainty values than those of the total side force because of a typical coefficient value of $0.7\,\mathrm{m} \cdot \cos(9°) \approx 0.7$. The relative uncertainties are even lower because of the higher values of yaw moment compared to side force.

4-1-4 Results

The uncertainties components propagating into the forces to be compared with CFD are listed in Tables 4-4, 4-5 and 4-6. From this it can be concluded that the calibration and strip resistance have the largest contribution to the total uncertainty. The effect of temperature, displacement and velocity is very minor. As is the precision estimate from repeat runs, with the exception for the resistance at drift for models #16 and #19. This is due to the asymmetry in the results for $\beta = 9°$ and $-9°$, which is not present at model #1, see section 4-1-1.

The total propagated experimental uncertainty estimates U_D are depicted in Tables 4-1, 4-2 and 4-3. The uncertainty in resistance F_x while sailing straight ahead ($\beta = 0°$) is 3% for model #16 and within 5% for models #1 and #19. The higher estimates are due to the larger uncertainty in strip coefficient. The uncertainty in resistance at drift is below 5% for all models, with the estimates of models #16 and #19 somewhat higher than that of model #1 due to the asymmetry of the results.

The uncertainty estimates for the side force F_y are quite consistent among the models and have values less than 5%. The uncertainties in yaw moment are around 1%, which is considered low.

Table 4-1: Experimental uncertainty estimates of model #1

	$\beta = 0°$	——— $\beta = 9°$ ———		
$\phi =$	F_x	F_x	F_y	M_z
$\bar{\phi}$	2.279	2.819	2.396	7.150
U_D	0.107	0.108	0.099	0.070
U_D [%D]	4.69%	3.82%	4.14%	0.97%

Table 4-2: Experimental uncertainty estimates of model #16

	$\beta = 0°$	——— $\beta = 9°$ ———		
$\phi =$	F_x	F_x	F_y	M_z
$\bar{\phi}$	2.764	3.479	3.143	7.575
U_D	0.083	0.163	0.131	0.092
U_D [%D]	3.00%	4.69%	4.18%	1.21%

Table 4-3: Experimental uncertainty estimates of model #19

	$\beta = 0°$	——— $\beta = 9°$ ———		
$\phi =$	F_x	F_x	F_y	M_z
$\bar{\phi}$	2.068	2.613	2.889	7.123
U_D	0.100	0.123	0.110	0.079
U_D [%D]	4.84%	4.71%	3.82%	1.11%

Table 4-4: Experimental uncertainty components of model #1

	—$\beta = 0°$—		$\beta = 9°$					
	R_T		R_T		F_f		F_a	
	U'	U	U'	U	U'	U	U'	U
Repeat runs	0.38%	0.0095	0.30%	0.0090	1.01%	0.0639	1.05%	0.0416
Calibration	2.64%	0.0662	2.17%	0.0662	0.29%	0.0185	0.24%	0.0095
R_{strip}	3.23%	0.0810	2.66%	0.0810				
Temperature	0.52%	0.0131	0.52%	0.0159	0.52%	0.0332	0.52%	0.0207
Displacement	0.04%	0.0010	0.04%	0.0013	0.04%	0.0026	0.04%	0.0016
Velocity	0.60%	0.0151	0.60%	0.0184	0.60%	0.0382	0.60%	0.0238

Table 4-5: Experimental uncertainty components of model #16

	—$\beta = 0°$—		$\beta = 9°$					
	R_T		R_T		F_f		F_a	
	U'	U	U'	U	U'	U	U'	U
Repeat runs	0.24%	0.0069	3.85%	0.1394	1.51%	0.1063	0.96%	0.0373
Calibration	2.29%	0.0662	1.83%	0.0662	0.26%	0.0185	0.24%	0.0095
R_{strip}	1.51%	0.0438	1.21%	0.0438				
Temperature	0.52%	0.0151	0.52%	0.0189	0.52%	0.0368	0.52%	0.0204
Displacement	0.04%	0.0012	0.04%	0.0015	0.04%	0.0029	0.04%	0.0016
Velocity	0.60%	0.0174	0.60%	0.0218	0.60%	0.0424	0.60%	0.0235

Table 4-6: Experimental uncertainty components of model #19

	—$\beta = 0°$—		$\beta = 9°$					
	R_T		R_T		F_f		F_a	
	U'	U	U'	U	U'	U	U'	U
Repeat runs	0.24%	0.0055	2.50%	0.0706	1.27%	0.0834	0.95%	0.0347
Calibration	2.92%	0.0662	2.35%	0.0662	0.28%	0.0185	0.26%	0.0095
R_{strip}	3.21%	0.0727	2.58%	0.0727				
Temperature	0.52%	0.0118	0.52%	0.0147	0.52%	0.0343	0.52%	0.0192
Displacement	0.04%	0.0009	0.04%	0.0012	0.04%	0.0027	0.04%	0.0015
Velocity	0.60%	0.0137	0.60%	0.0170	0.60%	0.0395	0.60%	0.0221

4-2 Numerical uncertainty

To estimate the uncertainty of the numerical simulations, a verification analysis is performed. As part of a V&V analysis, the ITTC (2002) guidelines are followed. Also the guidelines from American Society of Mechanical Engineers (ASME, 2009), which are an ANSI standard follow a similar approach.

The approach of these guidelines consists of two main steps: code verification and solution verification. Code verification ensures that the problem is correctly modelled in the numerical software. This may involve rigorous testing of the code on different benchmark problems and is thus considered to be out of scope of the current work. Moreover, commercial codes are subject to such studies prior to release. For a code verification example of the ISIS-CFD flow solver as implemented in FINE/MARINE, one is refered to the work of Deng et al. (2006).

For solution verification, the numerical simulation uncertainty U_S of a solution is estimated. This uncertainty is driven by errors from different sources: round-off errors, iterative errors and discretisation errors. The round-off errors are considered to be negligible due to the use of double-precision by the flow solver (Rijpkema and Vaz, 2011). After letting all residuals level out or drop by two orders in magnitude and if the solution does not change any more, the solution is considered to be converged. See Figure 4-4 for a typical convergence history.

The resulting forces are extracted by taking the average from the last 10 s from the convergence history. The standard deviation in the forces of this segment is typically less than 0.1% of the mean value. Its contribution to the numerical uncertainty is therefore considered to be negligible (Eça and Hoekstra, 2009).

4-2-1 Discretisation uncertainty

With the round-off error and iterative error declared negligible, the sole contribution to the numerical simulation uncertainty is the discretisation (or: grid) uncertainty: $U_S = U_G$. For estimation of this uncertainty, a grid convergence study is performed. The effect of varying the cell size on the hydrodynamic forces F_x, F_y and M_z is then examined.

A typical cell size is defined using the ratio between the domain volume and the number of cells as: $h = \sqrt[3]{\frac{V_D}{N}}$. The different grids should be geometrically similar to not include any other effects than the varying cell size. In an unstructured grid as the ones used this is difficult to achieve. The grid variations are constructed by changing the initial cell size, leaving the amount of refinements the same. Also the y^+ value and free surface refinement is scaled accordingly to preserve the cell's aspect ratio.

A series of six grids is constructed for every V&V case. The refinement factor is advised to be $r = \frac{h_{i+1}}{h_i} = \sqrt[3]{2} \approx 1.26$, resulting in a double amount of cells for each step in the 3-D case. However, applying this in HEXPRESS resulted in a somewhat lower factor due to discrete steps in the meshing process. The result is a typical amount of cells of 3.6, 2.5, 1.8, 1.2, 0.9 and 0.8 million from fine to coarse, the reference grid ('medium') containing 1.2 million cells. In case of $\beta = 0°$, a half domain is used. In that case, the amount of cells are about 2.4, 1.6, 1.1, 0.72, 0.63 and 0.56 million. See Figure 4-5 for a series of typical grid topologies.

The discretisation error can be estimated with Richardson Extrapolation (RE) and the Grid Convergence Index (GCI) method. This implies fitting a power series to the results per grid,

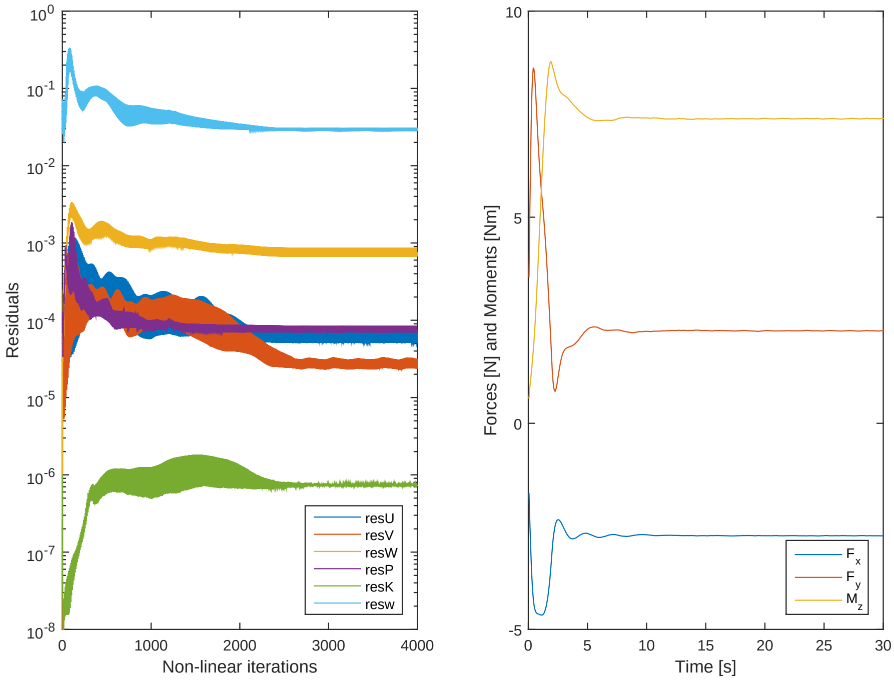

Figure 4-4: Typical iterative convergence, model #1 at $\beta = 9^\circ$ and $F_n = 0.168$

obtaining the following error estimate:

$$\epsilon_\phi \cong \delta_{RE} = \phi_i - \phi_0 = \alpha h_i^p \tag{4-8}$$

Here ϕ_i is the solution on grid i, ϕ_0 the estimate of the exact solution by extrapolation, α a grid constant, h_i the typical cell size and p the observed order of convergence.

For the power series, a weighted least-square fit is used with $\frac{1}{h_i}$ as weights to express more confidence in finer grids (Eça and Hoekstra, 2013). The fit returns the observed order p which is used to determine the uncertainty U_G at 95% confidence level by the GCI as:

$$U_S = \text{GCI}_{med} = F_s \left| \frac{\epsilon_{med}}{r_{med}^p - 1} \right| \tag{4-9}$$

with $r_{med} = \frac{h_{med}}{h_1}$ and a safety factor of $F_s = 1.25$. The discretisation error ϵ is calculated for the reference grid (dubbed 'medium') as:

$$\epsilon_{med} = \frac{\phi_{med} - \phi_1}{\phi_1} \tag{4-10}$$

with ϕ_1 being the solution on the finest grid.

Note:
The extrapolation with a power fit works under the assumption of a well-behaved dataset with a good fit and an observed order close to the formal order. In case of an ill-behaved

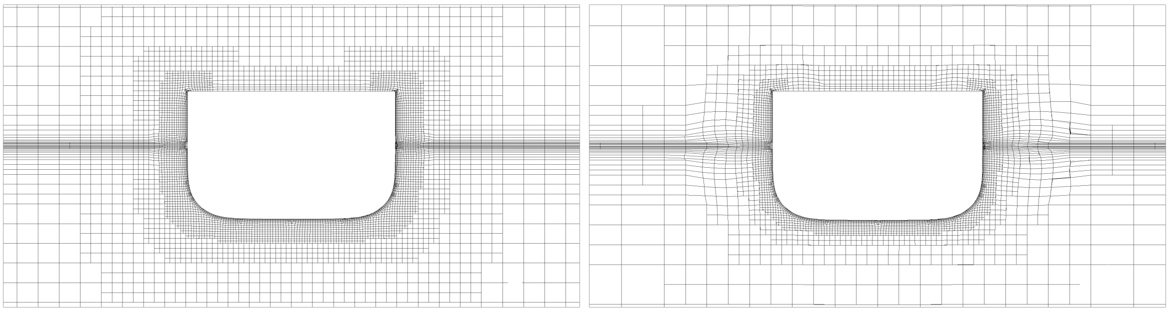

(a) Grid 1 **(b)** Grid 2

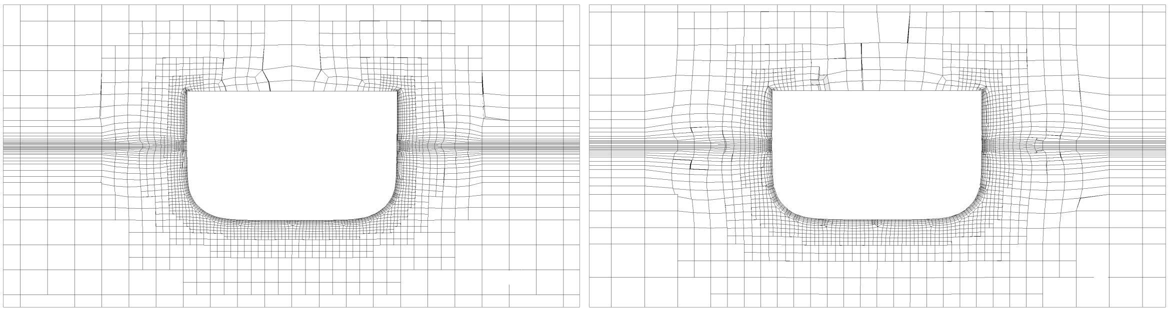

(c) Grid 3 **(d)** Grid 4

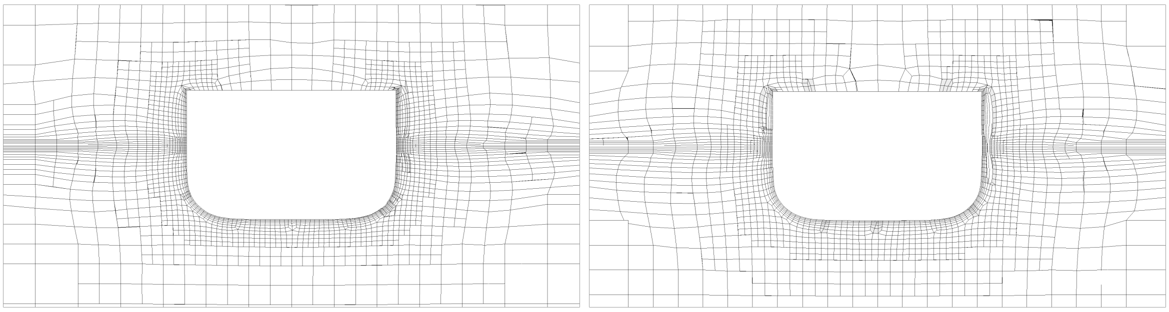

(e) Grid 5 **(f)** Grid 6

Figure 4-5: Different grid densities as used in the grid convergence study, cross section at midship

dataset (large scatter, non-monotonic convergence), Eça and Hoekstra (2014) recommend fitting with with a polynomial of the formal order of accuracy rather than a power series. In case of a non-monotonic convergence, for a second-order accurate scheme, the error estimate is obtained with a polynomial fit:

$$\epsilon_\phi \cong \phi_i - \phi_0 = \alpha_1 h_i + \alpha_2 h_i^2 \tag{4-11}$$

To express the lower confidence in the data, a larger safety factor of $F_s = 3$ is adopted.

4-2-2 Results

Model #1 Figure 4-6 depicts the results of the grid study for model #1. The grid convergence yields a fair fitted extrapolation ($R^2 \approx 0.98$ for all but F_y, which is slightly more poor with $R^2 \approx 0.94$) when neglecting some outliers in the coarse-grid region. These outliers could be an indication that these solutions are out of the asymptotic range.

An overview of the results of the grid convergence is given in Table 4-7. Here one can observe that the F_y extrapolation carries the highest numerical uncertainty estimate of 4.2%.

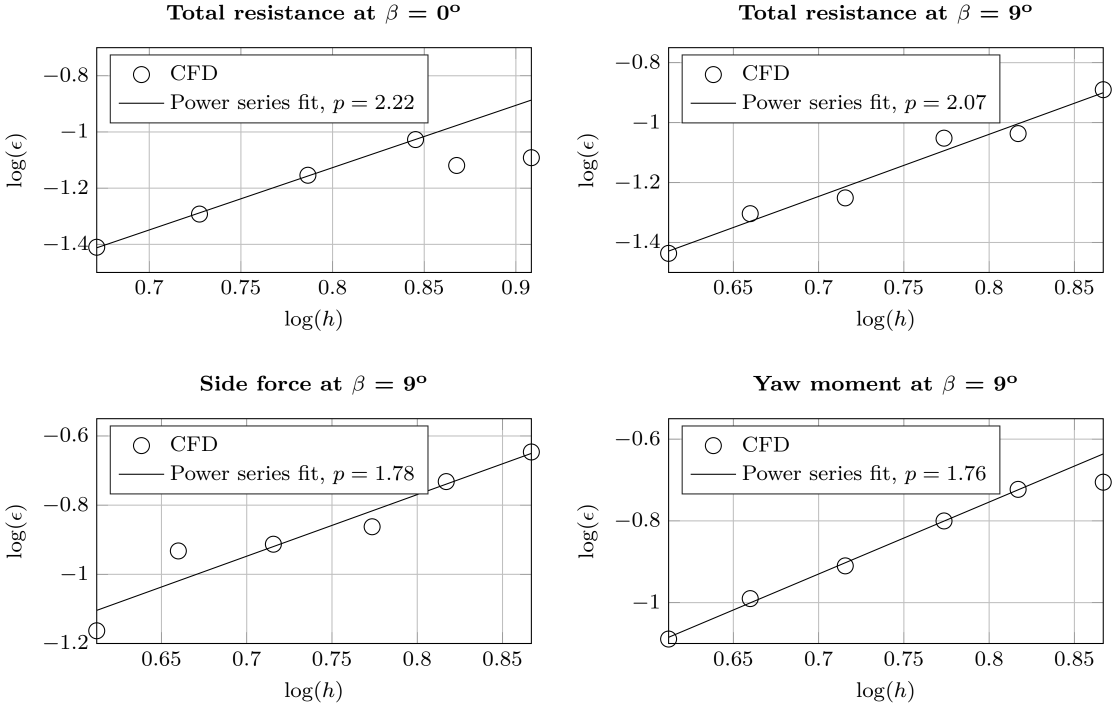

Figure 4-6: Error ($\epsilon = \phi_i - \phi_0$) versus grid spacing h on a log-log scale, model #1

Table 4-7: Numerical uncertainty of model #1

	$\beta = 0°$	$\beta = 9°$		
	F_x	F_x	F_y	M_z
ϕ_{ext}	2.246	2.671	2.123	7.267
p	2.217	2.073	1.781	1.760
ϵ_{med}	0.024	0.019	0.031	0.010
U_S [%S] = GCI	2.35%	2.07%	4.17%	1.42%

Model #16 For three out of four results in Figure 4-7, the power series is well fitted to the data with $R^2 \approx 0.93 - 0.99$ when neglecting outliers and the observed orders are in a plausible range. For F_y however, it proves to be more difficult to fit a power series extrapolation. The fit is more poor with $R^2 \approx 0.83$ and the observed order is out of theoretical range with $p = 0.32$. This ill-behaved dataset is thus fitted with a second-order polynomial fit, following Eça and Hoekstra (2014). The GCI is calculated with a larger safety factor of $F_s = 3$. This results in an uncertainty estimate of 5.8%, see Table 4-8.

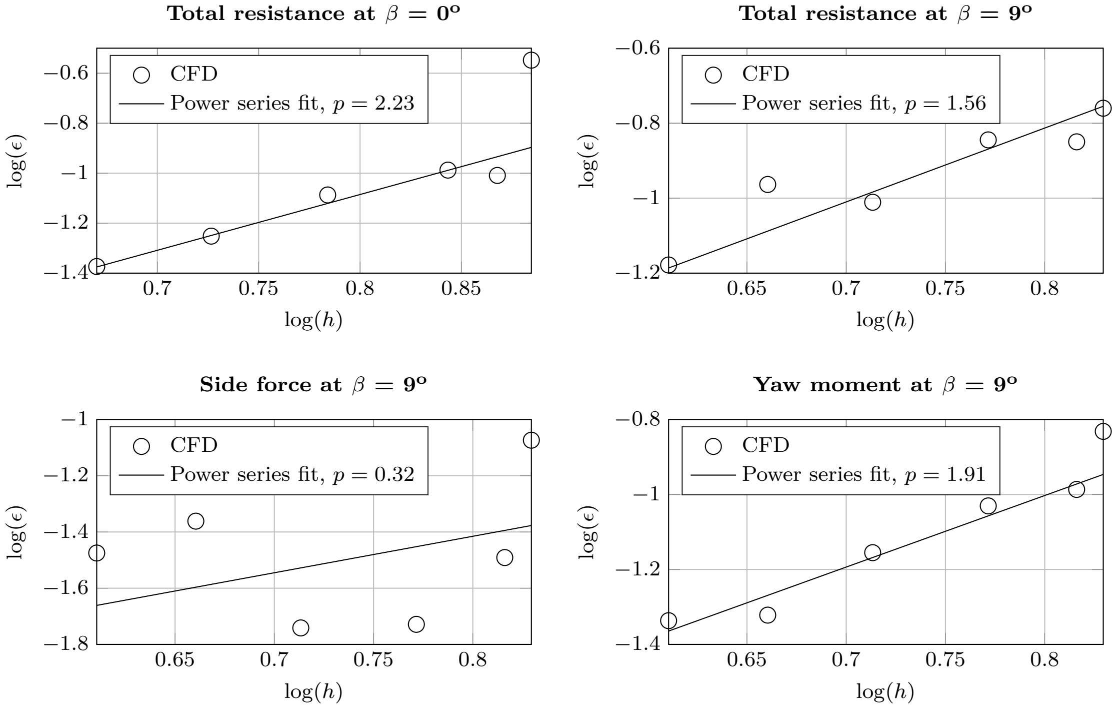
Total resistance at β = 0°

Total resistance at β = 9°

Side force at β = 9°

Yaw moment at β = 9°

Figure 4-7: Error ($\epsilon = \phi_i - \phi_0$) versus grid spacing h on a log-log scale, model #16

Table 4-8: Numerical uncertainty of model #16

	$\beta = 0°$		$\beta = 9°$	
	F_x	F_x	F_y	M_z
ϕ_{ext}	2.634	3.147	2.845	7.600
p	2.232	1.585	0.318	1.908
ϵ_{med}	0.023	0.024	-0.005	0.006
U_S [%S] = GCI	2.20%	3.73%	5.82%	0.75%

Model #19 Fitting the data with a power series for F_y yields a very poor fit of $R^2 \approx 0.43$ whereas the rest of the results has a better fit of around $R^2 \approx 0.99$ when neglecting some outliers in the coarse grid region, see Figure 4-8. Therefore, also here F_y is fitted with a second-order polynomial and a safety factor of $F_s = 3$ is applied. All GCI values are within 2%.

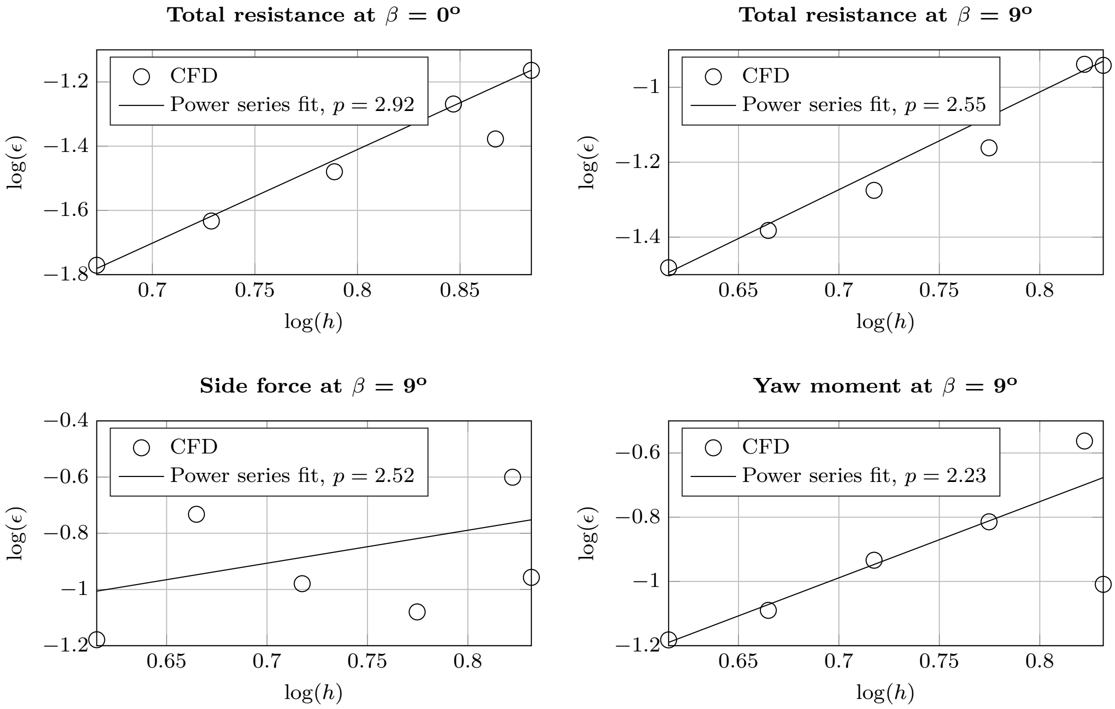

Figure 4-8: Error ($\epsilon = \phi_i - \phi_0$) versus grid spacing h on a log-log scale, model #19

Table 4-9: Numerical uncertainty of model #19

	$\beta = 0^\circ$	$\beta = 9^\circ$		
	F_x	F_x	F_y	M_z
ϕ_{ext}	2.004	2.441	2.670	7.161
p	2.915	2.551	2.519	2.371
ϵ_{med}	0.018	0.015	0.006	0.012
U_S [%S] = GCI	1.19%	1.17%	1.75%	1.09%

Chapter 5

Validation

In this chapter, validation of the numerical method is performed using the experimental data. Having obtained both method's uncertainties in chapter 4, the comparison error is evaluated and compared to the validation uncertainty level.

The accepted level of uncertainty is application dependent. For this work, the numerical results will be used to develop formulations for a concept evaluation tool in the form of a Performance Prediction Programme (PPP). For this application, a lower level of accuracy is acceptable than for a final design evaluation.

5-1 Method

As part of a Verification and Validation (V&V) analysis, the approach on validation follows the same ITTC guidelines as the numerical verification in section 4-2 (ITTC, 2002). To validate the solution, a comparison error E and validation uncertainty U_{val} are evaluated. The comparison error is simply the difference between the simulation value S and experimental value D:

$$E = S - D \tag{5-1}$$

The validation uncertainty U_{val} is a Root of Sum of Squares (RSS) of the experimental uncertainty U_D and numerical uncertainty U_S:

$$U_{val} = \sqrt{U_D^2 + U_S^2} \tag{5-2}$$

Using the comparison error E and the validation uncertainty U_{val} the validation statements is defined as:

1. $|E| < U_{val}$: the modelling error of the numerical method is within the noise level of U_{val}. The solution is validated at a level of U_{val}.
2. $|E| > U_{val}$: the modelling error is larger than the noise of U_{val}, i.e. the experimental solution is outside the uncertainty band and the solution is therefore not validated.

5-2 Results

The validation results for the three selected models (#1, #16 and #19) are discussed in this section. The V&V conditions ($\beta = 0°$ and $9°$ at $F_n = 0.168$, see Table 3-4) are treated in detail, comparing their uncertainty estimates with the comparison error. Applying these relative uncertainties to the other comparison data, a broader view of the comparison between the methods is given over the full range of results using errorbar plots.

Model #1 Table 5-1 gives the validation results. For the experimental uncertainty, F_x carries the highest uncertainty of 4.7% and 3.8% at $\beta = 0°$ and $\beta = 9°$ respectively. This originates largely from the uncertainties in strip correction and load cell calibration. For F_y and M_z, the contributions from U_D and U_S are more equal.

The resistances at $\beta = 0°$ and $9°$ are validated at an uncertainty level of around $4-5\%$ which is an acceptable accuracy. The comparison error E for F_y is slightly smaller than its validation uncertainty U_{val}. This result is validated at an uncertainty level of about 6%.

M_z is not validated, mostly because of the very low estimate for U_{val} of 1.7%. Although the comparison error of 3.9% still seems acceptable, the V&V method rejects the validation. This leaves to question the V&V method and the obtained uncertainty levels.

Table 5-1: Validation of model #1

	$\beta = 0°$	$\beta = 9°$		
	F_x	F_x	F_y	M_z
D	2.279	2.819	2.396	7.150
S	2.340	2.760	2.260	7.426
$E = S - D$ [%D]	2.67%	-2.09%	-5.65%	3.86%
U_D [%D]	4.69%	3.82%	4.14%	0.97%
U_S [%S]	2.35%	2.07%	4.17%	1.42%
U_{val} [%S]	5.14%	4.42%	6.05%	1.70%
Validated?	✓	✓	✓	✗

Figure 5-1 shows all experimental and numerical results for model #1 in one plot while Table 5-2 gives the numeric values of comparison error E. The errorbars are constructed from the obtained relative uncertainties in the V&V procedure. Here one can see that although there are some differences in F_x, the errorbars show overlap and both methods are in close agreement. At $\beta = 0°$ the values show larger deviations of $3-4\%$ for $F_n = 0.168$ and 0.210. In general one can observe that for F_x the experimental result show a more linear behaviour at low drift angles β while the CFD results show a little more curvature. However, it must be noted that all of these nuances occur within errorbar range.

The comparison errors of F_y are larger than those for F_x. Expressed in percentage they are a lot larger at smaller drift angles due to lower force magnitudes. The results for M_z show very good agreement with low values of E. The point of V&V exercise ($\beta = 9°$, $F_n = 0.168$) shows an unfortunate large mismatch. Other points in the dataset show a better comparison.

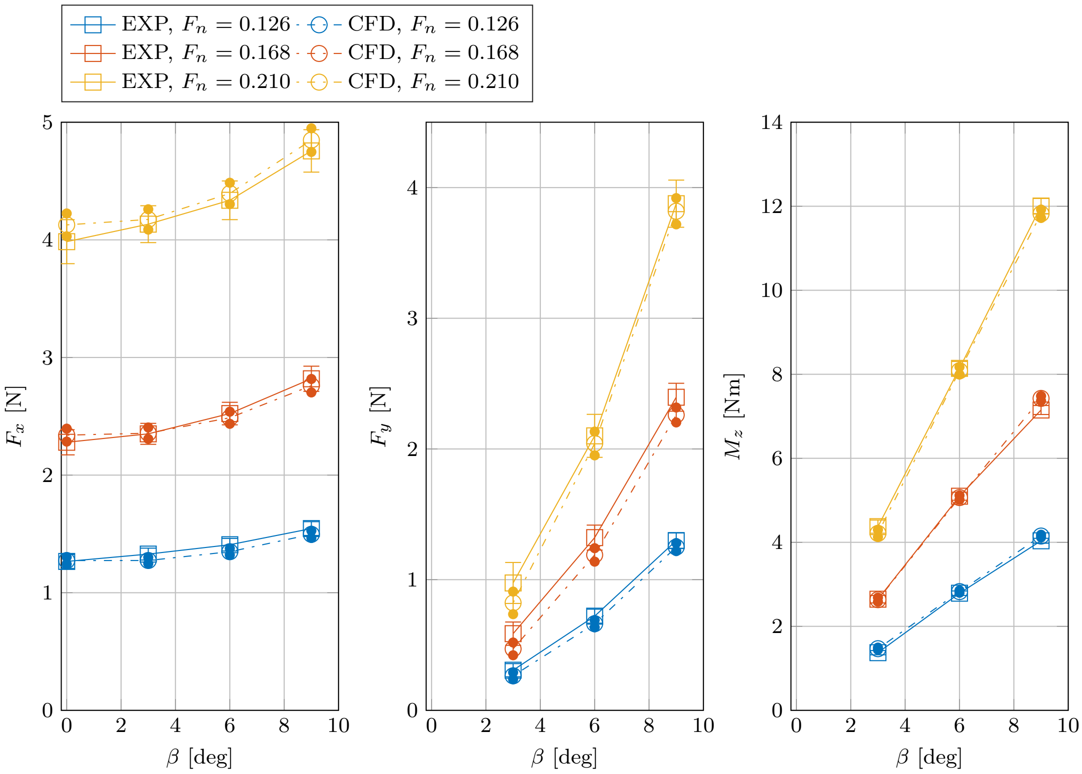

Figure 5-1: Comparison experimental and numerical results, model #1, solid dots depict errorbars for CFD cases

Table 5-2: Comparison errors ($E = S - D$ [$\%D$]) of model #1

		$\beta =$			
	F_n	0°	3°	6°	9°
F_x	0.126	0.59%	-4.10%	-4.23%	-3.17%
	0.168	2.67%	0.23%	-1.41%	-2.09%
	0.210	3.58%	0.97%	1.34%	1.93%
F_y	0.126		-13.99%	-7.99%	-3.82%
	0.168		-19.83%	-10.01%	-5.65%
	0.210		-15.63%	-2.78%	-1.49%
M_z	0.126		6.90%	1.38%	2.80%
	0.168		-0.42%	-0.64%	3.86%
	0.210		-3.69%	-0.70%	-1.53%

Model #16 Table 5-3 gives the validation results for model #16. The total resistance F_x is validated for $\beta = 0°$ and $\beta = 9°$ at U_{val} levels of 3.7% and 6.2% respectively. F_y and M_z are not validated. The main driver for F_y is the large comparison error E of almost 10%. For M_z the low uncertainty estimate prevents validation even though the comparison error is rather small.

Table 5-3: Validation of model #16

	$\beta = 0°$	$\beta = 9°$		
	F_x	F_x	F_y	M_z
D	2.764	3.479	3.143	7.575
S	2.737	3.290	2.831	7.693
$E = S - D$ [%D]	-1.00%	-5.42%	-9.91%	1.55%
U_D [%D]	3.00%	4.69%	4.18%	1.21%
U_S [%S]	2.20%	3.73%	5.82%	0.75%
U_{val} [%S]	3.74%	6.20%	7.44%	1.41%
Validated?	✓	✓	✗	✗

Considering the values for all comparison material in Table 5-4, rather large comparison errors exist for all values of F_y. Figure 5-2 shows deviations out of errorbar range (more than 10%) with low force values showing very large percentages for E. F_x is predicted more accurately, with E in most cases within 10%. M_z yields the best results with E mostly within 3%.

Table 5-4: Comparison errors ($E = S - D$ [%D]) of model #16

		$\beta =$			
	F_n	0°	3°	6°	9°
F_x	0.126	-3.19%	-8.00%	-10.11%	-2.61%
	0.168	-1.00%	-4.70%	-8.00%	-5.42%
	0.210	0.85%	-2.36%	-5.10%	0.79%
F_y	0.126		-42.23%	-25.68%	-8.47%
	0.168		-32.74%	-27.73%	-9.91%
	0.210		-37.02%	-17.79%	-9.54%
M_z	0.126		-2.41%	-0.89%	11.77%
	0.168		2.00%	-4.68%	1.55%
	0.210		-2.03%	2.75%	6.16%

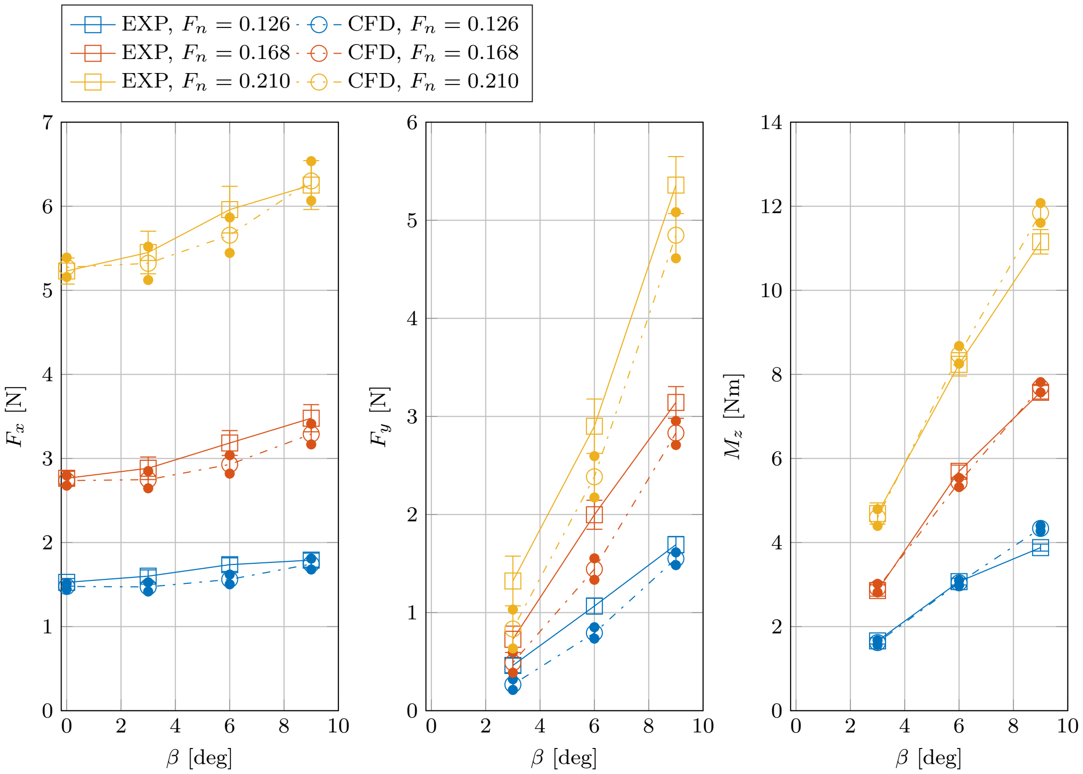

Figure 5-2: Comparison experimental and numerical results, model #16, solid dots depict errorbars for CFD cases

Model #19 Table 5-5 gives the validation results for model #19. The resistance F_x is validated at a U_{val} level of about 5% for both $\beta = 0°$ and 9°. The comparison error for F_y is some 2% larger than the U_{val} value and consequently validation is fails. While for M_z the comparison error is quite low, the U_{val} level is even lower, preventing validation.

When considering the rest of the comparison material in Figure 5-3 and Table 5-6 it is evident that in general model #19 shows lower comparison errors for F_x and F_y. All values for F_x are predicted within 4% and Fy mostly within 10%. Only the comparison errors for M_z are a bit higher than for the other models. The comparison error for yaw moment is relatively high compared to the other models. It shows an overprediction of mostly within 7%.

Table 5-5: Validation of model #19

	$\beta = 0°$	$\beta = 9°$		
	F_x	F_x	F_y	M_z
D	2.068	2.613	2.889	7.123
S	2.058	2.510	2.698	7.314
$E = S - D$ [$\%D$]	-0.49%	-3.94%	-6.63%	2.67%
U_D [$\%D$]	4.84%	4.71%	3.82%	1.11%
U_S [$\%S$]	1.19%	1.17%	1.75%	1.09%
U_{val} [$\%S$]	5.01%	5.04%	4.45%	1.54%
Validated?	✓	✓	✗	✗

Table 5-6: Comparison errors ($E = S - D$ [$\%D$]) of model #19

		$\beta =$			
	F_n	0°	3°	6°	9°
F_x	0.126	-2.44%	-2.22%	-2.23%	-0.78%
	0.168	-0.49%	0.31%	0.84%	-3.94%
	0.210	-0.08%	0.01%	2.71%	3.33%
F_y	0.126		-10.06%	-5.86%	-12.07%
	0.168		-5.60%	-4.03%	-6.63%
	0.210		-4.72%	-2.33%	-8.96%
M_z	0.126		6.50%	8.29%	6.56%
	0.168		6.82%	5.17%	2.67%
	0.210		2.10%	4.43%	4.99%

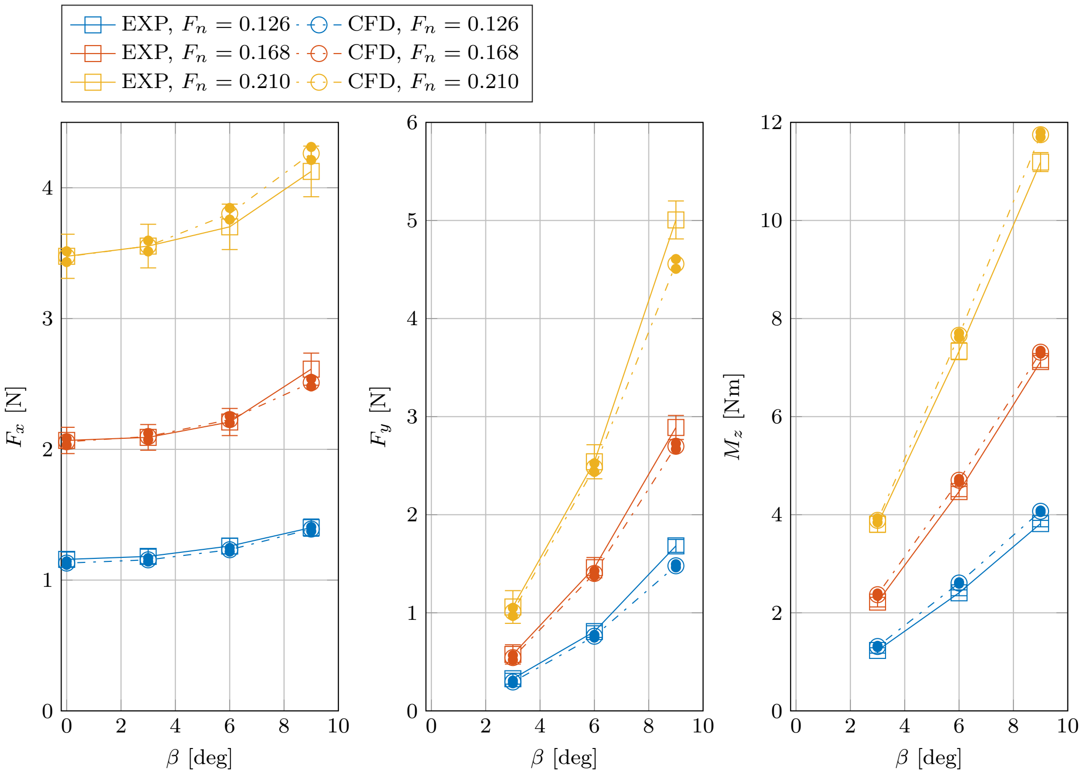

Figure 5-3: Comparison experimental and numerical results, model #19, solid dots depict errorbars for CFD cases

5-3 Qualitative comparison

Next to comparing absolute measured and calculated quantities, one can also make some qualitative comparisons. Because the wave system has a large influence on resistance, side force and yaw moment it is paramount for it to be predicted accurately. However, during the experiments no quantitative measurement was taken of the wave pattern around the hull. What remains is a qualitative comparison from visual observation and photographs taken during the tests.

Figures 5-4 and 5-5 show the bow wave system at the same conditions during the experiment and in the numerical simulation. These figures show a good qualitative agreement between the methods. The main features such as height and position of wave crests and troughs are in agreement.

From the CFD computations, a distinct stern wave with steep crest is observed at models of large C_p. The question arose if this was a numerical defect or a physical phenomenon. Figure 5-6 shows that the same wave system has been observed during experiments.

Although no definite validation, the observations of the wave systems during the experiments and their similarities with the computations are encouraging. Together with the validation data from the previous section, this strengthens the confidence in the numerical method.

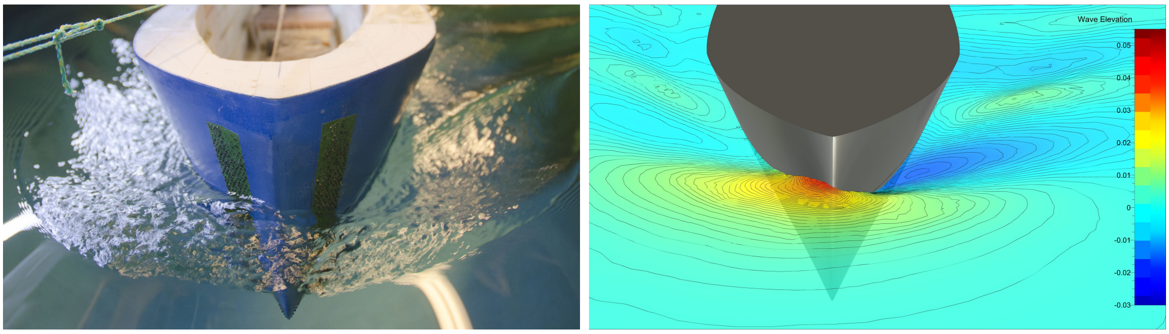

(a) Experiment **(b)** CFD

Figure 5-4: Frontal view of bow wave system, model #1 at $\beta = 9°$ and $F_n = 0.168$

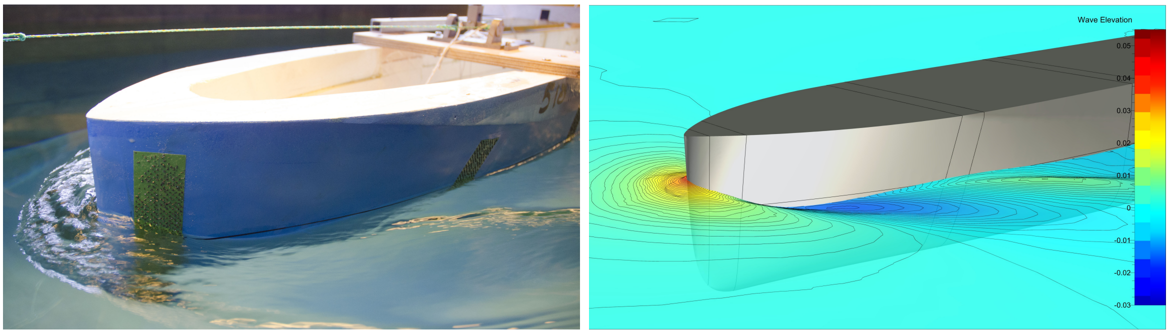

(a) Experiment **(b)** CFD

Figure 5-5: Sideview of bow wave system, model #1 at $\beta = 9°$ and $F_n = 0.168$

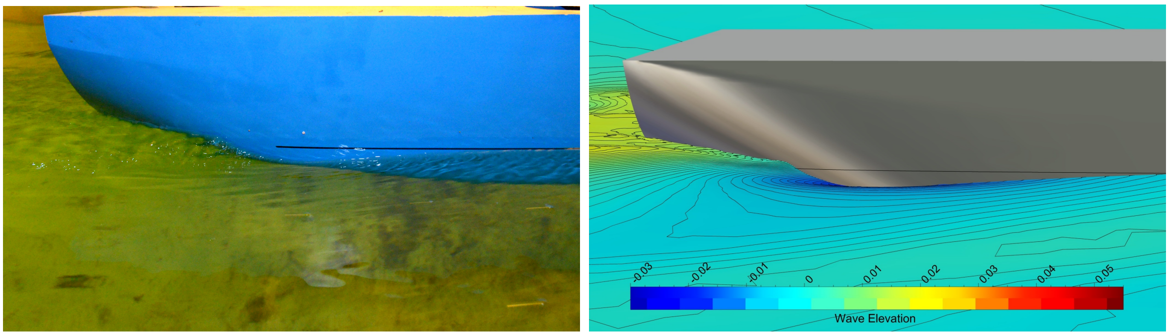

(a) Experiment **(b)** CFD solution of the free surface

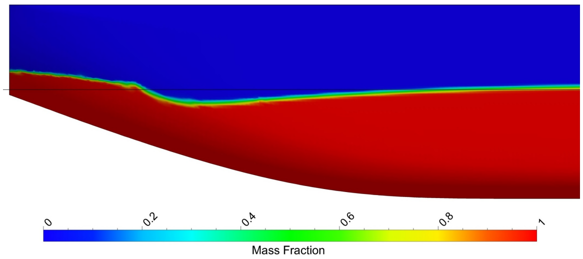

(c) CFD solution of the wetted surface

Figure 5-6: Free surface results at the stern, model #16 at $\beta = 0°$ and $F_n = 0.210$

5-4 Discussion

Observations

- The numerical method almost always underpredicts the resistance F_x and side force F_y.
- F_x is validated for all models at a U_{val} level of around 5%.
- For model #1 F_y is validated. E is only just within U_{val} level with both U_D and U_S contributing.
- In contrast, for models #16 and #19 F_y is not validated. For both models the comparison error E surpasses the already rather large estimate for U_{val} (with both U_D and U_S contributing).
- For all models, the yaw moment M_z is not validated. However, the cause is different. Here the comparison error E is quite small but the estimate for U_{val} is even smaller, preventing a successful validation.
- The solution of the free surface is in qualitative agreement with experiments.

Validation in perspective Although the V&V method leaves the side force for models #16 and #19 and the yaw moments for all models invalidated, there are some notions to be made. For the yaw moment, the estimated uncertainty levels are very low. Even with the quite low comparison errors observed (around 3%), this causes the validation to fail. This while a comparison error of 3% is very acceptable, especially for the foreseen application in a PPP. For the side force, the comparison errors are around $6 - 10\%$ at the V&V conditions. This is quite large and well outside of uncertainty range. The failure of validation is therefore not ascribed to the uncertainty levels. Still, keeping an eye on the application in a PPP, 10% can be acceptable. Especially if the trends are consistent, which they are. In that case, the differences in forces for different models is well predicted and it is expected that an optimisation in a PPP would still yield the correct result.

Leaving the synthetic bare hull condition of the present study and considering the actual application and conditions for a Wind-Assisted Ship Propulsion (WASP) vessel, it is expected that the bare hull forces are not necessarily dominant. A previous CFD study on the parent hull (Mobron, 2014) shows that adding a skeg to the aft ship increases the side force production by 150% compared to bare hull, making it the dominant component in side force generation. It should be noted though that this study has a slightly different approach; the computations are done at full scale and no validation or grid study is performed. Nevertheless it does put the current bare hull results and their validation into perspective with a possible actual sailing configuration. Furthermore, it is expected that when simulating a model with skegs or other appendages the relative uncertainties will decrease.

Possible causes of discrepancies Comparing Figures 5-1, 5-2 and 5-3 and Tables 5-2, 5-4 and 5-6, the comparison errors for the resistance F_x and side force F_y are largest for model #16 ($C_p^+ C_m^+$) while the comparison errors for the yaw moment M_z are largest for model #19 ($C_p^- C_m^-$). This could lead to thinking there is a correlation between the validity of the numerical method and either C_p, C_m or a combination of the two (or some other parameter which varies along with these).

To visualise vortices in the flow, the Q-criterion or second invariant is used:

$$Q = \frac{1}{2}(\|\Omega\|^2 - \|S\|^2) \tag{5-3}$$

where $\|\Omega\| = \text{tr}[\Omega\Omega^t]^{1/2}$ and $\|S\| = \text{tr}[SS^t]^{1/2}$. S and Ω are the symmetric and anti-symmetric components of ∇v. It describes the relative vortical strength given by the difference between the magnitudes of vorticity and local strain rate.

In Figure 5-7 iso-surfaces of $Q = 50$ are constructed and depicted in magenta. The right-hand side of the figures depict the trailing bilge in a cross section at midship. Here the vorticity is visualised by velocity vectors and isolines of the x-component of velocity on the cross section. From these figures the different nature of the vortical structures for these models become evident:

- At model #16, a vortex is shed along the length of the sharp bilges. Supporting this statement are the convergence of streamlines at the trailing bilge, indicating separation (Maskell, 1955). No vortex is shed at the bow.
- At model #19, due to the sharp bow, there exists a vortex shed at the bow travelling downstream. In the cross section this this vortex is also visible. The bow vortex becomes weaker downstream. The streamlines show not convergence along the bilges as at model #16 and no vortex is shed from the bilges.

- At model #1 a weaker bow vortex than at model #19 is shed because of a more blunt bow entry angle.

A hypothesis is that the numerical method does not resolve well the vortical structures around the hull. With nonlinear components such as vortex lift being an important contributor to the side force generation of these models, an ill-resolved vortical structure along the bilges could explain the discrepancies in validation, which are largest for the side force at model #16. The lengthwise development of the bow vortex at model #19 could be a difficult feature to asses, possibly affecting the yaw moment prediction.

Possible improvements Having obtained the validation results, the shortcomings of the numerical simulations are made visible. With the hypothesis that the issues are linked to resolving vortices in the flow, improvements are sought in turbulence modelling. In an attempt to reduce the comparison error the V&V models are simulated with the Explicit Algebraic Stress Model (EASM). Next to that, a 'free' approach is applied, solving trim and sinkage. The impact of these settings on the comparison error with experimental data is shown in Table 5-7. From this one can conclude that the EASM turbulence model captures the hydrodynamic forces more accurately, albeit at the cost of an increase in computation time of about 30%. Solving trim and sinkage does not always lead to a lower comparison error. Furthermore, the convergence time is about twice as large as for a fixed computation.

While the two-equation SST model uses the Boussinesq hypothesis to estimate the Reynolds stress term using eddy viscosity, the EASM model solves all equations for Reynolds stresses (in contrast to Reynolds Stress Modelling (RSM), the equations are solved algebraically). This offers a more complete and physical approach to the problem, including anisotropic eddies. This approach has been reported to outperform the two-equation models in flows with vortical structures (Visonneau et al., 2006), something certainly applicable to the current study. Furthermore, the solver implements a rotation correction (Deng and Visonneau, 1999) when using the EASM model which could influence the performance as well.

Table 5-7: Comparison error ($E = S - D$ [$\%D$]) for different turbulence models on a fixed and free approach at $\beta = 9°$ and $F_n = 0.168$

Trim & sinkage		Fixed		Free	
Turb. model		$k-\omega$ SST	EASM	$k-\omega$ SST	EASM
	F_x	-2%	3%	-1%	5%
Model #1	F_y	-6%	5%	-2%	11%
	M_z	4%	2%	9%	7%
	F_x	-5%	1%	-3%	3%
Model #16	F_y	-10%	3%	-4%	8%
	M_z	2%	0%	8%	6%
	F_x	-4%	-1%	-2%	2%
Model #19	F_y	-7%	-3%	-6%	-1%
	M_z	3%	2%	4%	2%

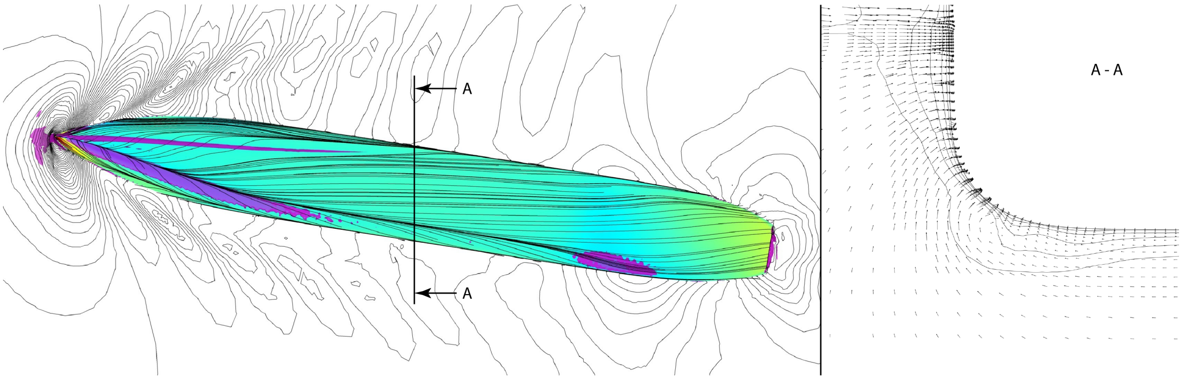

(a) Model #1

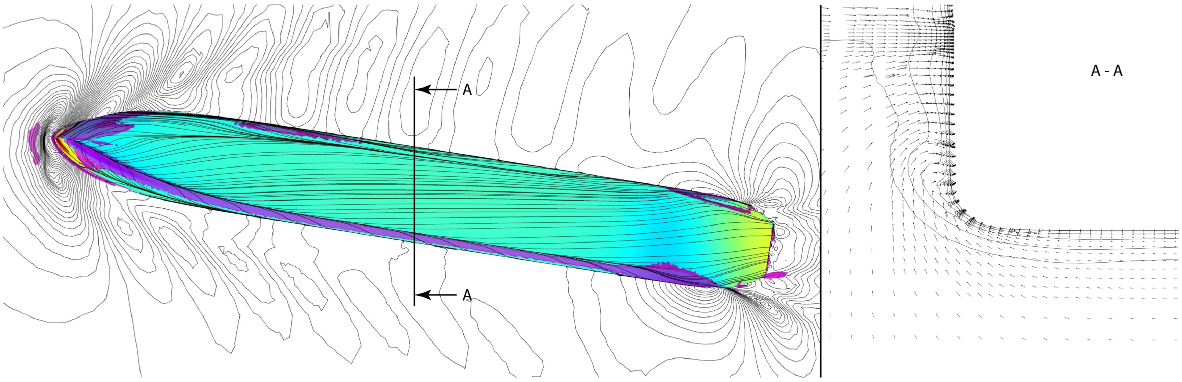

(b) Model #16

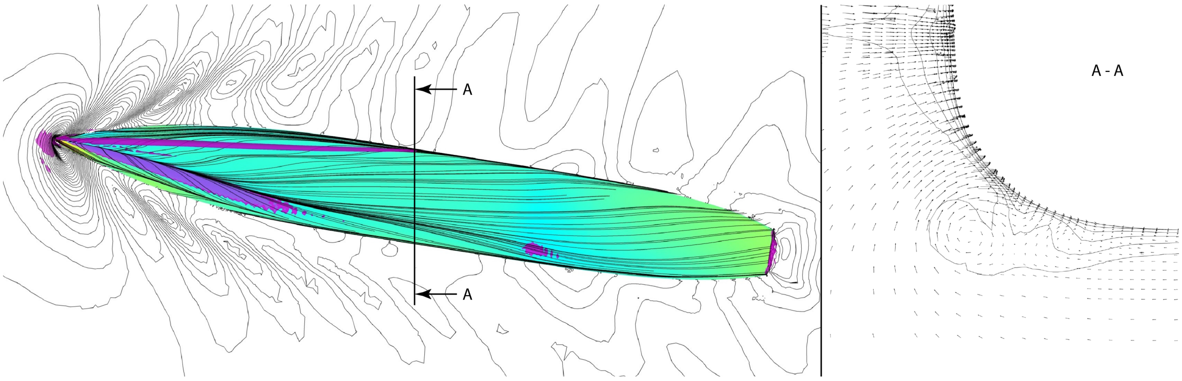

(c) Model #19

Figure 5-7: Numerical results at $\beta = 9^\circ$ and $F_n = 0.168$: wave pattern in isolines of free surface elevation, hydrodynamic pressure in coloured contours on the wetted surface, streamlines on wetted surface and vortices illustrated in magenta by isosurfaces of $Q = 50$, view A - A depicts isolines of the x-component of velocity and velocity vectors in cross section plane at midship

Chapter 6

Regression

To obtain a set of expressions for the hydrodynamic forces to be used in a Performance Prediction Programme (PPP), regression analysis is performed on the dataset obtained by the numerical simulations. In this chapter, the methods, results and evaluation are presented. Throughout this chapter, the statistical terms ‘dependent variable’ and ‘independent variable’ are used to describe the hydrodynamic forces and the hull form parameters respectively. The analysis is done for $F_n = 0.168$ because this is the most complete dataset, covering all drift angles.

6-1 Force decomposition and scaling

Before proceeding to regression analysis, the results are in need of some editing. The quality of the regression can be enhanced by proper decomposition and scaling. Decomposition allows to split a result into several parts to separate physical effects. Scaling allows to make the results non dimensional. With scaling one is also able to remove the largest known physical relation with an independent variable. This allows for a more easy identification of the subtle effects.

Decomposition The decomposition applied here is a common one in naval architecture: dividing the resistance into two components. However, there are still different options on how to make the decomposition.

- In a viscous numerical simulation like the one in the present work, the pressure and frictional resistance components can be obtained directly by integrating normal and tangential force components over the vessel’s wetted surface area respectively. It is therefore possible to perform regression on these two forces separately.
- Following towing tank practice, the frictional resistance F_{xF} is estimated using the ITTC-57 correlation line. This estimate is then subtracted from the total resistance F_x to obtain a residuary resistance F_{xR}.

While the correlation line is only an estimate, using the decomposition with frictional and residuary resistance does allow for scaling the results according to Froude's scaling law, offering flexibility in the application of a PPP. Because of this convenience, this decomposition has been chosen for the current regression analysis.

Recalling the main question's focus on the hydrodynamic forces leaves the following dependent variables for regression:

- side force F_y
- yaw moment M_z
- residuary resistance F_{xR}

Scaling The side force production is strongly related to the draft of the vessel and the projected surface area. The choice for division by the product $L \cdot T$ is made. It corresponds to the widely used non dimensional formulation in ship manoeuvring, albeit in a different axis system (in this case with y perpendicular to the flow rather than the vessel's centreline, see Figure 3-1). Furthermore, it allows C_y to be interpreted as the lift coefficient used in aerodynamics. With $q = {}^1\!/_2 \rho V_m^2$ the dynamic pressure the coefficient is defined as:

$$C_y = \frac{F_y}{qLT} \tag{6-1}$$

The yaw moment is made dimensionless analogous to the side force, but with an extra L to account for the extra dimension:

$$C_n = \frac{M_z}{qL^2T} \tag{6-2}$$

For the resistance, first the residuary component is obtained by subtracting the estimated friction resistance:

$$F_{xR} = F_x - F_{xF} \tag{6-3}$$

where $F_{xF} = qS_wC_{f,ITTC}$, with S_w the wetted surface and $C_{f,ITTC}$ the ITTC-57 correlation coefficient defined as (ITTC, 2005):

$$C_{f,ITTC} = \frac{0.075}{(\log_{10}(Re) - 2)^2} \tag{6-4}$$

Consisting mostly of wave-making resistance, the residuary resistance is heavily related to the displacement volume ∇ of a vessel. As in the Delft Systematic Yacht Hull Series (DSYHS), division by the vessel's weight $\rho g \nabla$ is used to make the residuary resistance dimensionless:

$$C_{xR} = \frac{F_{xR}}{\rho g \nabla} \tag{6-5}$$

6-2 Method

With the goal of deriving polynomial expressions for the hydrodynamic forces and moments as function of the form parameters varied in the series, multiple linear regression is applied. The data is fitted in the least-squares sense. The expressions all have the characteristic form:

$$Y = a_0 + a_1 P_1 + \cdots + a_n P_n \tag{6-6}$$

with Y being the dependent variable (in this case a hydrodynamic force coefficient), P_i the independent variables (in this case the hull form parameters) and a_i the coefficients obtained from least-squares fitting.

These coefficients are commonly determined per Froude number F_n. This avoids having to model the humps and hollows of the speed-resistance curve. In the current work only one F_n is considered. Nevertheless, this methodology is adopted for the sake of convenience and consistency with other regression formulae.

6-2-1 Selection of independent variables

The independent variables can be hull form parameters or the orientation of the vessel (only the drift angle β is considered since heel, trim and sinkage are neglected). From the main form parameters many derived combinations or higher order versions can be constructed. Above all, they are always made non dimensional, as the dependent variables are as well. The following hydrostatic parameters are considered for use as independent variable in the regression:

Global hydrostatic parameters & ratios of dimensions

- C_p, prismatic coefficient
- C_b, block coefficient
- C_m, midship section area coefficient
- C_{hl}, lateral area coefficient
- C_{wp}, waterplane area coefficient
- $\frac{LCB}{L}$, longitudinal centre of buoyancy, made non dimensional with L, taken from ⊗
- $\frac{VCB}{T}$, vertical centre of buoyancy, made non dimensional with T, taken from DWL
- $\frac{L_{hl}}{L}$, longitudinal centre of lateral area, made non dimensional with L, taken from ⊗
- $\frac{B}{T}$, breadth to draft ratio
- $\frac{T}{L}$, geometric aspect ratio
- $\frac{L}{B}$, length to breadth ratio
- $\frac{L}{\nabla^{1/3}}$, slenderness ratio
- $\frac{S_w}{\nabla^{2/3}}$, wetted surface to displacement ratio
- $\frac{L}{S_w^{1/2}}$, length to wetted surface ratio
- $\frac{A_{hl}}{A_{wp}}$, lateral area to wetted surface ratio
- $\frac{A_{wp}}{S_w}$, waterplane area to wetted surface ratio

Local form parameters (see Figure 6-1)

- I_e, incidence angle of DWL entrance
- E_r, exit rocker angle

- $\frac{R_b}{\sqrt{(\frac{1}{2}B)^2+T^2}}$, bilge radius, made non dimensional with cross section dimensions
- $\frac{L_{PMB}}{L}$, length of PMB, made non dimensional with L

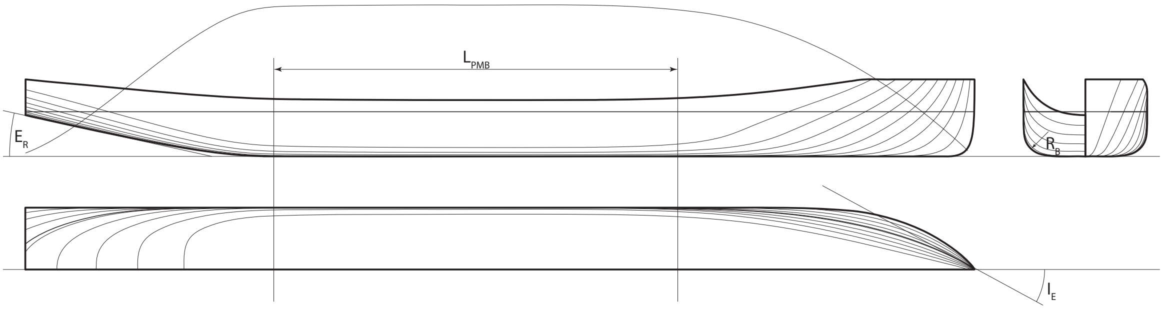

Figure 6-1: Definition of local form parameters

The independent variables are tested for significance with the dependent variable. From this, the highest ranking independent variables are chosen for a further trial-and-error process. Different combinations, products and powers are tried for a better fit of the data. During this process the aim is also to keep both the amount of variables and the power of the used variables as low as possible for a reasonable fit. This enhances the stability and robustness of the formulations because higher powers tend to behave unstable when extrapolating outside the range of the original series. Thus, if e.g. C_p describes the data equally as good as C_p^2, the former is chosen.

Also of importance is to use variables in the formulation which are not strongly correlated to each other. This can be determined using the Pearson's correlation coefficient r, defined as:

$$r = \frac{COV(X,Y)}{\sigma(X)\sigma(Y)} \tag{6-7}$$

in which the covariance between two variables is defined as $COV(X,Y) = E[(X - E[X])(Y - E(Y)]$. It is advised (Huetz, 2012) to keep this value below 0.85 to ensure stability of the formulation.

6-3 Result

6-3-1 Side force

As is known from wing theory, the aspect ratio $\text{\AE}$ has a pronounced effect on the lift production ($C_L \propto \text{\AE}$). In the case of a ship, this translates to $\text{\AE} = {}^{T}\!/_{L}$. A main characteristic of a ship hull is its low aspect ratio. With T an order of magnitude smaller than L one ends up with $\text{\AE} \ll 1$. Following low-aspect ratio wing theory (Hoerner, 1985) the generated lift can be split up into two components: a linear and nonlinear contribution. The linear contribution stems from circulation lift, the nonlinear component from so-called cross-flow drag. As an illustration, two extreme cases are considered:

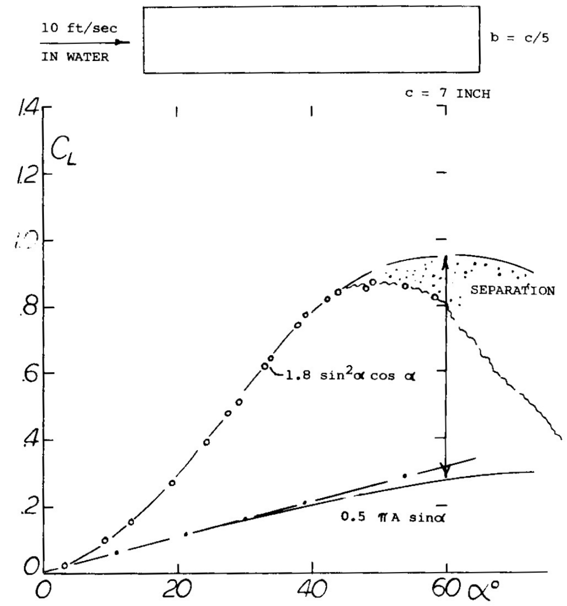

Figure 6-2: Lift characteristics of a flat plate of $\text{Æ} = 0.2$ at incidence angle α (from: Hoerner, 1985)

- A very high-aspect wing with $\text{Æ} \rightarrow \infty$ has no tips. Consequently, there cannot exist any cross-flow from the pressure to the suction side. All lift is therefore due to the circulation on the airfoil.
- A wing with $\text{Æ} \rightarrow 0$ (an infinitely long strip) has no leading or trailing edge. Therefore, there cannot be any circulation. However, lift is still produced by transfer of momentum normal to the wing, by cross-flow along its lateral edges. This manifests itself by vortex sheets curling around the lateral edges. It is therefore also associated with 'vortex lift'.

See Figure 6-2 for an illustration of both contributions on a flat plate of $\text{Æ} = 0.2$.

These two components can be estimated separately. The linear component can be estimated by e.g. Jones' formula for low-aspect ratio wings (Jones, 1946):

$$C_L = \frac{\pi}{2}\text{Æ}\sin\beta \tag{6-8}$$

$^{T}/_{L}$ $\rightarrow$ It is indeed found that $^{T}/_{L}$ in combination with β has a significant correlation to the side force coefficient C_y.

The nonlinear component of lift ΔL, dubbed cross-flow drag is treated as the drag component from the force N normal to the wing, varying with the square of the cross-flow velocity component:

$$\Delta L = N\cos\beta = C_D\frac{1}{2}\rho(V\sin\beta)^2\cos\beta \tag{6-9}$$

From this, the lift coefficient ΔC_L becomes:

$$\Delta C_L = C_D\sin^2\beta\cos\beta \tag{6-10}$$

So while for high-aspect wings the lift coefficient is linearly proportional to β, at lower aspect ratios it is found that lift production has a nonlinear component varying with β^2. The following terms are found to best be combined with β^2:

$\mathbf{C_m} \rightarrow$ From wing design the shape of the wing tip is found to be of influence on lift production as well. Rounded tips generate less lift. This can be expressed as a reduction of effective span or aspect ratio (Hoerner, 1985). Also, a larger C_m can induce stronger bilge vortices by its sharper bilges, thereby creating nonlinear vortex lift. Experiments on ship models with different bilge radii are in accordance with this. For example, the sharp-bilged hull blocks in the wind-tunnel study of Bradbury (1985) show distinct vortices originating from these bilges, increasing both side force and resistance compared to rounded bilges. Experiments on a wing section towed with square and rounded bilges offer the same observations (Beukelman, 1993). Furthermore, C_m shows good correlation to the data set. It is therefore included in the formula.

$\mathbf{C_p} \rightarrow$ It is expected that C_p also has an influence on the generation of side force. A low C_p makes for a fine bow entry angle, which at a drift angle could generate a vortex. See Figure 6-3 for an example of a bow vortex at a model of low C_p. Vortex-induced lift is then expected to contribute to the side force.

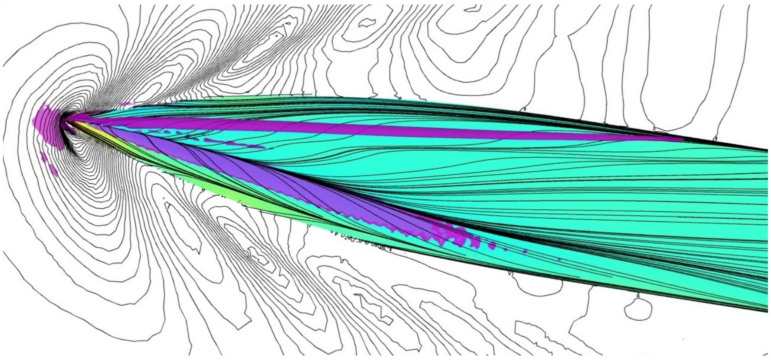

Figure 6-3: Bow vortex, model #19 ($C_p^- C_m^-$) at $\beta = 9°$ and $F_n = 0.168$, wave pattern in isolines of free surface height, hydrodynamic pressure in coloured contours on the wetted surface, streamlines on wetted surface and vortices illustrated in magenta by isosurfaces of $Q = 50$

$\mathbf{{}^{A_{wp}}/_{S_w}} \rightarrow$ Testing the influence of different variables, ${}^{A_{wp}}/_{S_w}$ was found to significantly increase the fit of the regression. This ratio between waterplane area and wetted surface can be interpreted as an effective span of some sort. When ${}^{A_{wp}}/_{S_w} = 1$ the draught (span) is zero. Assuming a constant waterplane area A_{wp}, an increase in draft T increases the aspect ratio ${}^{T}/_{L}$ and the span while an increase in C_p increases the projected area A_{hl} in the stern region, something ${}^{T}/_{L}$ cannot describe. A lower C_m has a similar effect as rounded wingtips in wing theory, decreasing effective span. While all these effects can be described by different variables separately, the ratio ${}^{A_{wp}}/_{S_w}$ describes the change in 'effective area' by the effect of multiple parameters. It is perhaps because of this that its effect in regression is so powerful. Unfortunately it does show a relatively hight correlation to ${}^{T}/_{L}$, see Table 6-1. This could be a risk for the stability of the formulation.

The formulation now reads:

$$C_y = \beta a_1 \frac{T}{L} + \beta^2 \left[a_2 C_p + a_3 C_m + a_4 \frac{A_{wp}}{S_w} \right] \tag{6-11}$$

with β in radians. The resulting fit of this is displayed in Figure 6-4. The relative error in the prediction (the residual as percentage of the observed value) is mostly within 20% for $\beta = 9^\circ$, which is still significant. Unfortunately, no means of improving this has been found without compromising the simplicity or stability of the formulation. Table 6-2 depicts the coefficients a_i of the formulation. To gain some insight into the relative contribution of each term, the total term (coefficient × variable) is represented as a percentage of the whole expression. For this, hydrostatic values for the parent hull are chosen for input as a representative mean case. It can be observed that the term containing C_m contributes most. After that, the ratios A_{wp}/S_w, T/L, and C_p follow.

Table 6-1: Correlation coefficients for variables used in C_y

	T/L	C_p	C_m	A_{wp}/S_w
T/L	1.00	0.01	0.00	-0.89
C_p	0.01	1.00	0.03	-0.17
C_m	0.00	0.03	1.00	-0.41
A_{wp}/S_w	-0.89	-0.17	-0.41	1.00

Table 6-2: Regression coefficients and contribution per term for C_y

F_n	a_0	a_1	a_2	a_3
0.168	1.144	-0.2519	1.358	-1.081
Term	$\beta a_1 T/L$	$\beta^2 a_2 C_p$	$\beta^2 a_3 C_m$	$\beta^2 a_4 A_{wp}/S_w$
Relative contribution	14%	-8%	50%	-28%

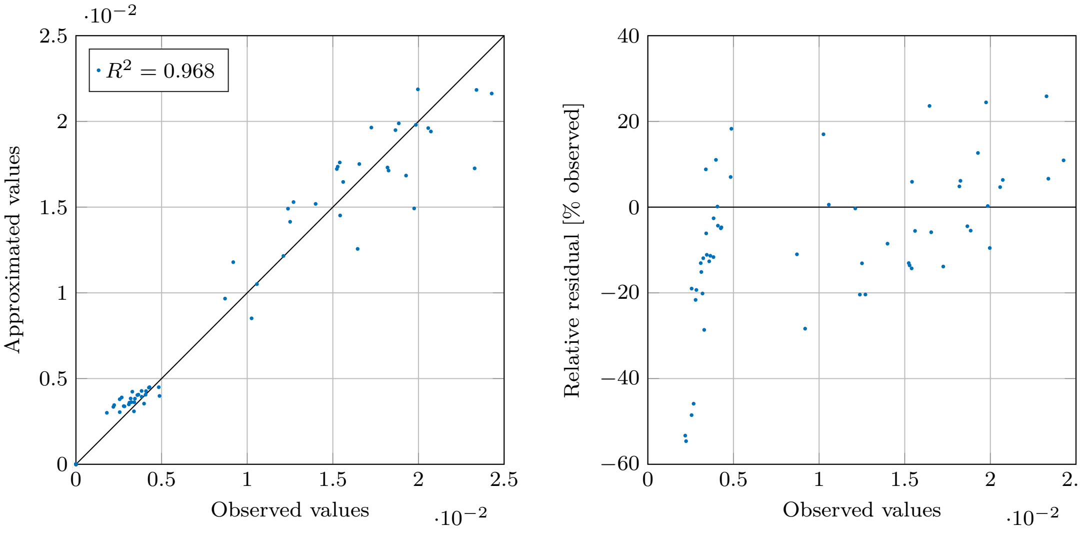

Figure 6-4: Fit of the C_y formulation

6-3-2 Yaw moment

As is observed in many WASP and manoeuvring studies, a ship at a drift angle tends to generate a destabilising yaw moment if not compensated by rudder action or other appendages. This destabilising moment is described as the *Munk moment* (Munk, 1924). Its mechanism can be explained as follows:

> In an inviscid flow, a blunt body under incidence angle will develop zero side force (*d'Alembert's paradox*), but a nonzero moment because of the asymmetry of the stagnation points. Consider the situation in Figure 6-5a. In the inviscid case, the flow is decelerated at the stagnation point at the inflow side of the bow and accelerated moving around the other side side of the bow. This induces a local lift force. At the stern, the exact opposite occurs. The two lift forces thus cancel out as total lift, but create a destabilising moment. This so-called *Munk moment* tends to increase the incidence angle even further.
>
> In the viscous case, the flow at the aft ship can be separated as illustrated with the grey area in Figure 6-5b. In that case the side force at the stern is lower and the yaw moment reduces. As a simplification, some methods approximate this viscous moment by integrating only over the forward half of the ship, or up to where the draft is maximum (e.g. Nomoto and Tatano, 1979).

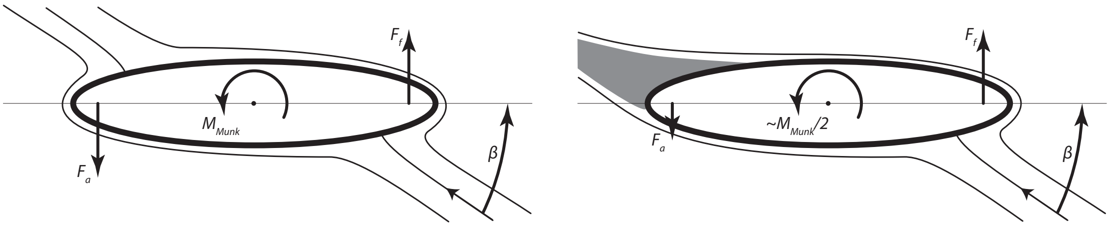

(a) Inviscid flow **(b)** Viscous flow, separation illustrated in grey

Figure 6-5: Streamlines around a blunt body (from: Kornev, 2011)

Figure 6-6a offers more detail on the lengthwise distribution of side force obtained from segmented model tests (Beukelman, 1989). The numerical results show a similar distribution, see Figure 6-6b. The bow sections are dominant in side force generation while the midship sections are little effective. The aft ship has a negative contribution, albeit smaller than the bow. From this it is expected that the distribution of volume near bow and stern is of influence. C_p is therefore included in the formulation for C_n.

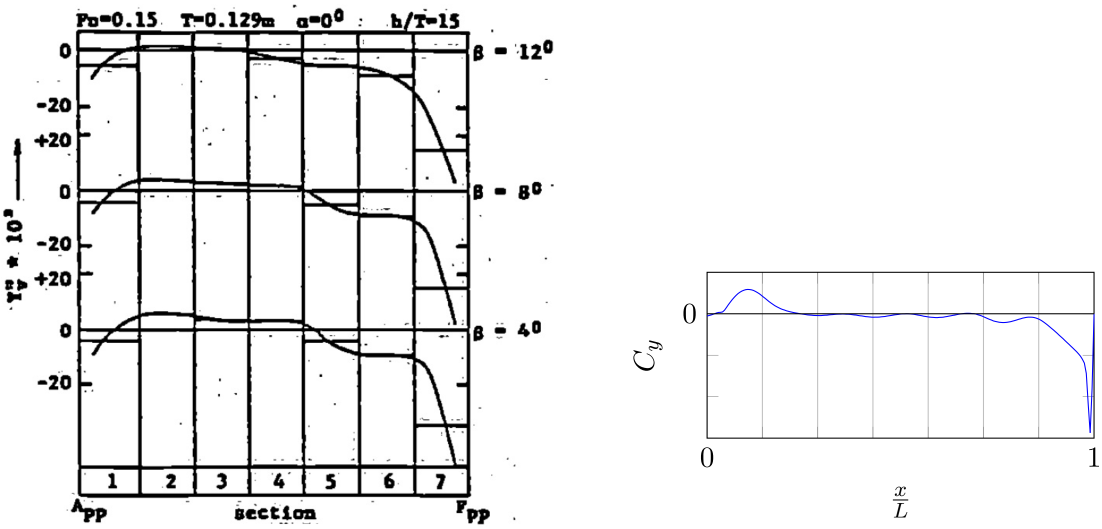

(a) Experimental results of a Series 60 model at $F_n = 0.15$ (from: Beukelman, 1989)

(b) Numerical result of model #16 at $\beta = 9°$ and $F_n = 0.168$

Figure 6-6: Lengthwise side force distribution

Looking at manoeuvring coefficients for the yaw moment, T/L is used to describe the linear coefficient N'_β. This is also shown to correlate to the current dataset and is thus included in the formulation.

The nonlinear contribution $N'_{\beta\beta}$ is often very small or neglected. Towing tank observations on Wind-Assisted Ship Propulsion (WASP) vessels also show an almost linear relation to β. The formula is therefore only multiplied by the linear term β.

Testing other variables, C_m helps describing the data while keeping the formulation simple and the variables uncorrelated (see Table 6-3). This might be only due to the construction of the series though (varying T, C_p and C_m).

Including a constant in the formula did not bring instability to the formulation as it did for C_y. However, it also did not benefit the quality. A form without constant is therefore adopted for C_n. The formula reads:

$$C_n = \beta \left[b_1 \frac{T}{L} + b_2 C_p + b_3 C_m \right] \tag{6-12}$$

with β in radians and the coefficients b_i depicted in Table 6-4 together with the term's relative contribution. T/L has the highest contribution while C_p has only a minor one. The relative error in the prediction is mostly within 10%, as can be read from Figure 6-7.

Table 6-3: Correlation coefficients for variables used in C_n

	${}^{T}\!/\!_{L}$	C_p	C_m
${}^{T}\!/\!_{L}$	1.00	0.01	0.00
C_p	0.01	1.00	0.03
C_m	0.00	0.03	1.00

Table 6-4: Regression coefficients and contribution per term for C_n

F_n	b_1	b_2	b_3
0.168	1.732	-0.005434	0.05055
Term	$\beta b_1 {}^{T}\!/\!_{L}$	$\beta b_2 C_p$	$\beta b_3 C_m$
Relative contribution	61%	-3%	36%

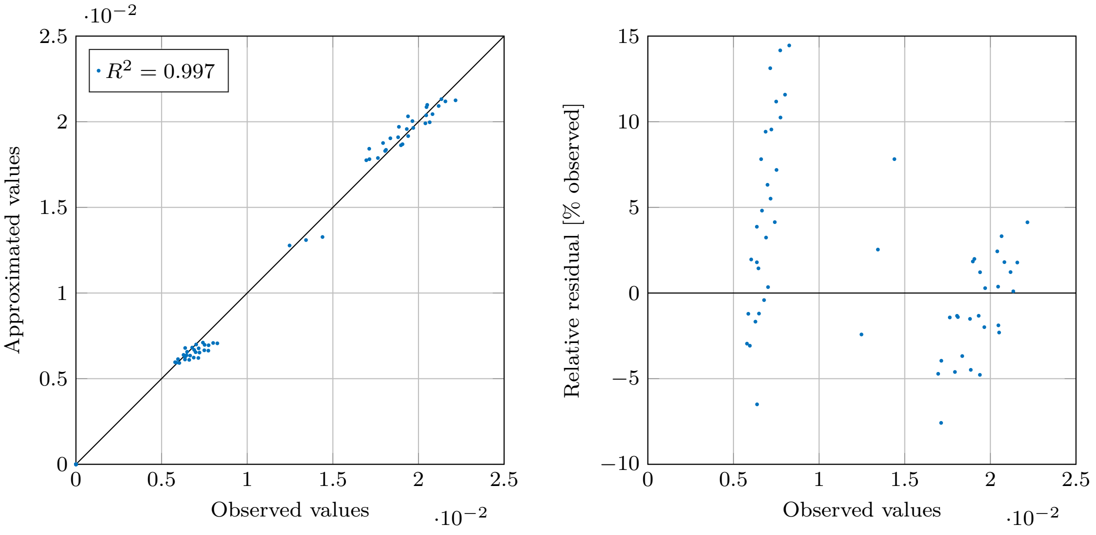

Figure 6-7: Fit of the C_n formulation

6-3-3 Residuary resistance

For residuary resistance, the volume and its distribution is known to be of primary influence. In making the quantity dimensionless, it is already divided by the vessel's weight $\rho g \nabla$. Remaining variables related to volume that are found to improve the fit are included in the formulation: C_p and C_m. Some other volumetric variables expected to be of influence like $L/\nabla^{1/3}$, LCB/L or VCB/T yield no improved fit and are therefore not included. See Table 6-6 for the correlation of the variables.

Next to predicting the residuary resistance at zero drift, also the induced resistance from side force at drift is estimated in this formula. From airfoil theory the induced drag is known to be proportional to the lift squared and aspect ratio: $C_{Di} \propto \frac{C_L^2}{A}$. For a ship this translates to $\frac{C_y^2}{T/L}$. However, using just C_y^2 yields a much better result and is thus chosen for inclusion. The formula reads:

$$C_{xR} = c_0 + c_1 C_p + c_2 C_m + c_3 C_y^2 \tag{6-13}$$

with the coefficients c_i depicted in Table 6-5. For presenting the contribution of the C_y^2 term, a representative value for C_y has been chosen from model #1 at $\beta = 9°$ and $F_n = 0.168$. The contributions are quite evenly divided amongst the different terms.

Figure 6-8 depicts the fit of the formulation. This shows quite some scatter with the relative error mostly within 20% of the observed value from CFD. Unfortunately, no means of improving this was found without adding variables or combination of variables that are very correlated to one another. However, to put this into perspective, the residuary resistance within this series for this Froude number is typically only $15 - 30\%$ of the total resistance. The error is therefore only about $3 - 6\%$ of the total resistance.

Table 6-5: Regression coefficients and contribution per term for C_{xR}

F_n	$c_0 \times 10^4$	$c_1 \times 10^4$	$c_2 \times 10^4$	c_3
0.168	4.870	9.445	-8.260	1.544
Term	c_0	$c_1 C_p$	$C_2 C_m$	$c_3 C_y^2$
Relative contribution	20%	29%	-32%	19%

Table 6-6: Correlation coefficients for variables used in C_{xR}

	C_p	C_m
C_p	1.00	0.03
C_m	0.03	1.00

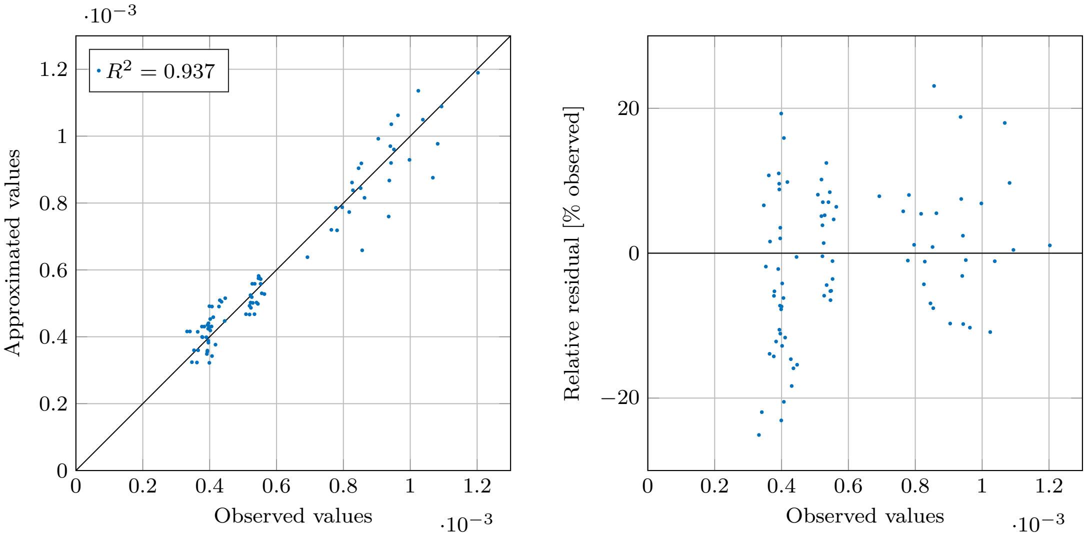

Figure 6-8: Fit of the C_{xR} formulation

6-4 Evaluation

To illustrate the effectiveness of the regression formulae, examples of the fit with models from within the Delft Systematic Wind-Assisted Series (DSWAS) are given. Thereafter, the formulations are tested on models not belonging to the series.

6-4-1 Verification within series

Figures 6-9, 6-10 and 6-11 give the fit to the Verification and Validation (V&V) models #1, #16 and #19 respectively. Here one can see that the fit for #1 and #16 is very good. Most models in the series show a similar satisfactory fit.

The fit on #19 is among the lowest throughout the series. The most poor fit is found for model #27, displayed in Figure 6-12. Here the resistance F_x and side force F_y at $\beta = 9°$ are underestimated by 6% and 24% respectively. This is in line with the residuals as found in sections 6-3-1 and 6-3-3.

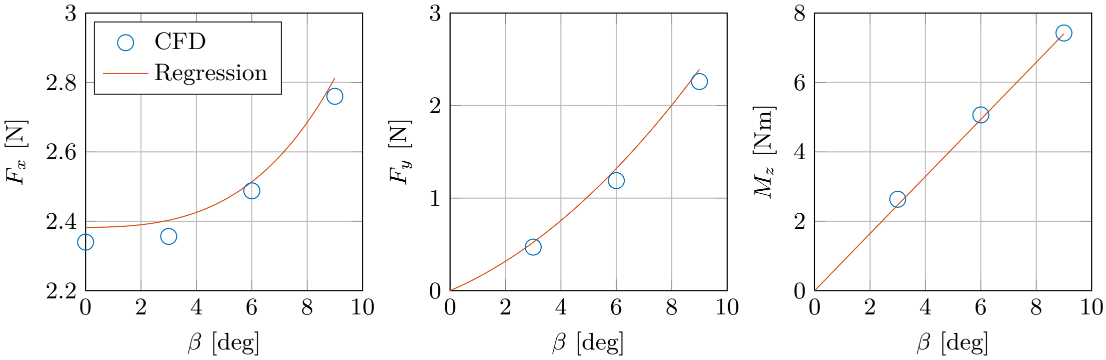

Figure 6-9: Fit of the regression on model #1

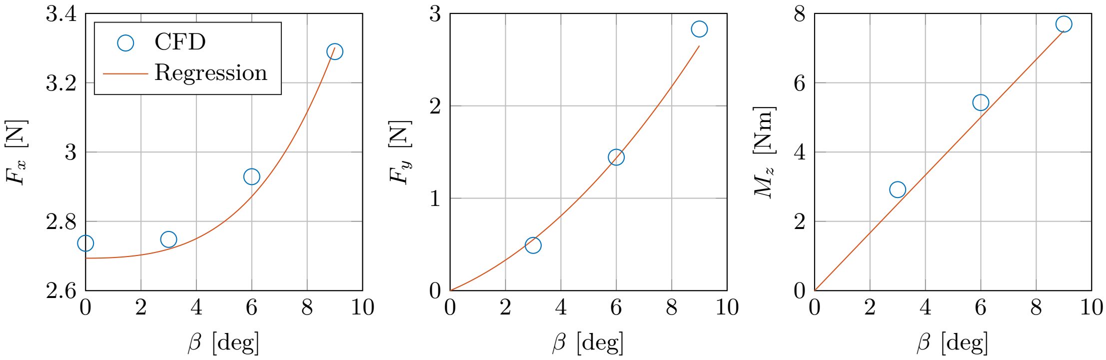

Figure 6-10: Fit of the regression on model #16

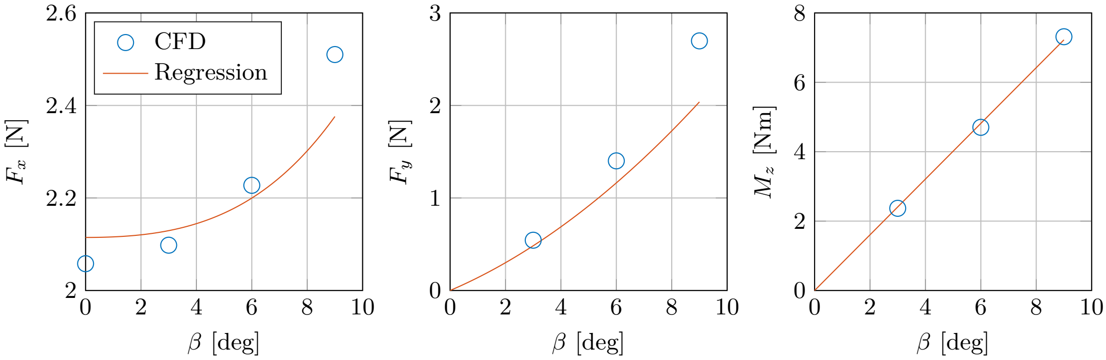

Figure 6-11: Fit of the regression on model #19

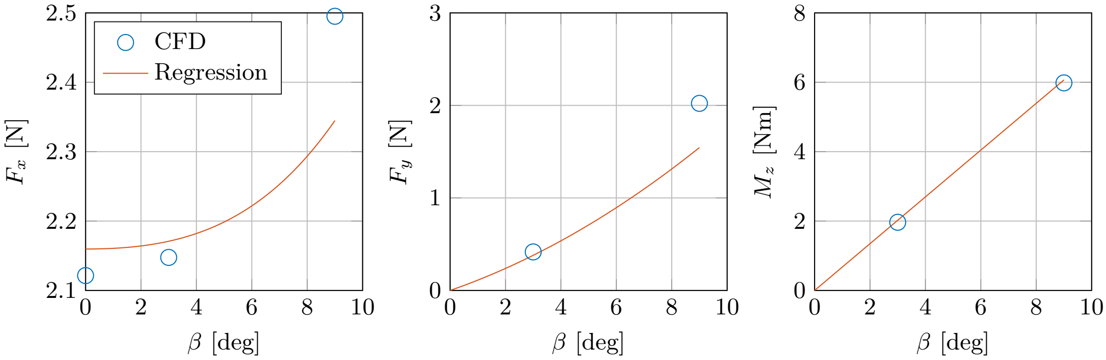

Figure 6-12: Fit of the regression on model #27

6-4-2 Comparison outside series

To test the obtained formulations, a comparison is made with models outside the series. In order for the formulations to remain stable, it is best to select models with their parameters for input within the range of the DSWAS. Next to that, for best performance of the formulations, the overall hull shape and design philosophy should be in line with that of the models in the DSWAS. It is evident that these conditions cannot always be met for other ship models. The deviations then give some valuable insight into the shortcomings of the present formulations.

The parameters used for input in the formulation for the selected evaluation models are depicted in Table 6-7. Parameters outside of range of the DSWAS are highlighted in red. An overview of their linesplans is given in Figure 6-13.

Unfortunately, for most models, no test data is available for resistance at drift angles. For these models only the formulations for side force and yaw moment are evaluated.

Table 6-7: Input parameters of models used to evaluate the formulations, values outside of range of the DSWAS highlighted in red

	DSWAS		*Victory*	*Series 60*	*Mariner*	*840 Series*	*840 Series*
	min	max		$C_b = 0.70$		*Model 842*	*Model 846*
F_n	0.168		0.173	0.150	0.195	0.198	0.198
T/L	0.042	0.052	0.066	0.056	0.049	0.050	0.031
C_p	0.686	0.840	0.751	0.710	0.620	0.540	0.540
C_m	0.874	0.984	0.989	0.986	0.965	0.943	0.943
A_{wp}/S_w	0.578	0.752	0.522	0.575	0.623	0.651	0.774

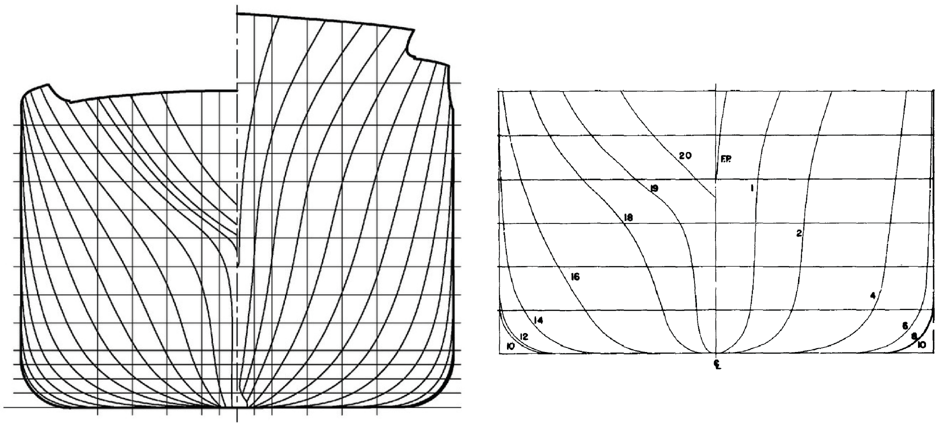

(a) *Victory* **(b)** *Series 60*, $C_b = 0.70$

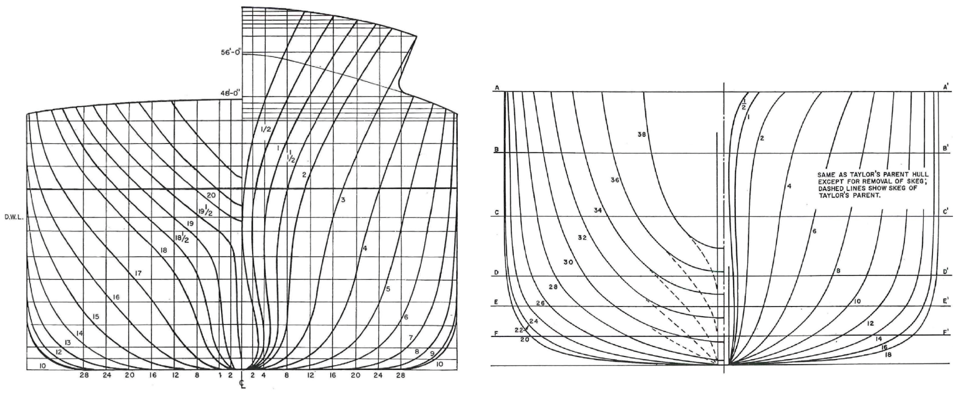

(c) *Mariner* **(d)** Parent of *840 Series*

Figure 6-13: Linesplans of models used for evaluation of the regression formulae

Victory ship Figure 6-14 depicts the result of using the hydrostatic parameters of a *Victory* ship as input for the formulations. Experimental results by De Jong et al. (2012) are plotted for comparison. These tests are performed at $F_n = 0.173$ and include a rudder fixed amidship (thereby deviating from the bare hull conditions of the DSWAS).

Here one can notice that the side force is underpredicted by about 50%, about the same effect as adding a rudder to the bare hull parent (Mobron, 2014). The yaw moment is reasonably close to the prediction by the formulation. The resistance at $\beta = 0°$ is overpredicted by 21% while the resistance at $\beta = 10°$ might be coincidentally well predicted.

It must be noted that the hull shape is fundamentally different from the ones in the DSWAS; the *Victory* does not feature a pram-type aft shape, but more V-shaped sections. See Figure 6-13a for her linesplan.

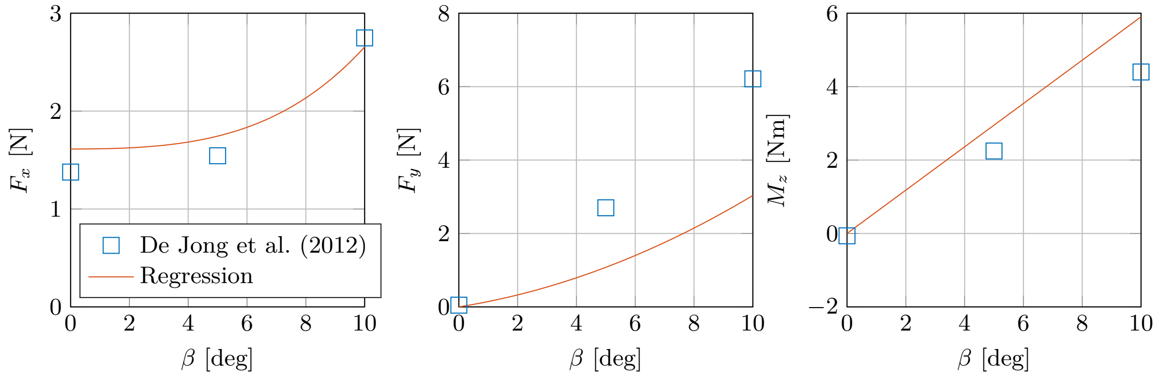

Figure 6-14: Fit of the regression results with experimental results of a *Victory* ship

Series 60 The regression formulae are tested for a model from the well-known *Series 60*. This hull form is similar to the *Victory*, both in parameters as in design (section shape and profile). Figure 6-15 depicts the fit of the formulations to the experimental data by Jacobs (1966). The performance of the formulation is comparable to that of the *Victory*, with F_y underpredicted and M_z a bit overpredicted.

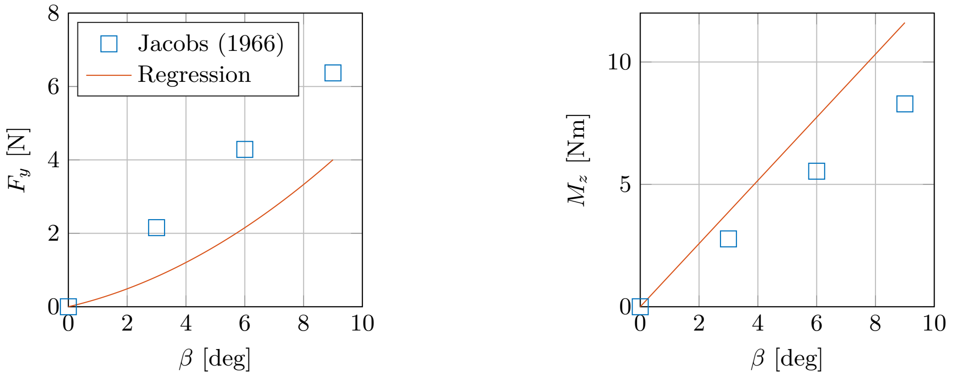

Figure 6-15: Fit of the regression results with experimental results for model of $C_b = 0.70$ from the *Series 60*

Mariner The *Mariner* type vessel is tested at many facilities around the world and serves as a benchmark. Experimental results by Glansdorp (1973) as well as Jacobs (1966) are plotted with the present formulation in Figure 6-16. It must be noted that the used model scale differs, with resulting model lengths of $L_m = 2.29\,\mathrm{m}$ and $1.52\,\mathrm{m}$ respectively. Nevertheless, the results from both experimental programmes are in reasonable agreement, an indication of a low influence of scale effects. The test conditions are equal for both experimental programmes, with a trim by the stern of $0.43°$. The results from Glansdorp (1973) for positive and negative static drift angles are grouped together, revealing experimental scatter.

As with the *Series 60* model, the side force is under-predicted and the yaw moment over-predicted. This can both be ascribed to the fundamentally different aft shape of the models. The V-shaped, deadwood-like aft stations are bound to generate a higher side force and reduce

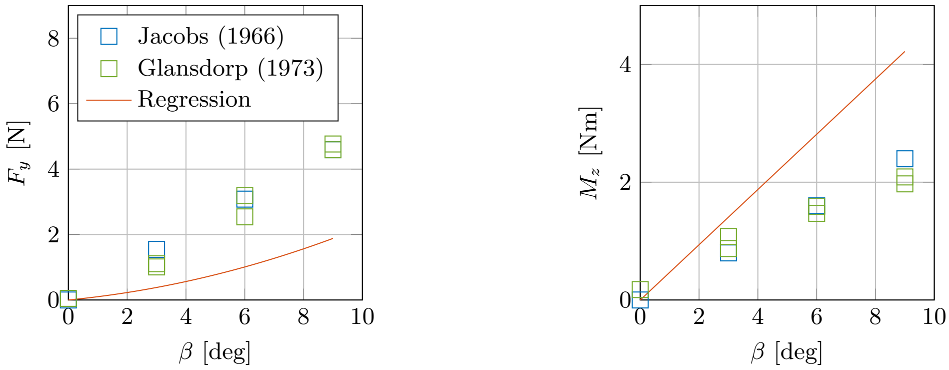

Figure 6-16: Fit of the regression results with experimental results for the *Mariner* model

the yaw moment. Also the trim by the stern is not accounted for in the formulations and can further increase side force and decrease the yaw moment.

840 Series The study by Jacobs (1966) on the effect of skegs on manoeuvring characteristics also offers bare hull data of models from the *840 Series*. With a pram-type aft ship, these models are more in line with the design philosophy of the DSWAS, making for useful comparison material. The main difference is the prismatic coefficient which is well outside of range, see Table 6-7.

Considering model 842 in Figure 6-17, it can be seen that the yaw moment is predicted very accurately. The side force shows more deviation. One can notice that the coefficients from Jacobs (1966) are only linear with β, while the present formulation for side force has a nonlinear term.

Using model 846 from the *840 Series*, the regression can be tested with a similar hull shape but with more parameters outside the range of DSWAS, see Figure 6-18. The fit is a little less good than for model 842 but in general the decrease in side force and yaw moment is captured quite adequately, demonstrating the stability of the formulations.

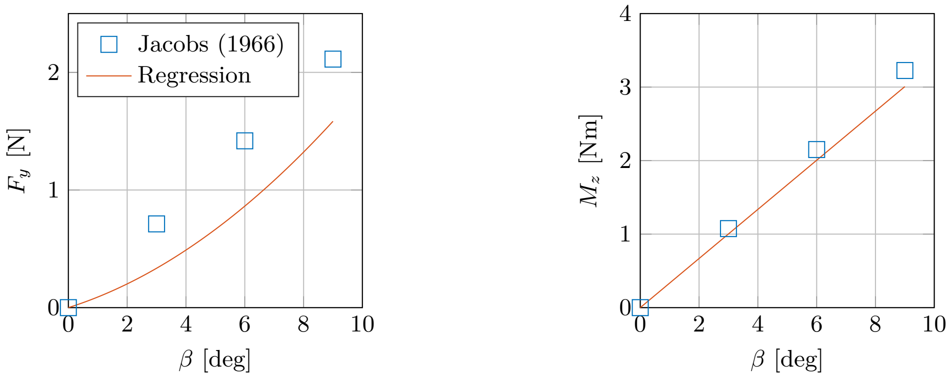

Figure 6-17: Fit of the regression results with experimental results for model 842 from the *840 Series* with removed skeg

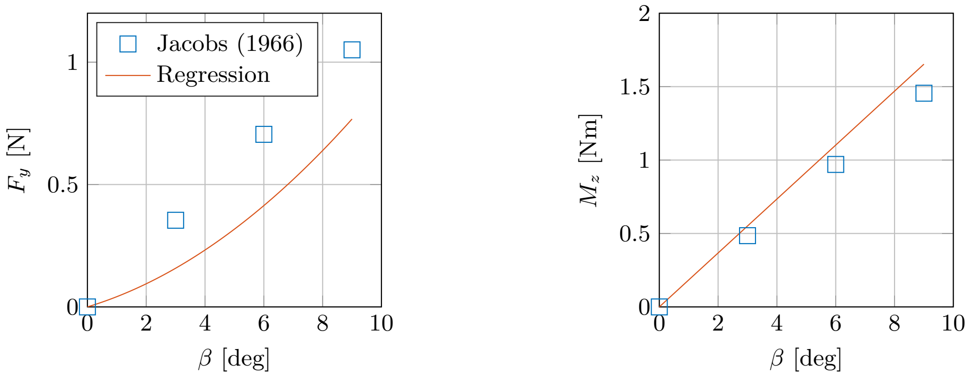

Figure 6-18: Fit of the regression results with experimental results for model 846 from the *840 Series* with removed skeg

6-5 Discussion

The regression formulae show satisfactory performance within the DSWAS with errors as expected from the residual fits in section 6-3. Testing the formulations on vessels outside the series offers some valuable insights into the performance of the formulations. Some observations:

- The yaw moment is predicted quite accurately, also for models not belonging to the series.
- The side force is predicted less accurately. Residuals within the series are typically around 20% while the fit for models not belonging to the series is also less than that of the yaw moment.
- Unfortunately, the formulation for residuary resistance C_{xR} is not properly evaluated due to the lack of available data on resistance at drift of the benchmark vessels.
- It seems plausible to ascribe underprediction of the side force and overprediction of the yaw moment to the aft hull shape. This tends to occur at models with more V-shaped aft sections resulting in a more skeg-like aft body profile than the pram-shaped DSWAS models. Results from Mobron (2014) confirm this effect of adding a skeg or more V-shaped aft sections.
- With the hull shapes of the *840 Series* rather similar to the DSWAS (pram aft ship without skeg) results show better agreement, even with some input parameters out of range.

The fit of the side force formulation is not satisfactory. The residuals are randomly spread up to about 20%. This is larger than the differences in side force between some of the models in the DSWAS. Due to this, an optimisation performed with a PPP using these formulations can end up yielding erroneous optima.

To increase the range of application of the formulations, one could include model parents with other types of aft ships. One with V-shaped sections leading to a faired-in skeg and perhaps a more modern one with a propeller gondola. Bulbous bows can be considered as well, allowing more modern vessels to be input for e.g. a retrofit study. However, from the current study no indication can be given on its influence.

Chapter 7

Conclusions

7-1 Validity of numerical simulations

Research question one, as stated in section 1-3-1, on the adequacy of the numerical method for the prediction of hydrodynamic forces for application within a Performance Prediction Programme (PPP) is answered predominantly positive. The validation study performed on the three selected models has reveals both adequacy and shortcomings of the numerical method.

- The resistance is predicted within about 5% of the experimental value for all models. This is within the validation uncertainty and validation is thus successful.
- The side force is not validated for two of the three models because the comparison errors exceed a reasonably large uncertainty estimate. The side force is therefore concluded to be poorly predicted by the numerical simulation (with comparison error around 10% for model #16).
- The yaw moment is not validated by the Verification and Validation (V&V) method. This is ascribed to its small uncertainty estimates, making it difficult for the comparison error to fall within those margins. In general, the comparison error on the yaw moment is observed to be of very acceptable magnitude ($2-4\%$).

In general it is observed that for a full ship with sharp bilges (model #16, $C_p^+C_m^+$) the side force is resolved most poorly while the comparison error for the yaw moment is highest for a smooth hull without sharp bilges (model #19, $C_p^-C_m^-$). The largest discrepancies overall occur at the side force of model #16. These deficits can possibly be ascribed to the lack of accuracy in the solution of vortices in the flow.

To put the validation into perspective, the foreseen application has to be kept in mind. With the results as input for regression formulations and ultimately a PPP, some scatter can be acceptable. At the highest drift angle of $\beta = 9^\circ$ the comparison error are mostly within 10%, which could arguably be a good *maximum* acceptable error for such a performance prediction of a design concept. However, absolute errors of similar magnitude result in larger relative errors for the side force at lower drift angles.

7-2 Regression

The formulations resulting from the regression analysis offer a means for predicting hydrodynamic forces by basic hull form parameters that can be implemented in a PPP. The formulations have a rather simple form, using four hydrostatic parameters as input at most. Also, the equations use no higher powers or products of parameters.

- The fit of the formula for residuary resistance coefficient C_{xR} leads to predictions of total resistance within 6% accuracy. This is an acceptable margin for the application in a PPP. Unfortunately, the resistance at drift is not evaluated properly outside the series due to the lack of available data.
- The formulation for side force coefficient C_y shows the largest residuals, up to about 20% at $\beta = 9°$ and even higher at $\beta = 3°$ because of the lower mean values. This accuracy is considered dissatisfying, as it is larger than the nuances of side force from model to model in the series. It could therefore lead to erroneous optimisation results.
- The formulation for yaw moment coefficient C_n has residuals mostly within 10%. This can be considered sufficient. The performance on vessels outside the series is quite good considering the differences in hull shape with respect to the series.

Research question two is also thus not entirely positively answered. Mainly the prediction of side force leaves room for improvement.

Discrepancies in side force and yaw moment on vessels outside the series are ascribed to fundamentally different hull forms, especially in the aft ship. With the Delft Systematic Wind-Assisted Series (DSWAS) only describing pram-type aft ships, more conventional V-shaped aft ships show more lateral area in the aft region. This has been shown in manoeuvring and previous WASP studies to offer a higher side force and a lower yaw moment. The effect of these deviating hull forms is not always expressed in hydrostatic coefficients and therefore not well captured by the formulations. Presumably, the same could hold for more modern ships featuring a propeller gondola.

7-3 Recommendations

Numerical method To improve the numerical results and attempt to reduce the comparison error with experiments, findings from this study give rise to the following recommendations:

- The numerical results can be improved by using the Explicit Algebraic Stress Model (EASM) turbulence model. Although somewhat more computational expensive than the used $k - \omega$ SST model, the comparison error is reduced to within the current estimates for the validation uncertainty when applied to model #16. However, one does need to re-evaluate the numerical uncertainty component by performing a new grid study with this turbulence model. The computation time is expected to increase by about 30%.
- The results can also be improved by including trim and sinkage in the computation. However, this comes at a cost of about twice the convergence time. This option therefore needs to be carefully considered when a large number of computations is needed.

Experimental method To reduce the experimental uncertainty the dominant contributors are considered:

- The correction for strip resistance is a major contributor to the experimental uncertainty. For future research where the estimation of experimental uncertainty is critical, it is recommended to evaluate this correction more thoroughly.
- The uncertainty from the calibration of the load cells brings another significant contribution. This is obtained from the difference in calibration factor before and after the test series. Measurement equipment on the carriage could be further evaluated for improvement.
- When looking for more validation material for numerical studies, an extensive list of experimental techniques exists. For the current study, a useful low-cost technique would be to draw a grid on the model's sides. This would offer *some* quantitative material on the wave elevation at the hull. Other techniques to investigate flow patterns such as tufts, oil paint or even Particle Image Velocimetry (PIV) are more intrusive or expensive.

Further WASP research When planning on expanding the systematic series to obtain formulations with better performance or a broader application range, different recommendations can be made.

- To prevent extrapolation outside the database, the range of varied parameters can be increased. This way, a larger variation of concepts can be evaluated.
- Results from the current series offer no clear signs that adding a different parameter for variation is necessary. However, it is known that a deadrise offers an increase in side force as well. This might therefore be worthwhile to investigate.
- The evaluation of the regression formulations indicates that it would be beneficial to introduce parent hulls with fundamentally different hull shapes to the series. Especially the shape of the aft stations has a large influence on both side force and yaw moment. Including models with more V-shape aft sections rather than the current U-shaped pram aft ships would greatly increase the applicability of the formulations. Similarly, a modern parent hull with propeller gondola and bulbous bow can be considered.

If the scope of hydrodynamic research on Wind-Assisted Ship Propulsion (WASP) is to be expanded from bare hull forces, the focus should be on the influence of appendages, as its contribution is expected to be significant. From other studies, the addition of a skeg in the aft ship is shown to control the yaw moment instability and strongly increase the side force production. The addition of bilge keels as is common on merchant vessels is expected to dominate the flow in that area, leading to different hydrodynamic forces.

Bibliography

ASME (2009). Standard for Verification and Validation in Computational Fluid Dynamics and Heat Transfer. Technical report, American Society of Mechanical Engineers, New York, NY.

Bergeson, L., Greenwald, C. K., and Kent Greenwald, C. (1985). Sail Assist Developments 1979 - 1985. *Journal of Wind Engineering and Industrial Aerodynamics*, 19(1-3):45–114.

Beukelman, W. (1989). Cross Fow Drag on a Segmented Model. Technical Report October, Delft University of Technology.

Beukelman, W. (1993). Lift and Drag for a Low Aspect-Ratio Surface Piersing Wing-Model in Deep and Shallow Water. Technical report, Delft University of Technology.

Beukelman, W. (1998). Manoeuvring Coefficients for a Wing-Model in Deep and Shallow Water. *International Shipbuilding Progress*, 45(441).

Bordogna, G., Markey, D. J., and Huijsmans, R. H. M. (2014). Wind-Assisted Ship Propulsion: a Review and Development of a Performance Prediction Program for Commercial Ships. *11th International Conference on Hydrodynamics*, pages 1–9.

Bovio, M. (2012). CFD Calculations Ecoliner. Technical report, Van Oossanen Naval Architects, Wageningen.

Bradbury, W. M. S. (1985). An Experimental Investigation of the Flow Past Hulls at Leeway. *Journal of wind engineering and industrial aerodynamics1*, 20(1-3):227–265.

Burden, A., Lloyd, T., Mockler, S., Mortola, L., Shin, I. B., and Smith, B. (2010). *Concept Design of a Fast Sail Assisted Feeder Container Ship*. Group design project, University of Southampton, Southampton.

Claughton, A., Pemberton, R., and Prince, M. (2013). Hull-Sailplan Balance, “Lead” for the 21st Century. Technical report, Wolfson Unit MTIA, University of Southampton, Southampton.

Coleman, H. W. and Steele, W. G. (2009). *Experimentation, Validation, and Uncertainty Analysis for Engineers*. John Wiley & Sons, Inc.

De Jong, M. J., Struijk, G. D., Vogels, R. H., and Voncken, N. H. P. (2012). *Vergelijkingsstudie naar de Toepassing van Hulpzeilvoortstuwing op een Vrachtschip*. Bsc thesis, Delft University of Technology.

Deng, G. and Visonneau, M. (1999). On the Prediction of Swirling Induced Recirculation. In *3rd International Symposium on Turbulence and Shear Flow Phenomena*, pages 377–382.

Deng, G. B., Queutey, P., and Visonneau, M. (2006). A Code Verification Exercise for the Unstructured Finite-Volume CFD Solver ISIS-CFD. In Wesseling, P., Onate, E., and Periaux, J., editors, *European Conference on Computational Fluid Dynamics*, pages 1–18.

Eça, L. and Hoekstra, M. (2009). Evaluation of Numerical Error Estimation based on Grid Refinement Studies with the Method of the Manufactured Solutions. *Computers & Fluids*, 38(8):1580–1591.

Eça, L. and Hoekstra, M. (2013). Solution Verification based on Grid Refinement Studies and Power Series Expansions. In *ASME Verification and Validation Symposium*.

Eça, L. and Hoekstra, M. (2014). A Procedure for the Estimation of the Numerical Uncertainty of CFD Calculations based on Grid Refinement Studies. *Journal of Computational Physics*, 262:104–130.

Fink, M. P. (1969). Full-Scale Investigation of the Aerodynamic Characteristics of a Sailwing of Aspect Ratio 5.9. Technical report, National Aeronautics And Space Administration, Washington D.C.

Fiorentino, A., Lecce, L., D'Antonio, A., Del Core, G., Maglione, A., and Marulo, F. (1985). Proposal of a Sail System for the Propulsion of a 25.000 TDW Bulk-Carrier. *Journal of Wind Engineering and Industrial Aerodynamics*, 19(1-3):115–137.

Fujiwara, T., Hearn, G. E., Kitamura, F., Ueno, M., and Minami, Y. (2005). Steady Sailing Performance of a Hybrid-Sail Assisted Bulk Carrier. *Journal of Marine Science and Technology*, 10(3):131–146.

Gerritsma, J., Beukelman, W., and Glansdorp, C. C. (1974). The Effects of Beam on the Hydrodynamic Characteristics of Ship Hulls. In Cooper, R. D. and Doroff, S. W., editors, *10th Symposium on Naval Hydrodynamics - Hydrodynamics for Safety Fundamental Hydrodynamics*, pages 3–33, Cambridge, MA. Massachusetts Institute of Technology.

Glansdorp, C. C. (1973). Horizontal High Frequency PMM-Tests With A Mariner Model. Technical Report 381, Delft University of Technology.

Hoerner, S. F. (1985). *Fluid Dynamic Lift - Practical Information on Aerodynamic and Hydrodynamic Lift*. Mrs. Liselotte A. Hoerner, Vancouver, second edition.

Hooft, J. P. and Quadvlieg, R. H. H. A. (1996). Non-linear Hydrodynamic Hull Forces Derived from Segmented Model Tests. *Marine Simulation and Ship Manoeuvrability*, pages 399–410.

Huetz, L. (2012). *Systematic Study of the Hydrodynamic Behaviour of Sailing Yacht Hulls using CFD and Parametric Design.* Phd thesis, Ecole Centrale de Nantes.

Ingham, P. and Tersløv, O. (1985). Wind Tunnel Tests and Manoeuvre Simulator Tests with Different Types of Sails and Ships. *Journal of Wind Engineering and Industrial Aerodynamics*, 20(1-3):169–185.

Inoue, S., Hirano, M., and Kijima, K. (1981). Hydrodynamic Derivatives On Ship Manoeuvring. *International Shipbuilding Progress*, 28(321).

ITTC (2002). Recommended Procedures and Guidelines: Uncertainty Analysis in CFD , Verification and Validation Methodology and Procedures. In *23rd International Towing Tank Conference.*

ITTC (2005). ITTC - Recommended Procedures and Guidelines - Resistance Test. Technical report.

ITTC (2011). Fresh Water and Seawater Properties. Technical report.

ITTC (2014a). Example for Uncertainty Analysis of Resistance Tests in Towing Tanks. In *27th International Towing Tank Conference.*

ITTC (2014b). General Guideline for Uncertainty Analysis in Resistance Tests. In *27th International Towing Tank Conference.*

ITTC (2014c). Practical Guide for Uncertainty Analysis of Resistance Measurement in Routine Tests. In *27th International Towing Tank Conference.*

ITTC (2014d). Recommended Procedures and Guidelines: Guide to the Expression of Uncertainty in Experimental Hydrodynamics. In *27th International Towing Tank Conference.*

Jacobs, W. R. (1966). Estimation of Stability Derivatives and Indices of Various Ship Forms, and Comparison With Experimental Results. *Journal of Ship Research1*, 10:135–163.

Jones, R. T. (1946). Properties of Low-Aspect-Ratio Pointed Wings at Speeds Below and Above the Speed of Sound. Technical report, NACA.

Kijima, K., Katsuno, T., Nakiri, Y., and Furukawa, Y. (1990). On the Manoeuvring of a Ship with the Parameter Performance of Loading Condition.

Kijima, K., Nakiri, Y., and Furukawa, Y. (2004). On a Prediction Method for Ship Manoeuvrability. Technical report, Kyushu University.

Kornev, N. (2011). Ship Theory I - Ship Manoeuvrability. Technical report, Universität Rostock, Rostock.

Lackenby, H. (1950). On the Systematic Geometrical Variation of Ship Forms. *Transactions of the TINA*, 92:289–316.

Larsson, L., Stern, F., and Visonneau, M. (2013). CFD in Ship Hydrodynamics - Results of the Gothenburg 2010 Workshop. Technical report.

Letcher, J. S. (2009). *The Principles of Naval Architecture Series - The Geometry of Ships*. The Society of Naval Architects and Marine Engineers, Jersey City, NJ, first edition.

Maskell, E. (1955). Flow Separation in Three Dimensions. Technical report, Royal Aircraft Establishment.

Minami, Y., Nimura, T., Fujiwara, T., and Ueno, M. (2003). Investigation into Underwater Fin Arrangement Effect on Steady Sailing Characteristics of a Sail Assisted Ship. In *Proceedings of the thirteenth international offshore and polar engineering conference*.

Mobron, E. (2014). *Improving the Performance of a Sail-Assisted Cargo Vessel*. Msc thesis, Delft University of Technology.

Munk, M. M. (1924). Remarks on the Pressure Distribution over the Surface of an Ellipsoid, Moving Translationally Through a Perfect Fluid. Technical report, NACA.

Naaijen, P. and Koster, V. (2007). Performance of Auxiliary Wind Propulsion for Merchant Ships using a Kite. Technical report, Delft University of Technology.

Nikkels, T. (2013). The Ecoliner Concept. In *2nd Natural Propulsion seminar*, pages 1–22, Wageningen.

Nomoto, K. and Tatano, H. (1979). Balance of Helm of Sailing Yachts. Technical report, University of Osaka.

NUMECA (2014). Theoretical Manual. Technical report, NUMECA International, Brussels.

Pope, S. B. (2000). *Turbulent Flows*. Cambridge University Press, first edition.

Prandtl, L. (1925). Application of the “Magnus Effect” to the Wind Propulsion of Ships. Technical report, National Advisory Committee for Aeronautics, Washington D.C.

Rijpkema, D. and Vaz, G. (2011). Viscous Flow Computations on Propulsors : Verification, Validation and Scale Effects. In *RINA Developments in Marine CFD*, pages 35–47.

Satchwell, C. J. (1986). Fiji Windship “Cagidonu”. Technical report, University of Southampton.

Schenzle, P. (1980). Standardised Speed Prediction for Wind Propelled Merchant Ships. In *Symposium On Wind Propulsion Of Commercial Ships*.

Schenzle, P. (1985). Estimation of Wind Assistance Potential. *Journal of Wind Engineering and Industrial Aerodynamics*, 20:97–110.

Schmidt, A. and Vahs, M. (2013). Entwicklung eines innovativen Schiffsantriebes gekennzeichnet durch den Einsatz von Magnus-Rotoren zur Windenergienutzung in Kombination mit einem hierauf abgestimmten Antriebspropeller. Technical report, Enercon GmbH, Aurich.

Skogman, A. (1985). The practical Meaning of Lateral Balance for a Sail-Assisted Research Vessel. *Journal of wind engineering and industrial aerodynamics*, 20(1-3):201–226.

Smith, T., Newton, P., Winn, G., and Grech La Rosa, A. (2013). Analysis Techniques for Evaluating the Fuel Savings Associated with Wind Assistance. *Low Carbon Shipping Conference*, pages 1–13.

Struijk, G. D. and Vogels, R. H. (2012). GDNP Ecoliner - Tests Upright and with Heeling and Leeway Angles. Technical report, Delft University of Technology.

Van Gastel, K. (1981). Onderzoek naar de Zeileigenschappen van Vrachtschepen. Technical report, Delft University of Technology.

Viola, I. M., Sacher, M., Xu, J., and Wang, F. (2014). A Performance Prediction Program for Wind-Assisted Ship Propulsion. Technical Report 2000.

Visonneau, M., Queutey, P., and Deng, G. B. (2006). Model and Full-Scale Free-Surface Viscous Flows around Fully-Appended Ships. In *European Conference on Computational Fluid Dynamics*, pages 1–16.

Wagner, B. (1967). Fahrtgeschwindigkeitsberechnung für Segelschiffe. *Jahrgang Schiffbau Technischen Gesellschaft*, 61:14–35.

WS Atkins Consultants (2002). Guidelines for Marine Applications of Computational Fluid Dynamics. Technical report.

Appendix A

Literature on WASP

In this appendix a literature review is given on research in the area of Wind-Assisted Ship Propulsion (WASP). Both research from the 1980's and more recent work is treated. The focus is on the hydrodynamics treated in the papers.

Past research

The interest in WASP peaked in the 1980's because of rising fuel prices. WASP studies from this period are reviewed below.

Bergeson et al. (1985) summarise six years of work on WASP, amounting to a very comprehensive study covering many aspect such as an aerodynamic comparison of different rig types (including full scale tests), performance prediction calculations and economic models. The technical part of this research focusses on the aerodynamics while very little of hydrodynamics is treated. The wingsail is flagged as best rig type.

In contrast, Schenzle (1985) includes a reliable hydrodynamic force prediction based on model experiments. Also for the rig, wind tunnel experiments are conducted. Conclusions are made in terms of best aerodynamic solution. Also here, the wingsail is appointed as the best overall performer for this application.

Skogman (1985) was one of the few to address lateral balance at that time. He did so by analysing a vessel using manoeuvring coefficients by Inoue et al. (1981) and aero data from Fink (1969), neglecting interaction effects of multiple sails. Results are presented in terms of drift angles, rudder angles, and added resistance in waves. The main conclusion was that putting the sails far forward resulted in the lowest rudder angles, an indication of a large yaw moment. Furthermore, the influence of some main parameters (L, T, $^L/_B$ and C_b) are discussed. Increasing C_b decreases the rudder angle considerably, as does decreasing $^L/_B$, implying a lower yaw moment. A larger draft T (increasing the aspect ratio) increases the side force production (or reduces leeway for the same side force).

While not providing an end-to-end WASP study, Bradbury (1985) did go to greater lengths to expose the physics behind a cargo vessel at drift. Conducting wind tunnel experiments with flow visualisation using oil, revealing when and where vortices are developed. The tested models are a representative ship hull and hull-blocks (extrusions of the waterplane area, consequently featuring sharp bilges) of different L/B, tested at different trim. From this paper it can be concluded that sharp bilges (from the block models) generate more side force, but come with a drag penalty. Increasing beam increases drag and lift, but L/D is lower while the Centre of Lateral Resistance (CLR) is about constant. Increasing draft increases lift and drag, but lift at a larger rate so that L/D is higher, and CLR shifts forward by a small amount. When trimming bow-down drag reduces at small leeway but increases at higher leeway, while little change in lift is observed. CLR is shifted well forward. Trimming by the stern has the opposite effect, but lift increases as well. Heeling the vessel causes the deep bilge to produce the main vortex. At zero leeway, a small side force is measured due to asymmetry of the heeled hull. At small leeway angles the drag and lift is reduced, while at large leeway angles drag is increased and the lift even more, causing L/D to increase. The CLR moves forward with increased heel angle.

Some studies stress the importance of appendages in aiding the vessel to produce side force and control the yaw moment. Schenzle (1980) already emphasised the need for bar keel, sloping keel or fins to aid the yaw balance. As far as hull shape goes, increased draft and a rounded bow shape is mentioned. Fiorentino et al. (1985) come with a proposal for automatically trimmed fins fore and aft, allowing the vessel to sail without any leeway at all. Also the yaw balance can be controlled this way. Results show to be in favour of the fin configuration when compared to bare hull condition when sailing close hauled with high aspect ratio sails. Sailing downwind, the addition of fins would not be favourable. Balancing a vessel under sail has two sides and Ingham and Tersløv (1985) mention that placement of the rig is also vital in preventing large rudder angles.

At the Delft University of Technology, Van Gastel (1981) tested a cargo vessel of the *Victory* type and a fishing trawler in the towing tank at a range of heel and drift angles. While neglecting the influence of the yaw moment, a performance prediction shows a thrust reduction of 60% and 15% for the Victory and trawler respectively at a wind speed of 7 m/s.

On a whole different approach, Satchwell (1986) conducted full-scale measurements on board a Fiji wind assisted ship. Although the method had its limitations, allowing for a large spread in results, available data suggests a maximum fuel saving of 37% under full canvas.

Recent studies

Studies from recent years also show the potential fuel savings from using wind assistance. However, the spread of results is large. This is caused both by the difference in approaches and the lack of accurate prediction methods.

To asses the wind-assisted performance of a retrofitted tanker, Viola et al. (2014) fitted America's Cup wing sails. The aero data originate from Computational Fluid Dynamics (CFD) work while the hydro data is taken from standard manoeuvring coefficients as proposed by Kijima et al. (1990), leaving room for discussion on the accuracy of the forces predicted. The work concludes with a "maximum oil saving" of about 10% at a transit speed of 10 kn and a wind speed of 13 kn.

Fujiwara et al. (2005) evaluated the performance of a sail-assisted bulk carrier. Hydrodynamic coefficients are taken from towing tank experiments and aerodynamic coefficients from wind tunnel experiments, including sail-sail and sail-hull interaction effects. This gives more confidence in the force prediction, as the actual configuration is experimentally evaluated. The so-called square hybrid sails (slat + rigid wing sail + soft sail) are shown to account for some 12% of the total thrust at 10 m/s wind speed and 13 kn transit speed on a North Pacific route. An interesting observation from the towing tank experiments is that all hydrodynamic forces (resistance, side force and yaw moment) are "fairly insensitive to changes of heel angle".

Smith et al. (2013) offer a general approach for the performance prediction of WASP. Although they do not publish full results, their approach on the *B9* concept appears solid, deploying experimental techniques in the wind tunnel and towing tank for the concept at hand. Also, the developed tools seem to incorporate a lot of effects, including added resistance in waves and extensive routing analysis. The observed range of fuel savings is $10 - 50\%$, depending on rig type and service speed.

If utilising kite propulsion, Naaijen and Koster (2007) show that the amount of hydrodynamic side force and yaw moment generated is small. Although the hydrodynamic forces are obtained by standard manoeuvring coefficients by Kijima et al. (2004), it does give indication that this type of rig induces little side force, yaw moment and consequently rudder angle.

Research dealing with the yaw balance issue of WASP ships are still scarce. Minami et al. (2003) showed that the best position for a fin is most aft, resulting in the lowest rudder angles. Claughton et al. (2013) raised the issue of balance on heavy displacement sailing *yachts* with high drag to side force ratios, a situation certainly applicable to cargo vessels.

Studies on the Dykstra Naval Architects designed WASP concept *Ecoliner* (Nikkels, 2013) reveal yaw moment issues. The large yaw moment results in a CLR very far forward for the bare hull featuring a pram stern, causing a significant imbalance with the aerodynamic forces. Tank test by Struijk and Vogels (2012) and CFD calculations by Bovio (2012) are in agreement on this. A study by Mobron (2014) has proven the addition of an aft skeg, or deadwood, to be very effective in restoring the yaw balance. Also the effect of some hull form parameters are studied, some results are summarised below.

- simple skeg added at the aft ship: significant aft shift of CLR (46% of L_{wl}) and increase of side force (F_y), resistance (F_x) increases by 3%.
- faired skeg: less shift in CLR, less increase in F_y, but lower F_x than simple skeg
- bar keel: moves CLR a bit forward, increases F_y and F_x
- 10° deadrise: higher F_y, CLR little more aft, decrease in F_x (induced drag?)
- 30° stem angle: CLR 1% more aft
- increased bow profile radius: CLR 1% more aft, slightly lower F_y and F_x
- waterline entry angle: CLR 1% more aft, lower F_y, slightly lower F_x
- C_p: smaller C_p (by increasing bilge radius and shortening parallel midbody) yields a more aft CLR and higher F_y, probably due to a greater skeg surface. It does raise F_x however.
- LCB +3%: shifts CLR aft by 8% at the cost of some lower F_y and higher F_x

- L_{wl}: increasing length (keeping displacement constant and reducing B and T) shifts CLR aft (more skeg area), but decreases F_y a little (due to reduced draught). Length increases X due to larger wetted area, but for fuller ships ($C_b = 0.71$) the shortest version has the highest X due to dominant wavemaking resistance.
- C_b: lower C_b means more room for the aft skeg, shifting CLR aft and increasing F_y. X is lowest for low C_b.

Especially adding a skeg to the aft ship has a significant effect of reducing the yaw moment, shifting the CLR aft. Although it is interesting to see the impact of these parameters, the approach has not been systematic, so not all effects can be isolated. Furthermore, the CFD calculations have not been verified and validated.

A good example of a recently developed and *built* WASP concept is the E-Ship 1 (Schmidt and Vahs, 2013). Developed by Enercon, this cargo vessel features four Flettner rotors. The ship has been sailing around the globe since 2010, offering plenty of full-scale data for validation of performance predictions. Unfortunately, no figures are published. The same holds for a company called Skysails. They have implemented kite propulsion on a number of vessels. But also here, little data is available.

Burden et al. (2010) performed a comprehensive study as group thesis on the design of a sail assisted container feeder. Hydrodynamic forces are obtained by towing tank tests, aerodynamic forces by wind tunnel experiments. A power reduction of 6% at a service speed of 15 kn has been reported when fitting a *multi-wing* system.

Hydrodynamic forces and moments The challenge of imbalance of a bare hull (low-aspect ratio body without defined keel) under drift and heel angle is of major importance for the feasibility of a WASP concept. For this, a proper prediction of the hydrodynamic forces and moments is paramount. Existing methods in literature are now discussed.

The influence of L/B ratios is investigated by Gerritsma et al. (1974) by altering the breadth. Conclusion is that the effect on side force and yaw moment is not very pronounced at low froude numbers (0.15 and 0.20), but some variation is observed at $F_n = 0.30$ which is due to the wave making.

An experimental investigation into the influence of draft is presented by Beukelman (1998) where a wing-model is towed in two opposite directions at various draughts, resulting in different aspect ratios. Also, the tips ('bilges') are tested as sharp and rounded. This study concludes that round bilges decrease drag as well as side force. Both the side force and yaw moment increases strongly with draught (or aspect ratio), but the yaw moment increases more strongly, resulting in a more forward CLR for deeper draught. Towing the wing backwards, i.e. with the sharp end as bow, results in lower side force and higher yaw moment and thus a more forwards CLR. Interestingly, this situation resembles a ship's waterline more.

Another interesting paper in the field of manoeuvring is Jacobs (1966) where expressions are offered to incorporate the effect of adding fins at the aft ship. This could be one of the solutions to stabilise a vessel which has a too large yawing moment at a drift angle. It does so by utilising Jones' formula for low aspect airfoils (Jones, 1946). Results are shown to be in good agreement with experiments. Addition of a large skeg is shown to bring the CLR from 75% in bare hull condition to $19 - 27\%$ of L_{wl} forward of LCG. The skeg study on the *Ecoliner* by Mobron (2014) shows the same orders of magnitude.

Summary The parameters of influence on the hydrodynamic forces developed by a ship under leeway are listed in Table A-1. Here, one can see the results found in literature. Sometimes they contradict each other. For example, according to Kijima et al. (2004) an increasing L/B ratio decreases F_y, while according to Skogman (1985) the opposite is true. This could arise from the way of scaling.

Table A-1: Summary of citations on the influence of main parameters on the hydrodynamic forces, ↑ increase, ↓ decrease, ← aftward, → forward, ∼ small effect

Increasing parameter	**Effect on side force F_y**	**Effect on CLR**	**Comments**
T	Bradbury (1985) ↑ Skogman (1985) ↑ Mobron (2014) ↑ Kijima et al. (2004) & Inoue et al. (1981) ↑ Beukelman (1998) ↑	Bradbury (1985) ∼→ Skogman (1985) ∼ Mobron (2014) ∼← Beukelman (1998) →	Here every reference concludes a positive contribution of T on F_y. The effect on CLR is small according to most, while Beukelman shows a forward shift.
θ (trim by stern)	Bradbury (1985) ↑	Bradbury (1985) ← Hooft and Quadvlieg (1996) ←	Trimming by the stern yields higher F_y and brings CLR aft.
ϕ	Bradbury (1985) ∼↑ Fujiwara et al. (2005) ∼ Mobron (2014) ∼	Bradbury (1985) → Fujiwara et al. (2005) ∼ Mobron (2014) ∼	According to most, the effect of heel is negligible. Bradbury (1985) concludes increase in F_y and M_z and a forward shift of CLR.
B	Bradbury (1985) ∼↑ Gerritsma et al. (1974) ∼ (at small F_n)	Bradbury (1985) ∼ Gerritsma et al. (1974) ∼	Small effect on F_y and CLR.
L/B	Gerritsma et al. (1974) ∼ (at small F_n) Skogman (1985) ↑ Kijima et al. (2004) ↓	Gerritsma et al. (1974) ∼ Skogman (1985) → Mobron (2014) ←	Very different conclusions. Could be due to the way of scaling L/B and leaving certain other parameters constant.
C_b	Skogman (1985) ∼ Mobron (2014) ↓ Kijima et al. (2004) ↑	Skogman (1985) ← Mobron (2014) → (skeg area)	Different conclusions, possibly by way of scaling. Also, for Mobron (2014) lowering C_b means more skeg area.
R_{bilge}	Bradbury (1985) ↓ Beukelman (1998) ↓	Bradbury (1985) → Beukelman (1998) →	Increasing bilge radius (or consequently C_m) lowers F_y and brings CLR forward.
Deadrise	Mobron (2014) ↑	Mobron (2014) ∼←	Introducing deadrise increases F_y but CLR remains about constant.
C_p	Mobron (2014) ↓	Mobron (2014) →	A higher C_p leaves less room for the aft skeg area.
LCB	Mobron (2014) ∼	Mobron (2014) ←	Little effect on F_y, CLR moves aft. Could be because of larger skeg area.
Appendages:			
bar keel	Mobron (2014) ↑	Mobron (2014) ∼	Adding a bar keel increases F_y but CLR remains constant.
fin/skeg aft	Mobron (2014) ↑	Mobron (2014) ∼ Schenzle (1980) ← Minami et al. (2003) ←	All conclude a considerable aft shift of CLR and Mobron (2014) also shows a increase in F_y.
sloping keel	Mobron (2014) ↑	Mobron (2014) ← Schenzle (1980) ←	Both confirm a shift of CLR aft. Mobron (2014) concudes an increase in F_y.

Appendix B

Linesplans

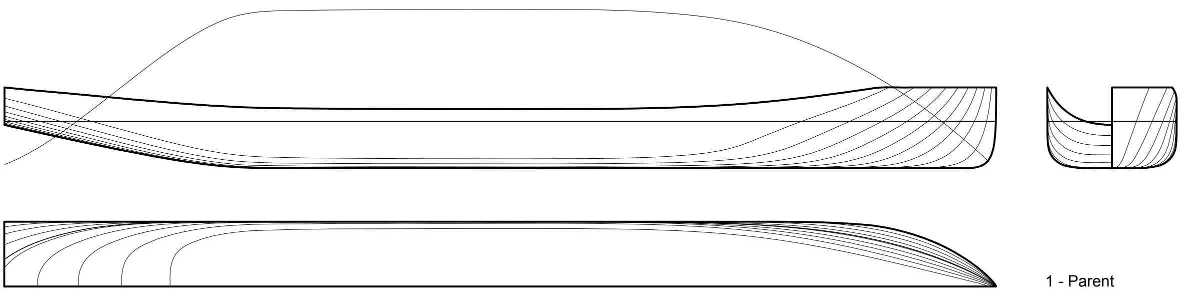

Figure B-1: Model #1

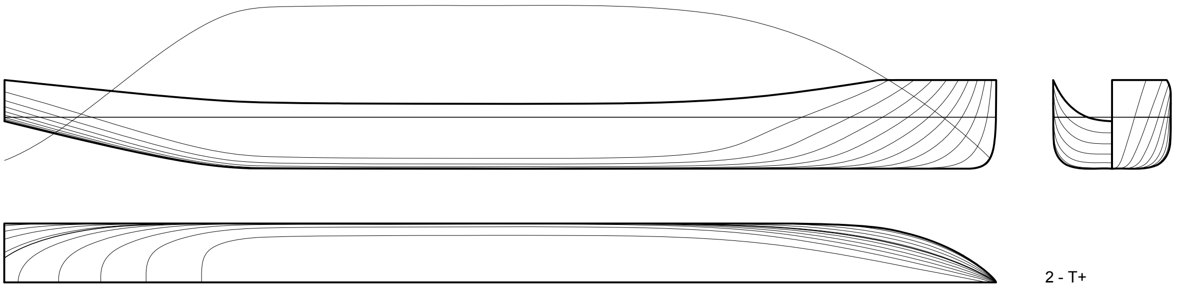

Figure B-2: Model #2

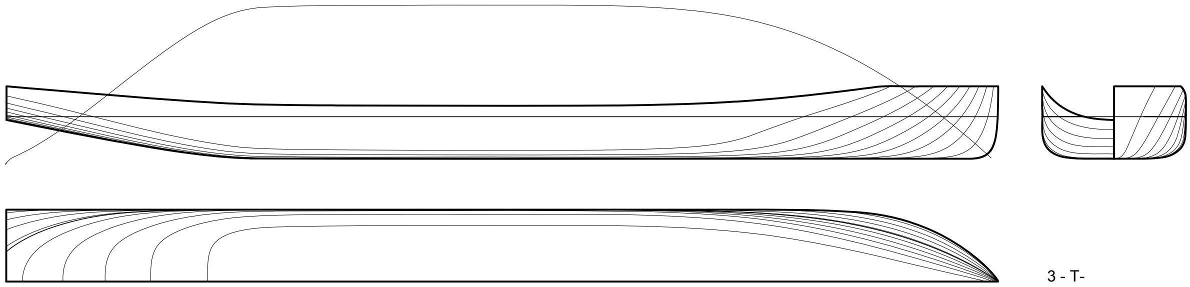

Figure B-3: Model #3

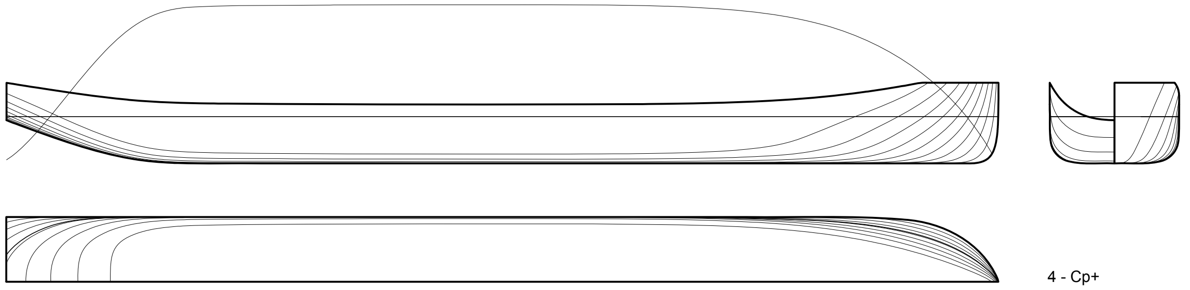

Figure B-4: Model #4

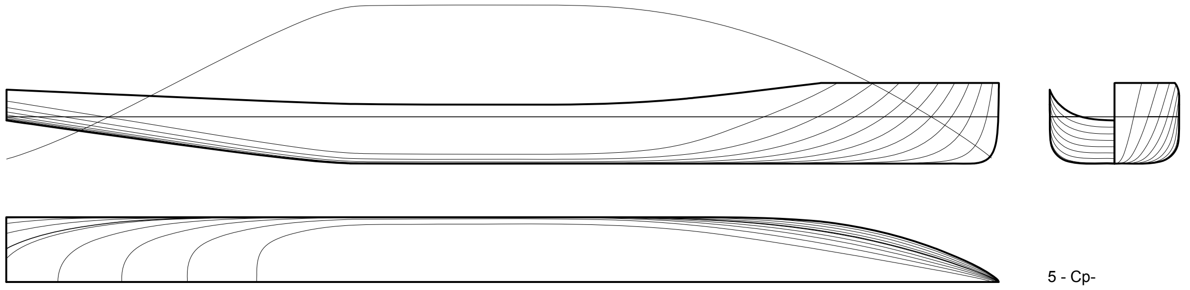

Figure B-5: Model #5

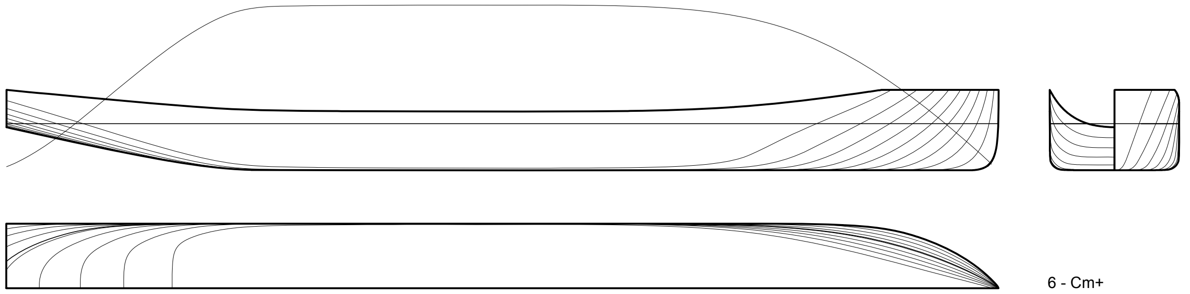

Figure B-6: Model #6

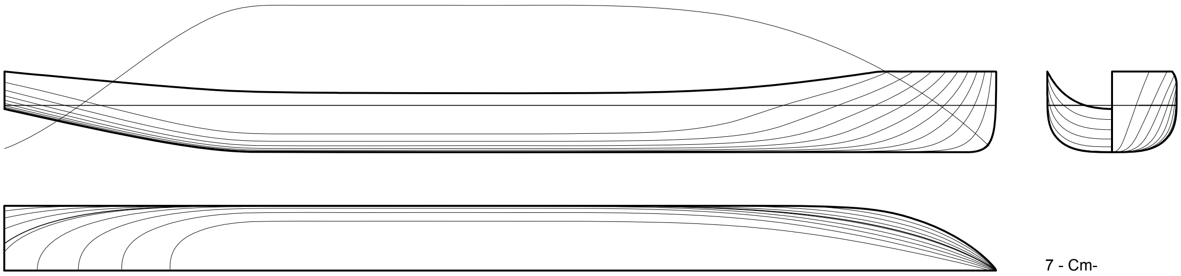

Figure B-7: Model #7

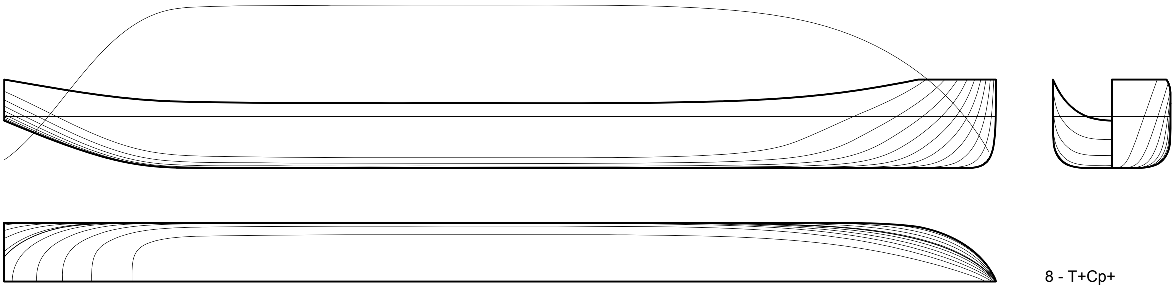

Figure B-8: Model #8

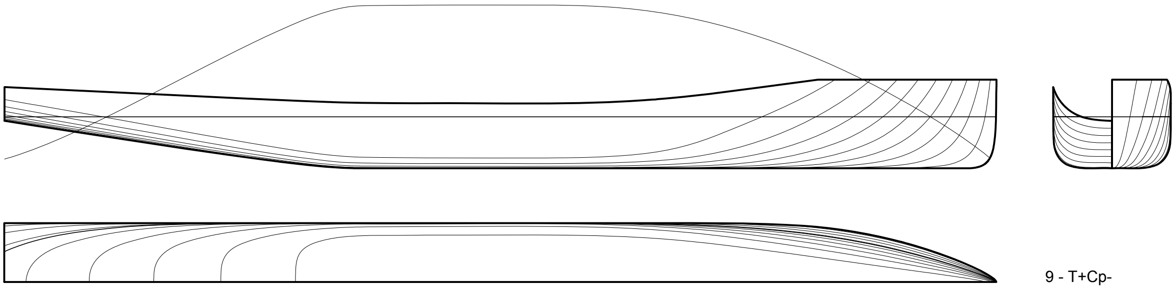

Figure B-9: Model #9

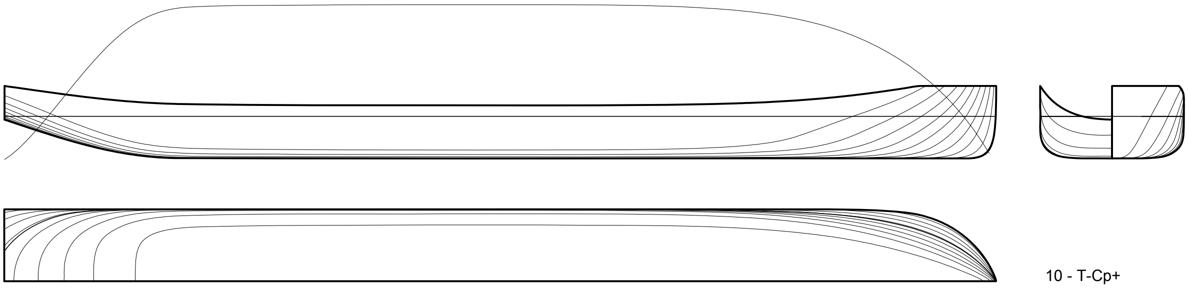

Figure B-10: Model #10

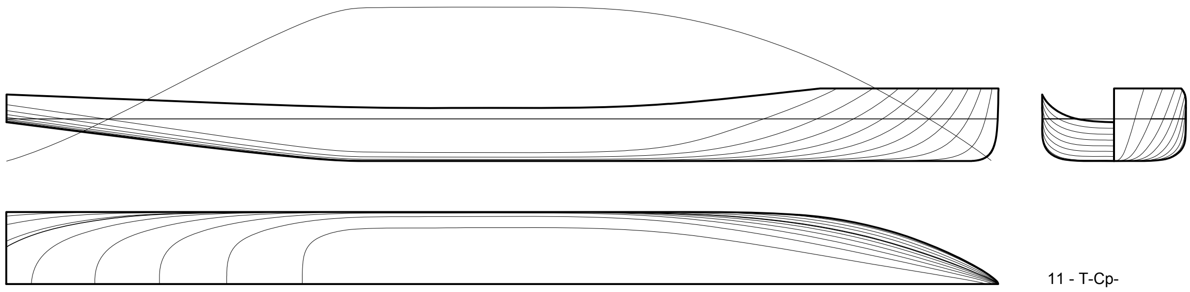

Figure B-11: Model #11

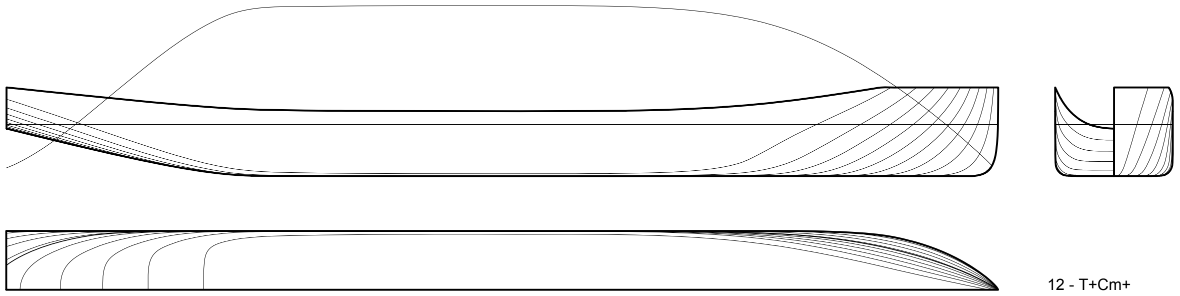

Figure B-12: Model #12

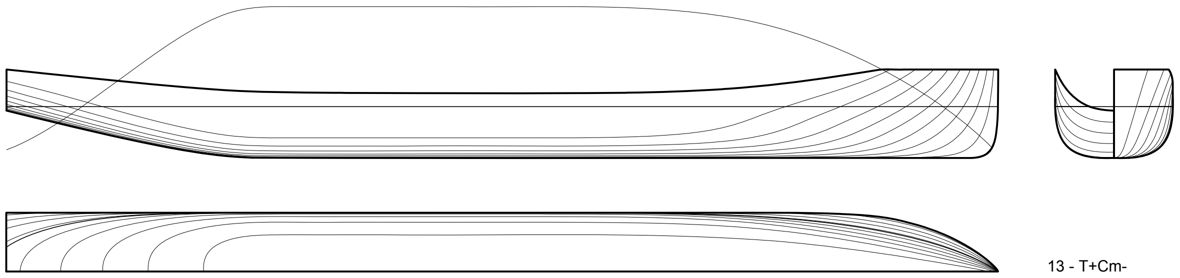

Figure B-13: Model #13

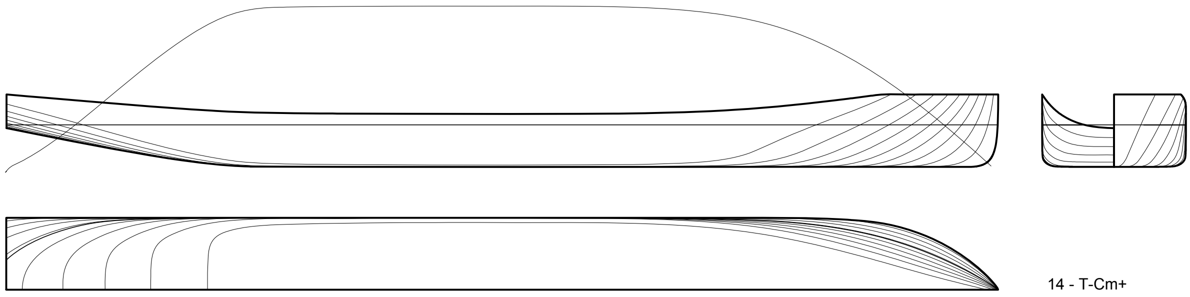

Figure B-14: Model #14

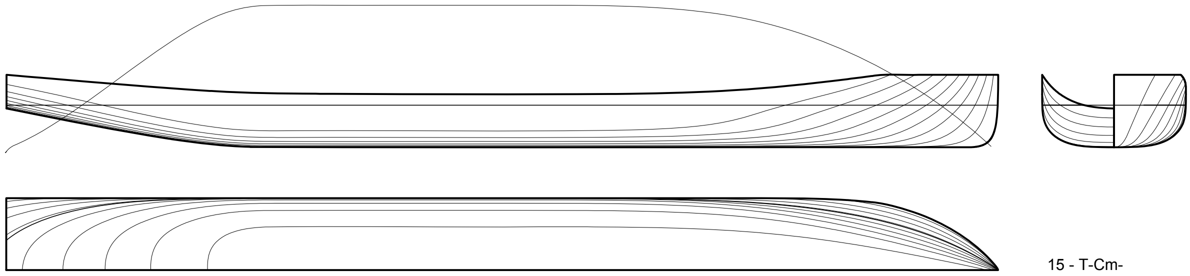

Figure B-15: Model #15

Figure B-16: Model #16

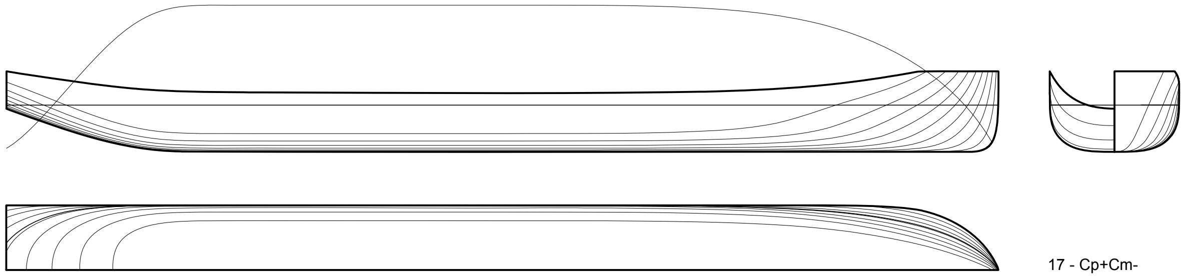

Figure B-17: Model #17

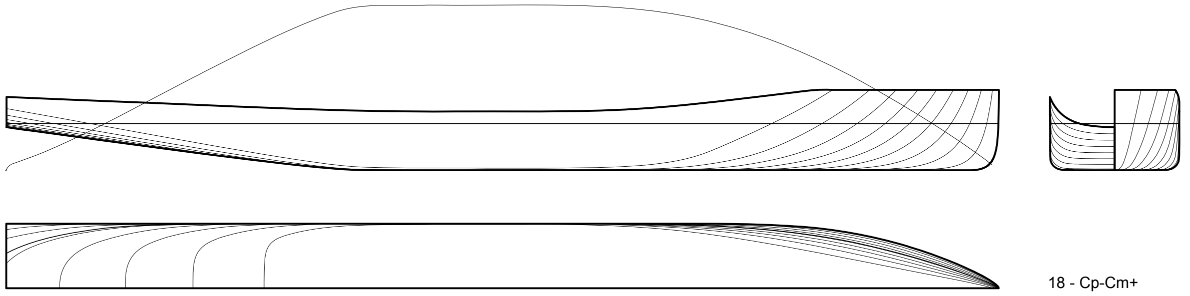

Figure B-18: Model #18

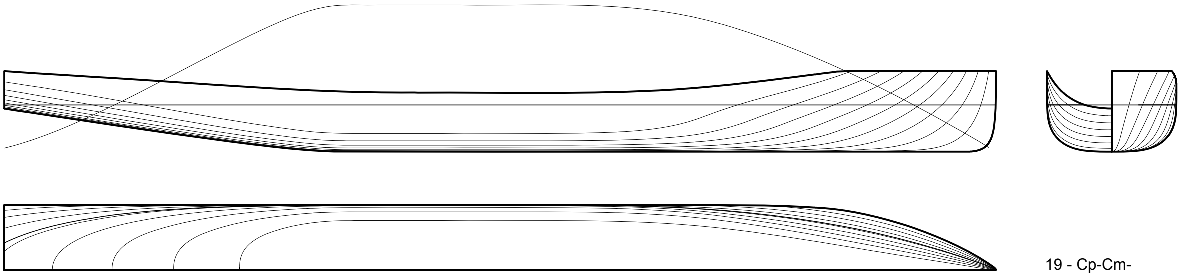

Figure B-19: Model #19

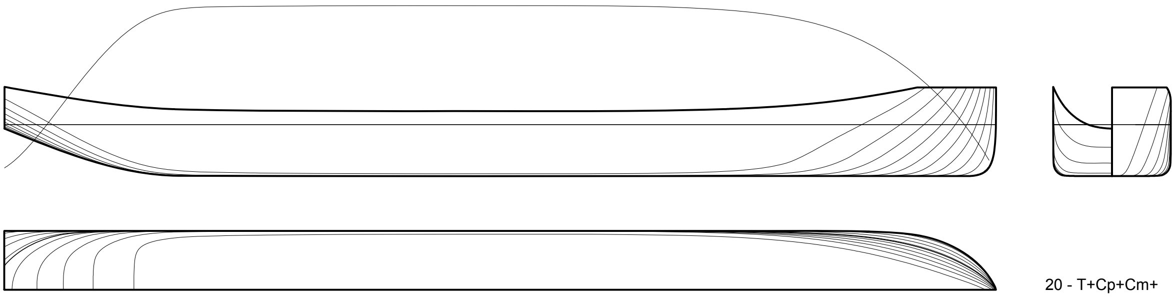

Figure B-20: Model #20

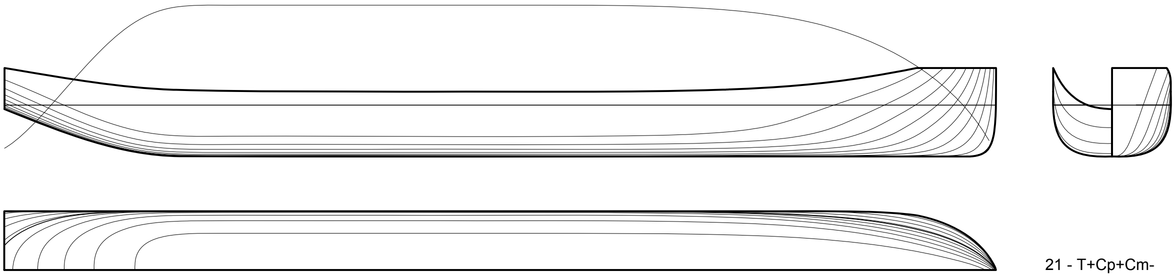

Figure B-21: Model #21

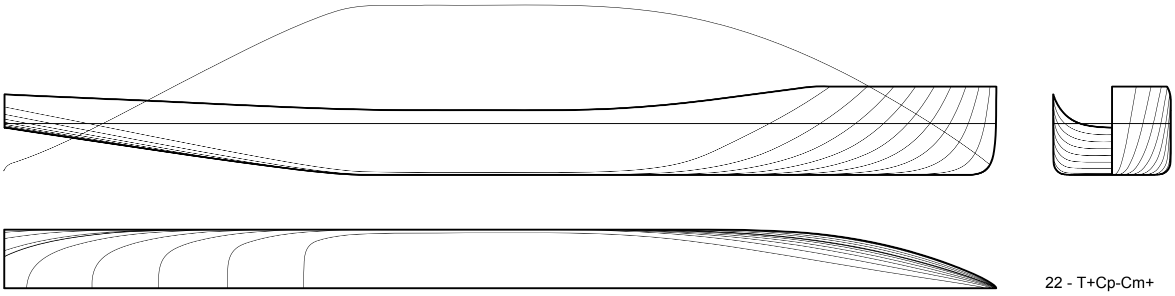

Figure B-22: Model #22

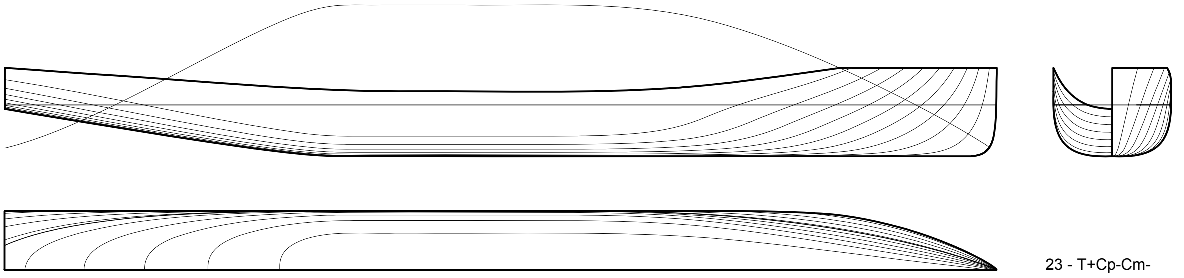

Figure B-23: Model #23

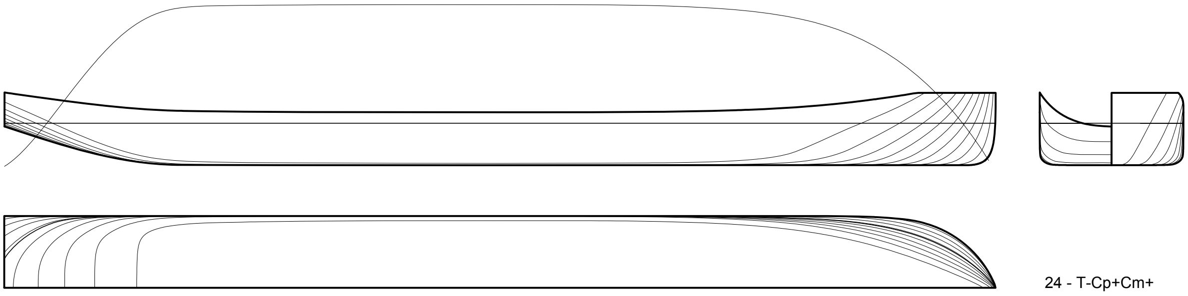

Figure B-24: Model #24

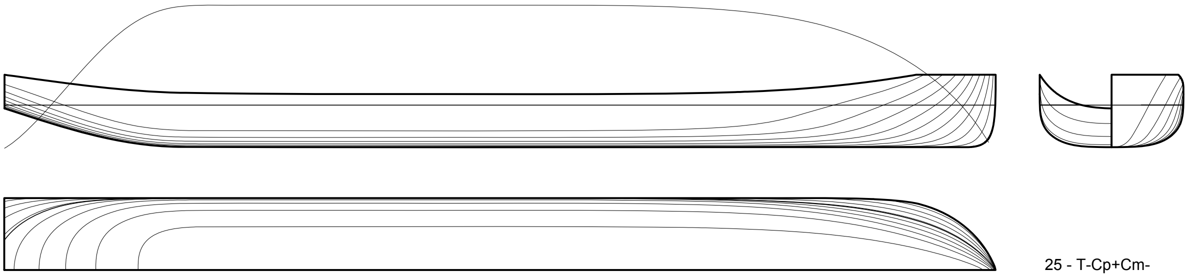

Figure B-25: Model #25

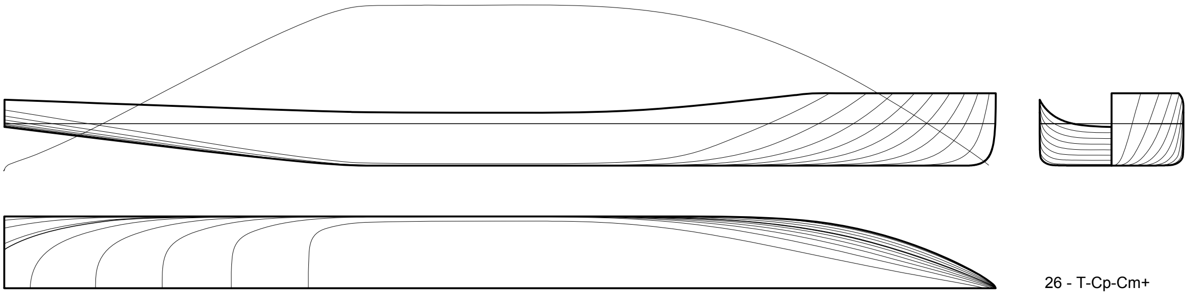

Figure B-26: Model #26

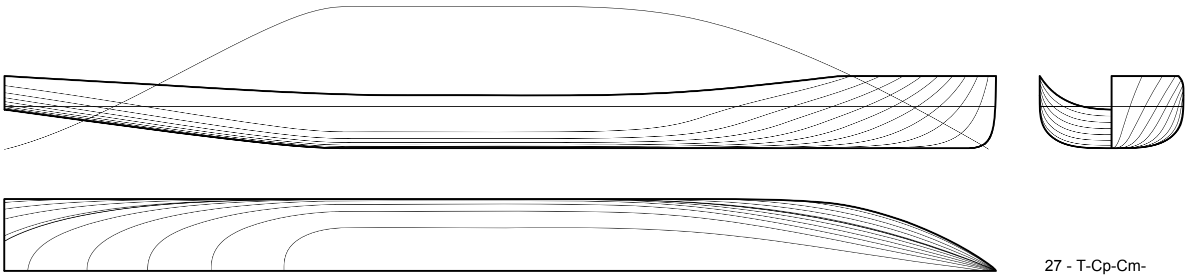

Figure B-27: Model #27